sid.inpe.br/mtc-m21b/2016/10.27.08.14-TDI

STUDY OF JOVIAN HIGH LATITUDE RADIO EMISSIONS VARIABILITY USING 26 YEARS OF NANÇAY DECAMETRIC ARRAY DATABASE (ESTUDO DA VARIABILIDADE DAS EMISSÕES JOVIANAS DE RÁDIO DE ALTA LATITUDE USANDO 26 ANOS DE DADOS DO ARRANJO DECAMÉTRICO DE NANÇAY)

Manilo Soares Marques

Doctoral Thesis of the Graduate Course in Space Geophysics, Supervised by Drs. Ezequiel Echer, Philippe Zarka and Maria Virginia Alves, approved in november 22, 2016.

URL of the original document:
<http://urlib.net/8JMKD3MGP3W34P/3MMAQAP>

INPE
São José dos Campos
2017

STUDY OF JOVIAN HIGH LATITUDE RADIO EMISSIONS VARIABILITY USING 26 YEARS OF NANÇAY DECAMETRIC ARRAY DATABASE (ESTUDO DA VARIABILIDADE DAS EMISSÕES JOVIANAS DE RÁDIO DE ALTA LATITUDE USANDO 26 ANOS DE DADOS DO ARRANJO DECAMÉTRICO DE NANÇAY)

Manilo Soares Marques

Doctoral Thesis of the Graduate Course in Space Geophysics, Supervised by Drs. Ezequiel Echer, Philippe Zarka and Maria Virginia Alves, approved in november 22, 2016.

INPE

São José dos Campos

2017

Aluno (a): **Manilo Soares Marques**

Título: " STUDY OF JOVIAN HIGH LATITUDE RADIO EMISSIONS VARIABILITY USING 26 YEARS OF NANÇAY DECAMETRIC ARRAY DATABASE (ESTUDO DA VARIABILIDADE DAS EMISSÕES JOVIANAS DE RÁDIO DE ALTA LATITUDE USANDO 26 ANOS DE DADOS DO ARRANJO DECAMÉTRICO DE NANÇAY)".

Aprovado (a) pela Banca Examinadora em cumprimento ao requisito exigido para obtenção do Título de *Doutor(a)*   em

Geofísica Espacial/Ciências do Ambiente Solar-Terrestre

Dr.   Marcelo Magalhães Fares Saba

Presidente / INPE / SJCampos - SP

Dr.   Ezequiel Echer
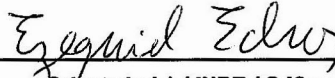
Orientador(a) / INPE / SJCampos - SP

Dra.   Maria Virginia Alves
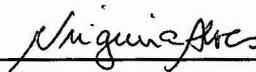
Orientador(a) / INPE / SJCampos - SP

Dr.   Phillipe Zarka

Orientador(a) / LESIA / França - FR

Dr.   Jean Pierre Raulin

Convidado(a) / CRAAM/Mackenzie / São Paulo - SP

Dr.   Luiz Fernando Ziebell

Convidado(a) / UFRGS / Porto Alegre - RS

Dr.   Francisco Carlos Rocha Fernandes
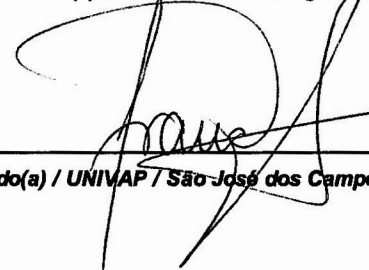
Convidado(a) / UNIVAP / São José dos Campos - SP

Este trabalho foi aprovado por:

( ) maioria simples

(x) unanimidade

São José dos Campos, 22 de Novembro de 2016

ACKNOWLEDGEMENTS

ABSTRACT

Jupiter is a complex radio source in the decameter wavelength range. The emission is anisotropic, intrinsically variable at milliseconds to hour timescales, and modulated by various causes at longer timescales, from ∼10h to months or years (Jovian day and year, season, solar activity and solar wind, and - for ground-based observations, terrestrial day and year). As a consequence, long-term observations and their statistical study have proved necessary to disentangle and understand the observed phenomena. We have built a database from the available 26 years of systematic, daily observations carried on at the Nançay Decameter Array and recorded in digital format. This database contains all observed emissions, classified with respect to their dominant circular polarization, time-frequency morphology, and maximum frequency. We perform a first statistical analysis of its content. We confirm the earlier classification in Io-A, -A', -B, -C, -D and non-Io-A, -B, -C types, but we also identify new emission components: Io-A", Io-B' and non-Io-D. We determine the exact contours of all emission components in the $CML-\Phi_{Io}$ (Central Meridian Longitude versus Io Phase) plane, providing representative examples of their typical time-frequency shapes, and the distribution of emission's maximum frequency as a function of Λ_{Io} (Io's Longitude). We present general statistical results on each component's occurrence rate, duration, intensity and polarization. We also develop a study of the long-term variabilities (declination, solar activity and synodic period) and we show how they can affect the occurrence probability in the CML-Φ_{Io} plane and their implication.

Keywords: Jupiter. Decameter Radio emissions. Catalog. Io-DAM. non-Io-DAM. Io controlled emissions. Io independent emission. Long-term Variability. Declination. Solar activity. Synodic period.

vii

ESTUDO DA VARIABILIDADE DAS EMISSÕES JOVIANAS DE RÁDIO DE ALTA LATITUDE USANDO 26 ANOS DE DADOS DO ARRANJO DECAMÉTRICO DE NANÇAY

RESUMO

Júpiter é uma complexa fonte de rádio na faixa decamétrica. As emissões são anisotrópicas, intrinsecamente variáveis na escala de tempo de milissegundos a horas, e moduladas por diversos processos em escala de tempo mais longas, de $\sim$10h a meses ou anos (dia e ano Joviano, sazonalidade, atividade solar e vento solar, e para observações terrestres, dia e ano terrestre). Como consequência, as observações de longo prazo e seu estudo estatístico requerem a necessidade de separar e compreender os fenômenos observados. Nós construímos um catálogo a partir de 26 anos de dados disponíveis de observações sistemáticas, diariamente realizadas pelo Arranjo Decamétrico de Nançay e gravados em formato digital. Esta base de dados contém todas as emissões observadas e classificadas levando em conta a sua polarização circular, morfologia no plano tempo-frequência e máxima frequência. Realizamos uma primeira análise estatística de seu conteúdo. Nós inicialmente validamos a classificação das fontes Io-A, -A', -B, -C, -D e non-Io-A, -B, -C, mas também identificamos novas componentes de emissão: Io-A", Io-B' e non-Io-D. Nós determinamos os contornos exatos de todas as componentes de emissão em CML-Φ_{Io} (Longitude do meridiano central versus Fase de Io), fornecendo exemplos representativos de suas formas típicas de tempo-frequência, e a distribuição de frequência máxima de emissões como uma função de Λ_{Io} (Longitude de Io). Apresentamos resultados estatísticos gerais, sobre cada componente, da taxa de ocorrência, duração, intensidade e polarização das emissões. Também desenvolvemos um estudo das variabilidades de longo período (declinação, atividade solar e período sinódico) e mostramos como elas podem afetar a probabilidade de ocorrência no plano CML-Φ_{Io} e suas implicação.

Palavras-chave: Júpiter. Rádio. Emissão decamétrica. Catalogo. Io-DAM. non-Io-DAM. Emissões controladas por Io. Emissões não controladas por Io. Longos períodos. Variabilidade. Declinação. Atividade Solar. Período sinódico.

LIST OF FIGURES

LIST OF TABLES

CONTENTS

1 INTRODUCTION

The decametric radio (DAM) emissions from Jupiter were discovered in 1955 by Burke and Franklin (1955). Shortly thereafter, it was observed that the emissions are strongly modulated by planetary rotation. A rotating Jovian longitude system called System III was defined, which shows a current period of 9 h 55 min 29.71 s (HIGGINS et al., 1997). Bigg (1964) discovered that the Io satellite controls a large part of the DAM emissions. For convenience, these emissions are called Io-emissions and the others (not controlled by Io) are called non-Io-emissions. Soon after, Bigg (1966) found a possible effect from Europa satellite in Io-emissions. However, it was argued that due to the observation geometry it would take over 20 years of homogeneous records to determine the combined effects of the satellites, which even so could be disguised by unrelated long-period changes (BIGG, 1966). The Voyager and Galileo spacecraft data have shown a possible control of Europa, Ganymede and Callisto in non-Io-DAM with frequency less than 6 MHz (MENIETTI et al., 1998; MENIETTI et al., 2001; HIGGINS et al., 2006). However, no evidence of effect or control of the other Galileo satellites in DAM emissions, in ground-based observations, have been found to the present day.

Wu and Lee (1979) proposed a generation mechanism, called Cyclotron Maser Instability (CMI), to explain the Earth's Auroral Kilometric Radiation. Soon, this mechanism has been convincingly identified as responsible for generating the DAM emissions from Jupiter (ZARKA, 1998; TREUMANN, 2006). Carr et al. (1983) showed four typical shapes of Io-Jupiter radio arcs that may be observed in the time-frequency plane, related to the so-called Io-A, -B, -C and -D "sources". Queinnec and Zarka (1998) deduced, from a 3D geometrical analysis of a few arc shapes, that these four shapes are caused by the anisotropic beaming generated by CMI at large angles from the local magnetic field, and the source-observer geometry. These sources actually correspond to the vicinity of the northern (A & B) and southern (C & D) Io flux tube footprints, seen from either side of the radio emission cone, i.e. when Io is at the eastern (A & C) or western (B & D) limbs of Jupiter (ZARKA, 1998; HESS et al., 2008). Identical Io-Jupiter-observer geometries lead to identical radio arc shapes observed. Currently, this idea is used in the Exoplanetary and Planetary Radio Emission Simulator (ExPRES) to simulate the arc shapes from Jupiter, Saturn and exoplanets (HESS et al., 2008; LAMY et al., 2008; HESS; ZARKA, 2011).

Since the late 70s, several evidences have been showing that non-Io DAM and Hectometric (HOM) emissions seem to respond to solar wind variations (TERASAWA et

al., 1978; BARROW et al., 1986; ZARKA; GENOVA, 1983; GENOVA et al., 1987; ZARKA; GENOVA, 1989; BOSE; BHATTACHARYA, 2003; ECHER et al., 2010b; HESS et al., 2012; HESS et al., 2014), however, the precise positions of the non-Io DAM sources are unknown.

Due to the high variabilities in DAM emissions (in source region, observation geometry and interplanetary medium), systematic observations have been carried out at various ground based radio observatories since shortly after the discovery of Jovian DAM, in Boulder (WARWICK et al., 1975), at Florida station (THIEMAN et al., 1975) and at Nançay (BOISCHOT et al., 1980) and several catalogs of the detected emissions were built until the early 90s (WARWICK et al., 1975; THIEMAN, 1979; LEBLANC et al., 1981; LEBLANC et al., 1983; LEBLANC et al., 1989; LEBLANC et al., 1990; LEBLANC et al., 1993). However, no catalog was built after the 90s, but, systematic observations are still developed by Nançay Decametric Array (NDA), France, in digital format.

Consequently, this thesis proposes to use the arc shape properties to create a new catalog of the detected emissions using 26 years (1990-2015) of data from NDA, and to develop a statistical study to validate it. We also propose to develop a study of long-term variabilities of DAM emissions. To achieve this goal, this thesis is structured as follows: Chapter 2 introduces the DAM emissions and the magnetospheric processes that can trigger it; Chapter 3 describes the NDA, the catalog building process and the classification criteria of emissions; Chapter 4 shows the catalog, the statistical analysis as well as the conclusion of this part; Chapter 5 develops a long-term variability study in the DAM emission as well as the conclusion of this study. Finally Chapter 6 summarizes the contribution of the work as well as new prospects for the future.

2 AURORAL RADIO EMISSION

In the solar system all magnetized planets, i.e., Earth, Jupiter, Saturn, Uranus and Neptune emit auroral radio emissions (AREs). AREs are intense and non-thermal emissions and extend from few kHz to tens of MHz (ZARKA, 1998). Figure 2.1 shows the average spectra of all AREs, including Io-Jupiter emissions (Io-DAM) and S-bursts (S for Short). It is observed that the AREs from Jupiter are the most intense and show a broader spectral range. However, due to the Earth's ionosphere cut-off at $\sim$ 10 MHz (see dotted line in Figure 2.1) only the decameter range from Jupiter is detected from the ground-based observations.

Figure 2.1 - Spectra of auroral radio emissions from all magnetized planets in the solar system. Average emission levels are sketched, normalized to a distance of 1 AU from the source.
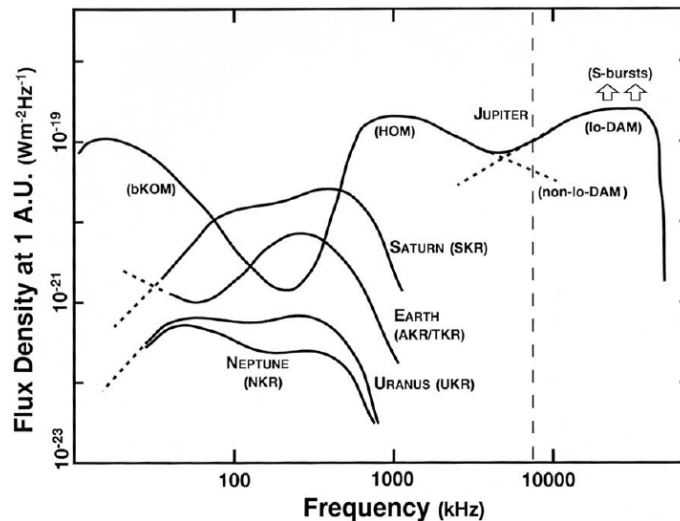
The dotted line indicates the cut-off of the Earth's ionosphere.
SOURCE: From Zarka (1998).

2.1 Decametric radio emission from Jupiter

The Jupiter DAM emission has been studied, from the ground-based observations since 1955, when it was discovered by Burke and Franklin (1955). Later, observations from space, through missions such as Voyager 1 and 2, Ulysses, Galileo, Cassini, Wind and Stereo, extended the observations to lower frequency. Since then, Jupiter has shown to be a complex and variable source of DAM emission, consisting of

3

several components modulated at all timescales from milliseconds to weeks or months (LECACHEUX et al., 2004, e.g):

- Milliseconds to seconds: S-bursts (GALLET, 1961; RYABOV et al., 2014);

- Seconds to minutes: interplanetary and ionospheric scintillations (GENOVA et al., 1981), modulation lanes (IMAI et al., 1992);

- Minutes to hours: arcs in the time × frequency plane (BOISCHOT; AUBIER, 1981; HESS et al., 2007);

- Tens of hours: planetary rotation (HIGGINS et al., 1997);

- Days to months: response to solar wind (HESS et al., 2012) and possibly seasonal variations (not identified yet).

Figure 2.2 - An example of an arc of DAM emission observed at Nançay and Wind Space-craft over their whole frequency range.
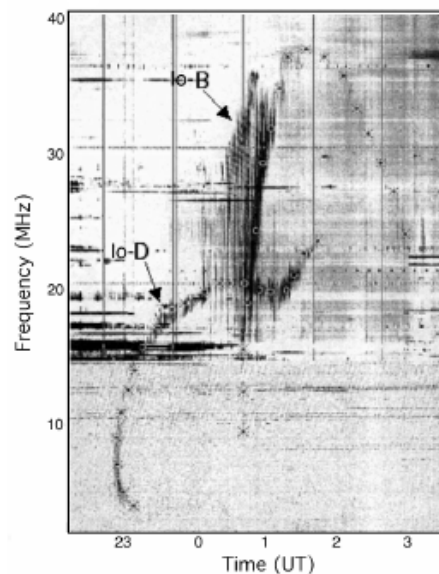
SOURCE: Adapted from Queinnec and Zarka (1998).

In special, at a timescale longer than ∼1 minute (from this point in this thesis it will be treated only this type of emissions), most of the observed variations in DAM

emission (but, not all, e.g. solar wind influence on the Jovian magnetosphere - (HESS et al., 2012)) are related to visibility effects, i.e. by Io-Jupiter-observer geometries.

Figure 2.3 - The number of emissions observed at Boulder and at Nançay as a function of CML.
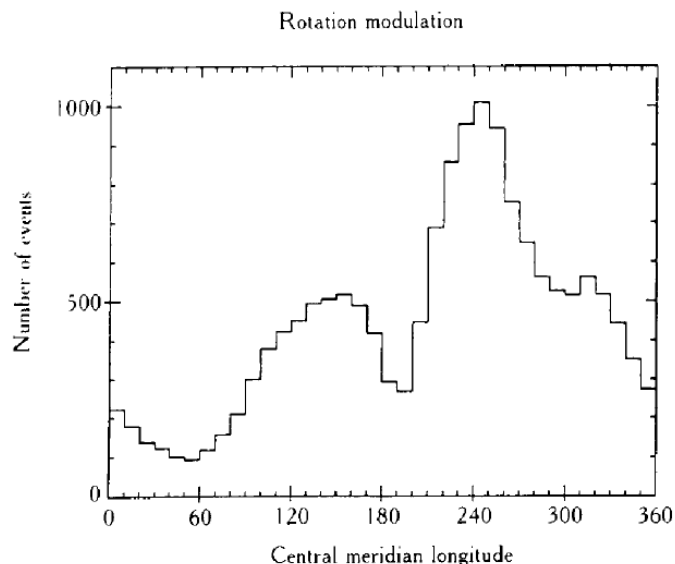
SOURCE: Adapted from Genova et al. (1989).

In the time × frequency (t-f) domain, DAM emissions are sporadic and observed in form of arcs (BOISCHOT; AUBIER, 1981; HESS et al., 2007). Figure 2.2 shows an example of a typical DAM emission detected at NDA and Wind Spacecraft. The events are similar to "storms", and they are mostly organized as a function of the Jovian Central Meridian Longitude (CML) or observer's Jovicentric longitude, as shown in Figure 2.3. The definition of CML is shown in Figure 2.4. The observations of DAM emissions over a long period of time gives an accurate estimate of the planet rotation time[1]: 9 h 55 min 29.71 s (HIGGINS et al., 1997). This characteristic is known as modulation by planetary rotation.

Another important feature of DAM emissions occurs due to the electrodynamic interaction between the Io satellite and the Jovian magnetosphere, where Io controls a large part of the DAM emissions (BIGG, 1964). This modulation is clear when the

---

[1]Jupiter has three systems of rotation: System I (defined from the clouds near equator), System II (defined from the clouds in high latitude) and System III (defined from the magnetospheric rotation).

Figure 2.4 - Definition of CML (defined by the System III (1965) of rotation), Io phase Φ_{Io} and longitude Λ_{Io}, lead angle δ_a, phase and longitude of the radio-emitting "active" field line.
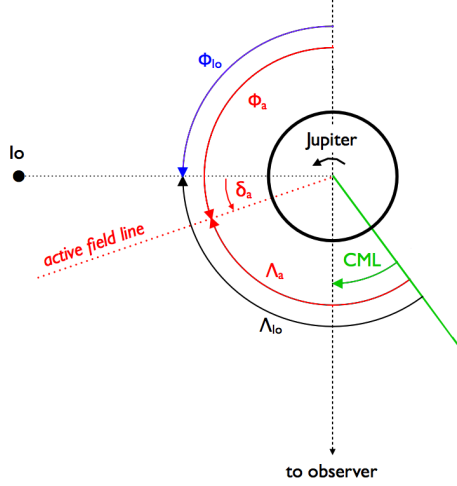
CML is shown in green; Φ_{Io} is shown in blue; Λ_{Io} is shown in black and δ_a is shown in red.

SOURCE: From Marques et al. (submitted to A&A).

occurrence of emissions is shown as a function of the phase of the Io[2] (Φ_{Io}). In Figure 2.5, the DAM occurrence shows two strong peaks at the Io Phase $\sim$90° and $\sim$240°, revealing the existence of an Io-Jupiter electrodynamic interaction which causes electron acceleration and consequently DAM radio emission (more detail will be shown later).

Based on the Io effect, Bigg (1964) and others (CARR et al., 1983; GENOVA et al., 1989) split DAM in two groups, one related to Io (and called "Io-DAM") and other that is not related to it (non-Io-DAM). Furthermore, when the emission occurrence is plotted as a function of CML and Φ_{Io}, Io-DAM appears clearly in 4 main regions of enhanced occurrence probability limited in both CML and Φ_{Io}, whereas non-Io-DAM appears in intervals of CML independent of Φ_{Io}. Those regions have been labelled A, B, C and D as shown in Figure 2.6.

Further studies showed that these occurrence regions actually correspond to two physical sources, one in each hemisphere. Furthermore, they showed that the emissions are strongly anisotropic, being produced by each point source along the walls

---

[2]The convention is to count the phase of Io along its orbit in the direct sense from an origin located in the anti-observer direction, see Figure 2.4.

Figure 2.5 - The number of emissions observed at Boulder and at Nançay as a function of
Io phase.
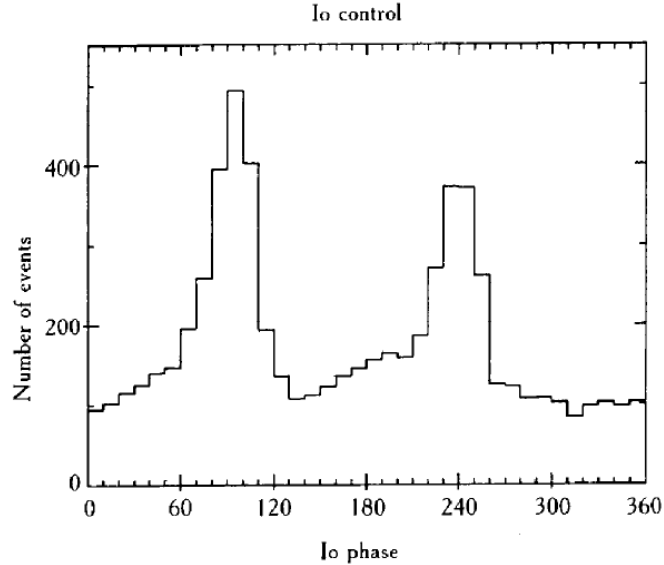
SOURCE: From Genova et al. (1989).

of a hollow cone centered on the magnetic field line in the source, whose aperture varies with frequency but is wide in most of the DAM frequency range (QUEINNEC; ZARKA, 1998; HESS et al., 2007). The sources are distributed along Jovian magnetic field lines, where precipitation of electrons (with keV energies) occurs, caused either by Io-Jupiter electrodynamic interaction or by the auroral activity. At each altitude, the emission is produced at/near the local electron cyclotron frequency (ZARKA, 1998; HESS et al., 2007).

In the decameter range, these sources extend from the planetary surface to an altitude of a few tenths of Jovian radius. The generation mechanism has been convincingly identified as the Cyclotron Maser Instability, similar to the generation mechanism of Earth's Auroral Kilometric Radiation (WU; LEE, 1979; ZARKA, 1998; TREUMANN, 2006).

2.2 Cyclotron Maser Instability

The Cyclotron Maser Instability (CMI) is a resonant interaction created due to an electron distribution with a relativistic speed $\vec{v}$ gyrating around magnetic field lines with a cyclotron frequency ω_c (where $\omega_c = eB_0/m$, and B_0, e and m are respectively

Figure 2.6 - CML $\times$ Io phase of DAM emissions observed at Boulder and at Nançay.
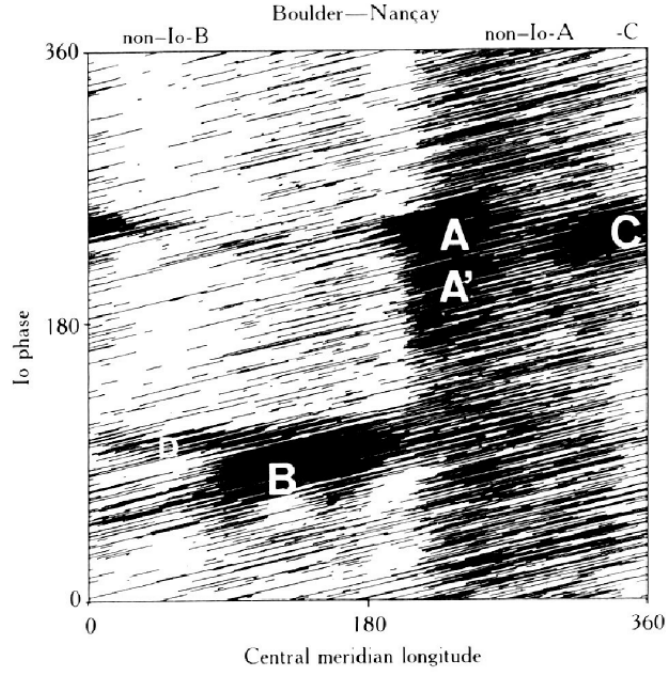
Io-DAM emissions appear like irregular shaped regions in the diagram while non-Io-DAM emissions are distributed in vertical bands. Those regions have been labelled A (A' only for Io-emissions), B, C and D.

SOURCE: From Genova et al. (1989).

the magnetic field strength, modulus of the charge and mass of the electron) and an elliptically polarized wave, with frequency ω and wave vector $\vec{k}$. Wu and Lee (1979), Wu (1985) and Galopeau et al. (2004) have calculated the CMI growth rate ω_i shown here,

$$\omega_i = \frac{\omega_p^2}{8} \int_0^{+\infty} v_\perp^2 dv_\perp \int_{-\infty}^{+\infty} \frac{\partial f}{\partial v_\perp} \delta \left(\omega - k_\parallel v_\parallel - \frac{\omega_c}{\gamma} \right) dv_\parallel, \qquad (2.1)$$

where $f(v_\parallel, v_\perp)$ is the normalized electron distribution function, ω_p is the plasma frequency ($\omega_p^2 = ne^2/m\epsilon_0$, where n is the electron density), γ is the relativistic Lorentz factor and the subscripts $_\parallel$ and $_\perp$ refer to the direction of the local magnetic field in the source and perpendicular to it, respectively. If the reader is interested in to get more details of how we can obtain the growth rate of the CMI, please see APPENDIX A.

The wave-particle resonance is reached when the Doppler shift frequency of the wave in the electron reference frame $(\omega - k_\parallel v_\parallel)$ is equal to the gyrofrequency of the resonant electron (ω_c/γ). The resonant condition is:

$$\omega - k_\parallel v_\parallel = \omega_c/\gamma. \tag{2.2}$$

In the weakly relativistic approximation $(\gamma^{-1} \simeq 1 - v^2/2c^2)$ the resonance condition represents a circle in the velocity plane $(v_\parallel, v_\perp)$ with the center v_0 and the radius R given by:

$$v_0 = \frac{k_\parallel c^2}{\omega_c} = \frac{\omega}{\omega_c} cN \frac{\vec{k} \cdot \hat{b}}{k} \simeq c \frac{\vec{k} \cdot \hat{b}}{k} = c\cos(\theta), \tag{2.3}$$

$$R = \left[v_0^2 + 2c^2 \left(1 - \frac{\omega}{\omega_c} \right) \right]^{1/2}, \tag{2.4}$$

where $\hat{b}$ is the magnetic field unit vector (i.e. the CMI depends on the magnetic field direction) and N is the refraction index $(\simeq 1)$. θ indicates the direction of wave propagation, i.e., it is the radio beaming angle relative to the magnetic field in the source.

The dependence of the CMI on the magnetic field direction allows to observe a difference in the sense of polarization. In a northern magnetic hemisphere, $\vec{B}_0$ points outwards so that the angle $(\hat{k}, \vec{B}_0)$ is acute and the polarization of the emitted radio wave (relative to $\hat{k}$) is thus the same as the polarization of the magneto-ionic X mode generated by the CMI, i.e. Right Hand (RH) sense. In a southern magnetic hemisphere, $\vec{B}_0$ points inwards so that the angle $(\hat{k}, \vec{B}_0)$ is obtuse and the RH wave (relative to B_0) generated by the CMI is Left Hand (LH) sense relative to k. The observed polarization is thus LH in that case.

It was assumed that the radio emission occurs at the local electron cyclotron frequency $\omega_c = \omega = eB_0/m$. So this linear relation between the emission frequency, or the instantaneous maximum frequency, and the magnetic field strength permits to obtain the amplitude of the magnetic field at or/near the footprint of the emitting field line. However, due to the long wavelengths of the radio emissions, a very low angular resolution is obtained, so that we cannot pinpoint accurately the position of the radio source (ZARKA, 2004). Even without angular resolution, the radio emis-

sions can give the minimum values of the magnetic field strength at the surface of the planet. For example, if we take a determined longitude of Io, the maximum emitted frequency cannot be larger than the electron cyclotron frequency at the top of the Jovian ionosphere.

By integrating equation (eq. 2.1) along the resonant circle (eqs. 2.3 and 2.4), the growth rate of the wave is obtained, given by the relation:

$$\omega_i = \frac{\omega_p^2 c^2}{8\omega_c} \int_0^{2\pi} v_\perp^2(\theta) \nabla_{v_\perp} f(\vec{v}_0, \vec{R}(\theta)) d\theta. \tag{2.5}$$

The growth rate arises only if the gradient $\nabla_{v_\perp} f(\vec{v}_0, \vec{R}(\theta))$ takes positive values along at least a part of the resonant circle. Therefore, the distribution function plays a very important role in the amplification of radio waves by the CMI. In the Earth's auroral region, three electron distribution functions which obey the CMI condition are commonly observed:

a) Loss cone distribution function: implies in collisions in the atmosphere of electrons which penetrate almost parallel to the magnetic field;

b) The horseshoe/shell distribution, resulting from the acceleration, parallel to the magnetic field (steady state, possibly due to static electric fields);

c) The ring distribution, caused by acceleration parallel to the magnetic field at high latitudes (possibly impulsive, for example, due to Alfvén waves).

Galopeau et al. (2004) and Galopeau et al. (2007) used the loss cone distribution and the O6 model of Jupiter's magnetic field (CONNERNEY, 1993) to calculate the maximum rate of amplification generated by the CMI as a function of Io's longitude. The authors showed that some Jovian longitudes in the northern and southern hemispheres favor the radio decametric emissions and lead to a higher occurrence probability.

Hess et al. (2008) obtained the radio beaming angle using the equation (2.3) for a loss cone distribution:

$$\theta = \arccos \left[(v/c) / \left(1 - \omega_c/\omega_{c,max} \right)^{1/2} \right]. \tag{2.6}$$

They used this result to develop the ExPRES model to simulate the t-f arc shapes, shown in Figure 2.7, as a function of emission beaming, lead angle between the radio emitting field line and the instantaneous Io's field line and the electron energy.

Figure 2.7 - Dynamic spectra of typical arc shapes simulated for Io-emission.
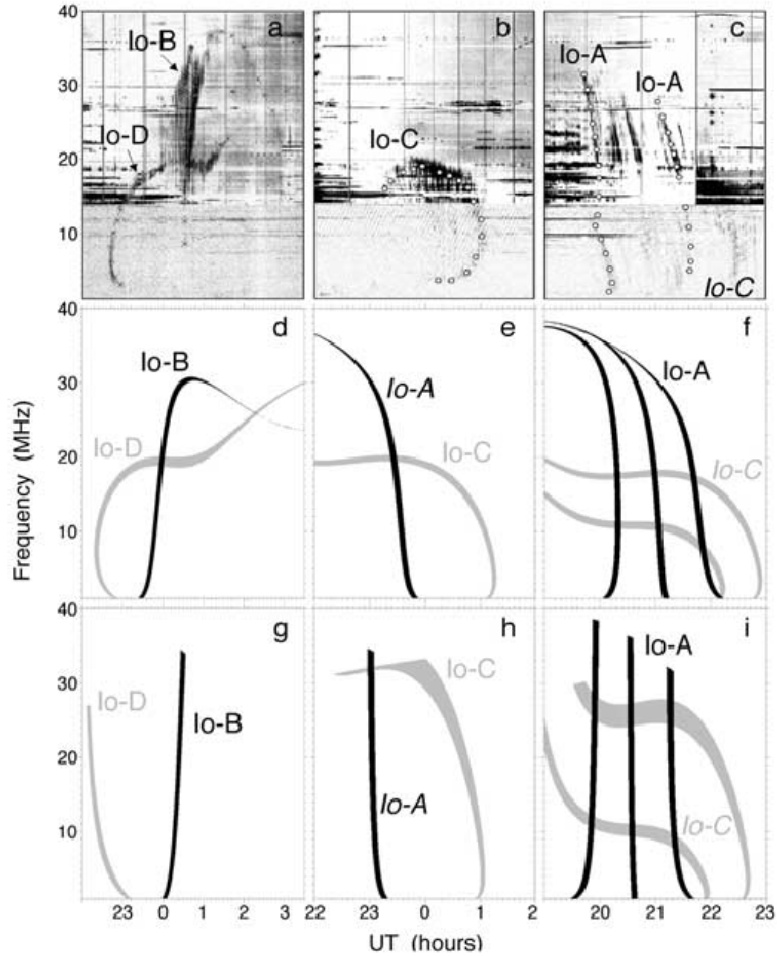
(a-c) typical Io-Jupiter arc shapes observed by Nançay and Wind Spacecraft and (d-f) arc shapes simulated for Io-emission using the equation (2.6). Black arcs are generated with RH polarization and grey with LH polarization. (g-i) the same that (d-f) except that $\theta(f)$ is taken constant and equal to $82°$.

SOURCE: From Hess et al. (2008).

In both studies the authors described a complex source structure (sources being distributed in a complex Jovian magnetic field, with strong contribution of multipolar terms in the range of altitudes corresponding to DAM). The anisotropic beaming

combined with the planetary rotation, the orbital motion of the Io and the variable latitude of the observer during the Jovian year cause the observed modulations in the emissions.

It was also observed, from CMI, that the magnitude and orientation of the magnetic field in the source region are important parameters in DAM emission. Thus, it is essential to know about the magnetic field in auroral region, although, the emissions are triggered in different parts of the magnetosphere and mapped by induction of field aligned currents to the auroral region. Hence, the auroral activity is a projection of magnetospheric processes (communicated via precipitating energetic particles) onto the atmosphere and thus they allow the studies of global processes not yet accessed by spacecraft (BAGENAL, 2007). Thus, Jupiter magnetosphere and its processes that can lead to acceleration of electrons, which in turn, generates the appropriate condition to CMI, will be briefly discussed below.

2.3   The Jovian magnetosphere and its processes

Because of its rapid rotation, strong magnetic field, with a magnetic moment of 4.2 G/R_J^3 (i.e. almost 18 times the Earth's magnetic field)[3] and an internal source of plasma, Jupiter creates the largest and most active planetary magnetosphere in the solar system, with wide dimensions and a large population of energetic particles that move in its magnetic field (KHURANA et al., 2004).

This powerful magnetosphere is strongly dominated by the rotation of the planet. It shows some structures similar to the ones observed in the Earth's magnetosphere and some unique structures in the solar system, for example, the plasma torus created by the Io satellite. Traditionally, Jupiter's magnetosphere is divided into three regions: inner ($< 10\ R_J$), middle (10 - $40\ R_J$) and outer ($> 40\ R_J$) magnetosphere (KHURANA et al., 2004). Each of these regions has distinct processes that can trigger the auroral emissions. Figure 2.8 shows a sketch of the magnetosphere (KHURANA et al., 2004).

The Jovian auroral region, shown in Figure 2.9, is responsible to display through the radio emissions, as well as by the ultraviolet (UV) and infrared (IR) emissions, the different processes occurring in the magnetosphere. It exhibits three regions: (1) Jovian magnetic footprints of the Galilean satellites; (2) a persistent and continuous auroral oval of emission encircling the magnetic pole; and (3) a time-variable and spatially-structured "polar cap" emission that partially fills the continuous oval, particularly its dusk half. These regions are apparently independent and physically

---

[3]Jupiter equatorial radius, where 1 $R_J = 71492$ km

Figure 2.8 - Sketch of the noon-midnight meridian of Jupiter magnetosphere.
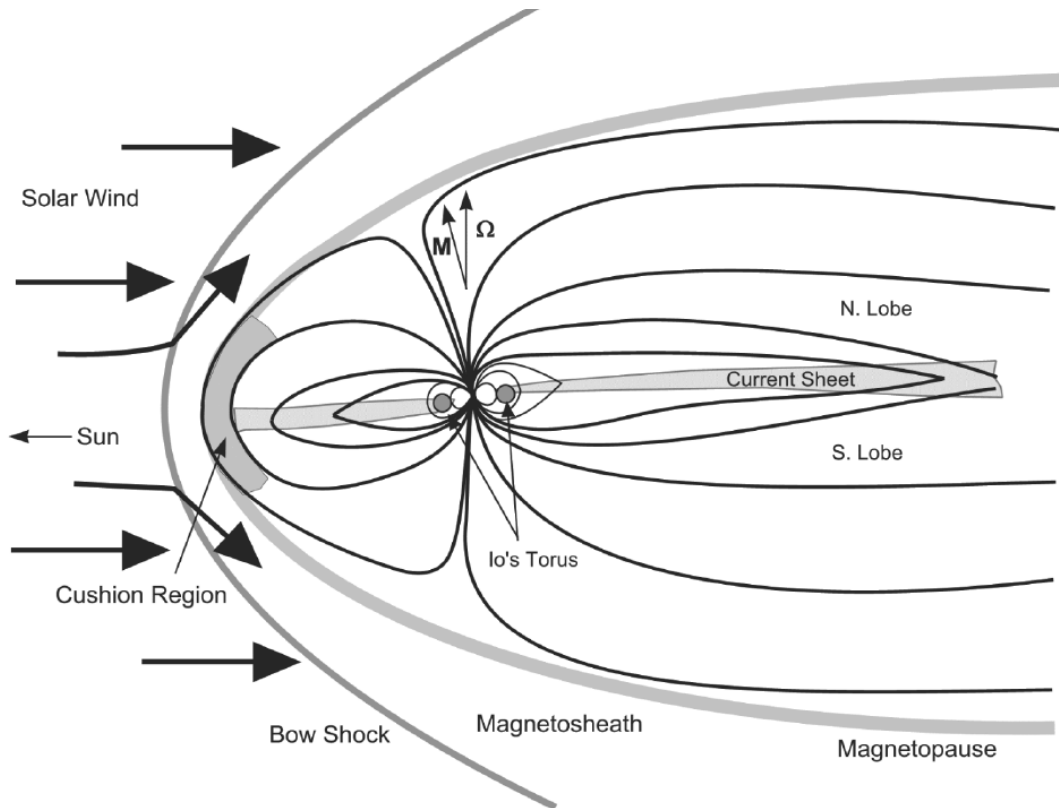
SOURCE: From Khurana et al. (2004).

separated from each other (CLARKE et al., 2004). They also show an asymmetry between the dawn and dusk sides of the northern aurora, which in part is due to an anomaly in the magnetic field caused by the rapid rotation of Jupiter.

2.3.1 Inner magnetosphere

The inner magnetosphere is the region extending up to 10 R_J. It is the main region of plasma production for the magnetosphere and also hosts the inner radiation belts. The magnetic field close to the planet is totally dominated by the field created by currents in the planetary interior (KHURANA et al., 2004).

The dense plasma torus created by the volcanic activity of Io is located between 5.2 and 10 R_J near the magnetic equator plane. It is the main source of plasma in the jovian magnetosphere, which is estimated to throw ∼1 $tons^{-1}$ of plasma in the magnetosphere (KHURANA et al., 2004).

Figure 2.9 - Hubble Space Telescope UV image of Jupiter northern auroral zone showing the satellite footprints (Io, Europa and Ganymede), the main and polar ovals, and also an asymmetry of the magnetic field.
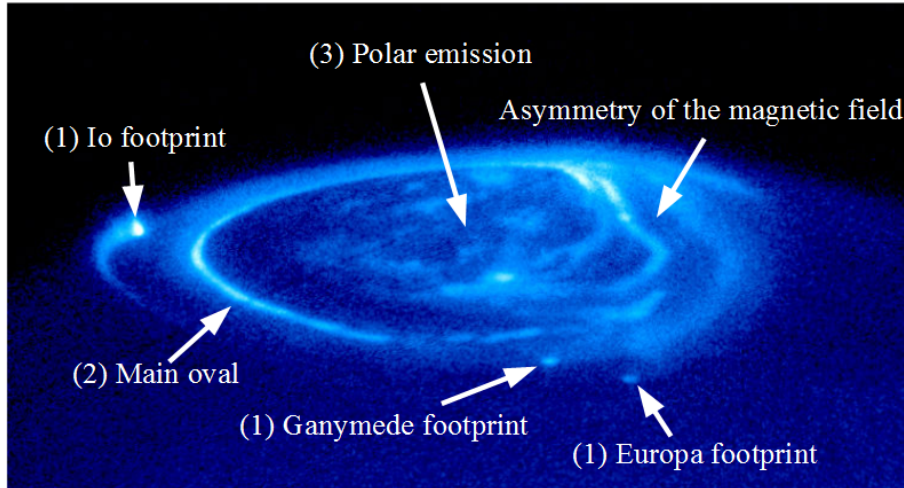
All regions are indicated in figure.

SOURCE: From Clarke et al. (2004).

The electromagnetic interaction between Io and Jupiter's magnetosphere is responsible for the most intense satellite-driven auroras which control a large part of the DAM emissions (BIGG, 1964), as well as bright UV spots and its downstream corotational wake at/near the Io flux tube (IFT) ionospheric footprints (PRANGÉ et al., 1996), seen in Figure 2.9. It is considered a secondary "auroral" source, occurring at slightly lower latitudes than the non-Io-DAM (ZARKA, 1998). That is, in the title of the thesis, "high latitude" was used instead of "auroral".

2.3.2 Middle magnetosphere

The middle magnetosphere is controlled by the magnetic field created due to the ring and sheet currents carried in the corotating plasmasheet that flows radially from the Io torus throughout the magnetosphere. It extends from 10 R_J to the region where the corotation of the plasma sheet breaks down completely, about 40 R_J (KHURANA et al., 2004; BAGENAL, 2007). This region creates a persistent and continuous oval of emissions (main oval) that circles the magnetic pole, shown in Figure 2.9, and it is mapped along magnetic field lines to 20-30 R_J at the equator in the magnetosphere, deeply inside the magnetopause. Thus the main aurora is not directly connected with the solar wind boundary (HILL, 2001).

The middle magnetosphere also hosts the other Galilean satellites (Europa, Ganymede and Callisto). Several studies used the Galileo and Voyager spacecraft data have shown a possible control of Europa, Ganymede and Callisto of non-Io-DAM emissions at frequencies lower than 6 MHz (MENIETTI et al., 1998; MENIETTI et al., 2001; HIGGINS et al., 2006). These results are consistent with the UV emissions at the footprints of Europa and Ganymede, shown in Figure 2.9. This demonstrates an electromagnetic connection between the satellites and Jupiter's magnetic field. This is explained by precipitating electrons and other particles moving on magnetic field lines which pass through the satellite. Additionally, it was discovered by Kivelson et al. (2004) that Ganymede has an intrinsic magnetic field, i.e. a separate magnetosphere. However, this possible control has not yet been observed to frequencies higher than 10 MHz, i.e., in ground-based observations.

Recently, Louarn et al. (2014) have observed in data from Galileo spacecraft a global disturbance of the magneticdisk responsible for energy and particle injection in the auroral regions. Figure 2.10 shows the sketch of this event. Such events have been observed in HOM emissions. However, it has been considered that non-Io-DAM and HOM emissions could be the same radio component, but emitted at different latitudes, i.e., along field lines with magnetic-L-shell = 7-9 for HOM, and L-shell > 9 for non-Io-DAM (LADREITER et al., 1994; ZARKA, 1998; ZARKA, 2004). Therefore, these events are strong candidates to trigger a part of the non-Io-emissions.

Figure 2.10 - Sketch of global disturbance of the magneticdisk.
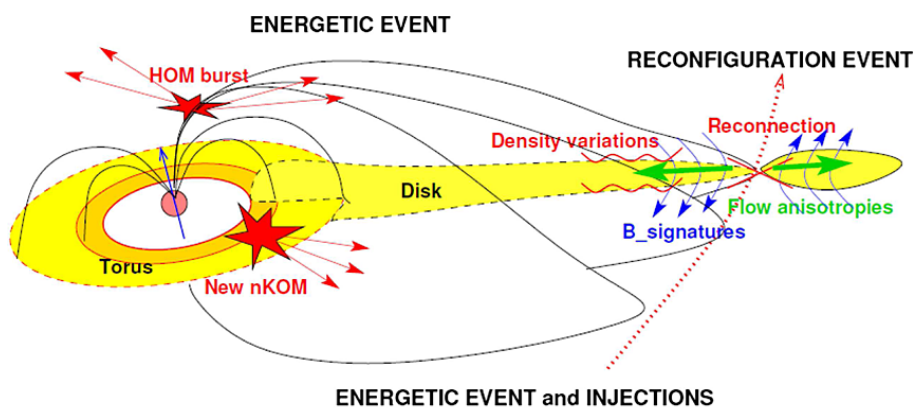
SOURCE: Adapted from Louarn et al. (2014).

2.3.3 Outer magnetosphere

For distances $> 60 \, R_J$ (or beyond the corotating plasmasheet) the magnetosphere is highly distorted due to the solar wind influence. This region exhibits the form of a teardrop that extends $100 \, R_J$ upstream (subsolar magnetopause distance), $200 \, R_J$ transverse to the solar wind, and beyond the Saturn's orbit downstream (magneto-tail). However, it shows large spatial and temporal variations as a direct response to changing solar wind pressure (SMITH et al., 1978; KRUPP et al., 2004). Several studies have shown the relationship between the solar wind variations and non-Io-DAM emissions (TERASAWA et al., 1978; BARROW et al., 1986; ZARKA; GENOVA, 1983; GENOVA et al., 1987; ZARKA; GENOVA, 1989; BOSE; BHATTACHARYA, 2003; ECHER et al., 2010b; HESS et al., 2012; HESS et al., 2014), however, this relation is complex.

As it was lastly discussed, the dependence of the solar wind conditions, the possible control by the other three Galileo satellites, with a correlation of HOM and UV auroral emissions, suggest that non-Io-DAM originates from Jovian magnetic field lines at higher invariant latitude than the Io-DAM. However, the precise positions of the non-Io-DAM sources are unknown.

2.4 Observation effects on DAM-emissions

Because the radio beaming occurs at a large angle from the magnetic field in the source and taking into account the planet rotation, each of these two sources may be observed from two viewing geometries, near each limb of the planet (QUEINNEC; ZARKA, 1998; ZARKA et al., 2011). A & B emissions thus originate in the northern hemisphere, respectively from the dusk and dawn sides of Jupiter as seen from the Earth, and C & D symmetrically from the southern hemisphere and respectively from the dusk and dawn sides.

The emission arc shapes were interpreted as resulting from the combination of the topology of the Jovian magnetic field, the radio beaming and the observation geometry (CARR et al., 1983; ZARKA, 1998; HESS et al., 2008). It exhibits an unique pattern for each emission region. B & D arcs show a so-called "vertex-early" shape (i.e. like an open parenthesis "("), whereas A & C arcs show a "vertex-late" shape (closed parenthesis ")"). As discussed earlier, the emissions from the northern hemisphere (A and B regions) show a dominant RH circular or elliptical polarization, whereas emissions from the southern hemisphere (C and D regions) are LH polarized.

The Jovicentric declination of the Earth (D_E), that varies by $\pm 3.3°$ over Jupiter's

11.9-year solar revolution period, strongly affects the CML and the occurrence probability of DAM emissions. This effect is also a geometrical one, resulting from the fact that the observers see different parts of a narrow emission beam that corotates with Jupiter during different apparitions of the planet (CARR et al., 1983).

In Figure 2.11 we have shown a general sketch of the geometry and arcs of emissions as viewed from the Earth.

Figure 2.11 - Schematic summary of geometry and arcs of DAM emissions as observed from Earth.
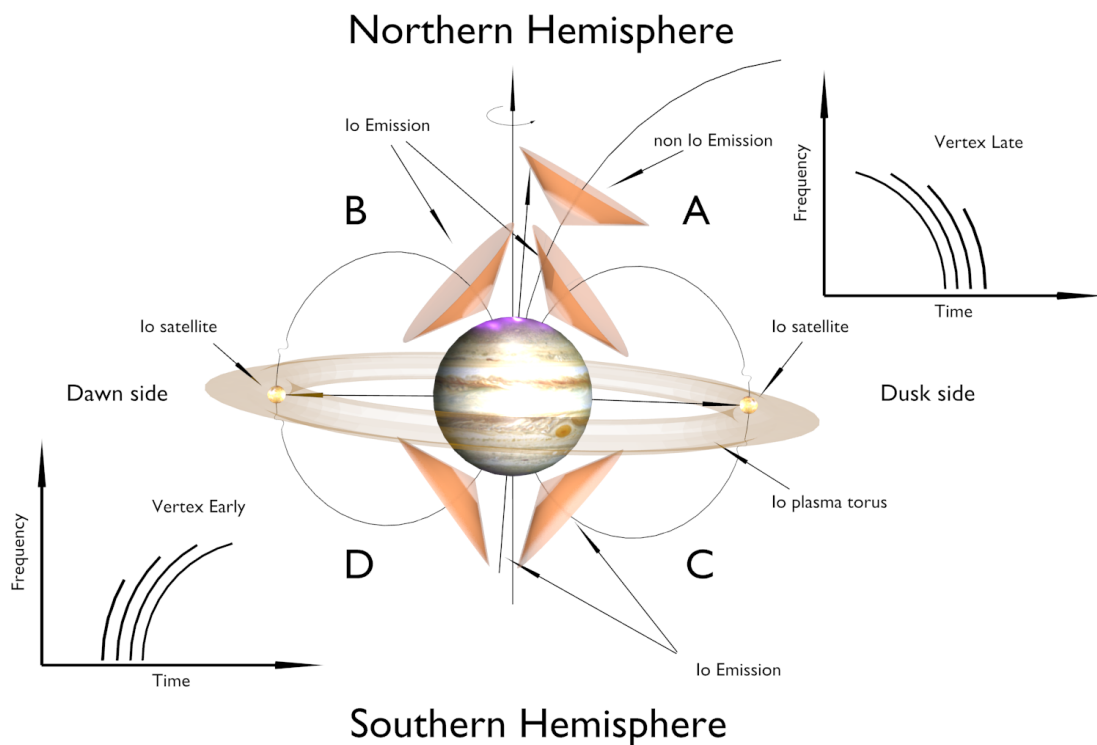
SOURCE: From Marques et al. (submitted to A&A).

2.5 Catalog of DAM-emissions

As a consequence of the complex source structure described above, the determination of many emission properties, that in turn constrain the generation scenario and its relation to the Jovian magnetosphere dynamics, requires statistical studies based on long-term observations, in order to disentangle the various phenomena superimposed at various timescales. This is why systematic observations (synoptic

17

monitoring programs) have been carried out at various ground based radio observatories since shortly after the discovery of Jovian DAM, e.g., in Boulder (WARWICK et al., 1975) and in Florida station (THIEMAN et al., 1975) and Nançay (BOISCHOT et al., 1980). Several catalogs of the detected emissions were built (WARWICK et al., 1975; THIEMAN, 1979; LEBLANC et al., 1981; LEBLANC et al., 1983; LEBLANC et al., 1989; LEBLANC et al., 1990; LEBLANC et al., 1993).

As discussed in chapter 1, the proposal of this thesis is to use the emission properties (discussed above) to create a new catalog of the detected emissions using 26 years (1990-2015) of data in digital format from NDA. Thus, this catalog will fill a gap in the period from 1990 to 2015. In the next chapter (3) will be described the instrumentation and the classification methodology adopted in this work.

3 INSTRUMENTATION & METHODOLOG

This chapter describes the Nançay Decameter Array (NDA) and the catalog building process as well as the classification criteria of emissions.

3.1 Nançay Decameter Array (NDA)

The Nançay Decameter Array, shown in Figure 3.1, is a moderate size phased array, built in 1975-77, consisting of 144 loc-conical (so-called "Tee-Pee") antennae, sensitive to the range ~10-100 MHz (BOISCHOT et al., 1980; LECACHEUX et al., 2004). The antennae have conical shape, with helical winding of the wires. 72 antennae are circularly polarized in the Right-Hand (RH or RHC) sense distributed in the form; 6 East-West x 12 North-South, and 72 in the Left-Hand (LH or LHC) sense. Each of the 72-antennae array are phased in two steps: by groups of 8 antennae, then through delay lines. Thus, NDA is effectively composed of two detection arrays, i.e., waves with right and left polarization may be observed. Each antenna has an effective area $\sim \lambda^{2/3}$, thus each polarized array of 72 antennae has an effective area ($A(m^2)$) iqual to $\sim 24\lambda^2$, limited to ~ 3500 m^2 due to the overlap of antenna effective areas at low frequencies, i.e., it is equivalent to a parabolic dish of ~ 67 m of diameter. The surface of this collector provides a gain of about 25 dB at 25 MHz. The system noise (System Equivalent Flux Density - SEFD) of the NDA is dominated by the galactic background noise ($T \sim 60\lambda^{2.55}$), and it is $\sim 10^4$ Jy at 40 MHz. However, NDA has low angular resolution (about $7° \times 14°$), which prevents the direct location of radio emission sources in the observed environment. Moreover, the compensation comes from the possibility to measure different polarizations (BOISCHOT et al., 1980; LECACHEUX et al., 2004).

Thus, the sensitivity of the instrument is limited. It has been largely dedicated to the systematic observation of the strong and variable decameter radiosources that are Jupiter and the Sun. Observations are carried out 8 hours/day for each target, i.e., from -4h to +4h of their times of meridian transit, when these times are distant enough. When Jupiter and the Sun are less than 8h apart in Right Ascension[1], priority is given to one target or the other according to the situation (high Solar activity, high probability of Io-emission, support observation campaign for a space mission).

Systematic/survey/synoptic observations of Jupiter at the NDA, called "Routine"

---

[1] It is the angular distance measured eastward along the celestial equator from the vernal equinox to the hour circle of the point in question (KEPLER; SARAIVA, 2004).

Figure 3.1 - Nançay Decameter Array.

observations, are performed since September 1990 by a swept-frequency analyzer that scans across the band 10-40 MHz, measuring alternately one spectrum of LHC polarized intensity and one spectrum of RHC polarized intensity (not full polarization). It is connected to a PC that ensures digitization and data acquisition. The sweep takes 500 msec per spectrum, i.e. 1 sec between two consecutive spectra of the same polarization. 400 frequencies are explored, i.e. a frequency step of 75 kHz, with a filter width equal to 30 kHz. They are scanned consecutively, i.e. ~1.2 msec / channel, hence a low sensitivity (SEFD/$(30000 \times 0.0012)^{1/2}$ ~SEFD/6~10^3 Jy).

"Routine" data consist of 2 dynamic spectra, i.e., intensity shown as a function of time and frequency, with 1 sec × 75 kHz resolutions in LHC & RHC for ~8 hours, each day, see Figure 3.2. Every hour, a calibration sequence (4 steps of 10 sec each) with broadband noise (from noise sources) is inserted instead of the sky signal at 4 different levels (lowest than sky, and the 3 others = +10 dB each, starting with strongest) at 8-antenna blocks. The data represent ~3 Mbytes/second and they are stored on a disk, with quick-looks, built immediately after the observation. They are distributed via the NDA web server at the Nançay Radio Observatory (http://realtime.obs-nancay.fr/dam/data_dam_affiche/data_dam_

`affiche.php?init=1`).

Figure 3.2 - Example of NDA "Routine" dynamic spectra.
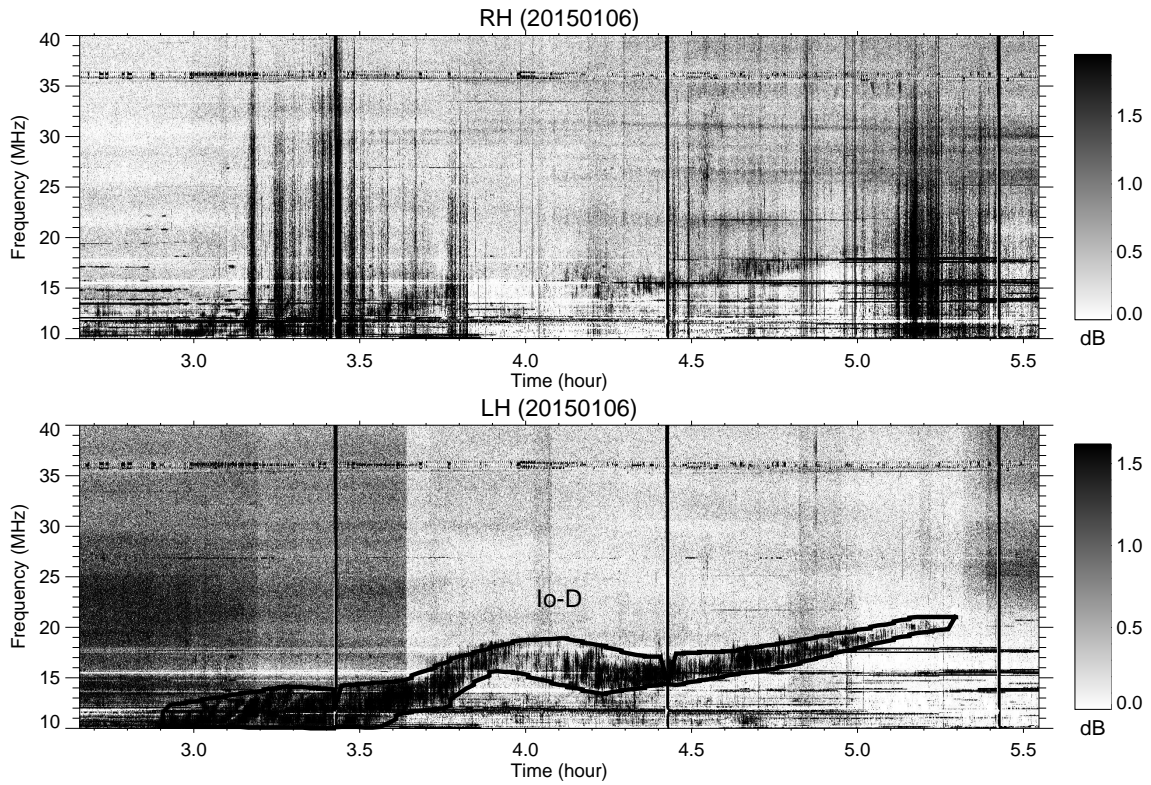
3.2   The construction of the catalog

As explained in chapter 2, the determination of many DAM properties, constraining its generation scenario and its relation to the Jovian magnetospheric dynamics, requires statistical studies based on long-term observations. Several catalogs of Jovian DAM have been constructed from the NDA data since the start of its operations (LEBLANC et al., 1981; LEBLANC et al., 1983; LEBLANC et al., 1989; LEBLANC et al., 1990; LEBLANC et al., 1993), from the visual examination of recorded dynamic spectra in printed form (on paper or 35 mm film). The listed information in the catalogs is generally restricted to the spectral range covered, (start & end) times and (minimum & maximum) frequencies as well as (start & end) positions in the CML-Φ_{Io} plane.

In order to build a more informative digital database of Jupiter emissions over about ∼54.578 hours of observations by NDA recorded from September 18 of 1990 to December 31 of 2015, a specific tool was designed for interactively displaying and cataloguing the emissions. This software, illustrated in Figure 3.3, was developed by the Paris Observatory. It displays both dynamic spectra (LH and RH), simultaneously, with a time-integration and a contrast (that may be adjusted manually), thus enabling to catalog the emissions that they contain.

Figure 3.3 - Construction of the catalog: interactive step #1.
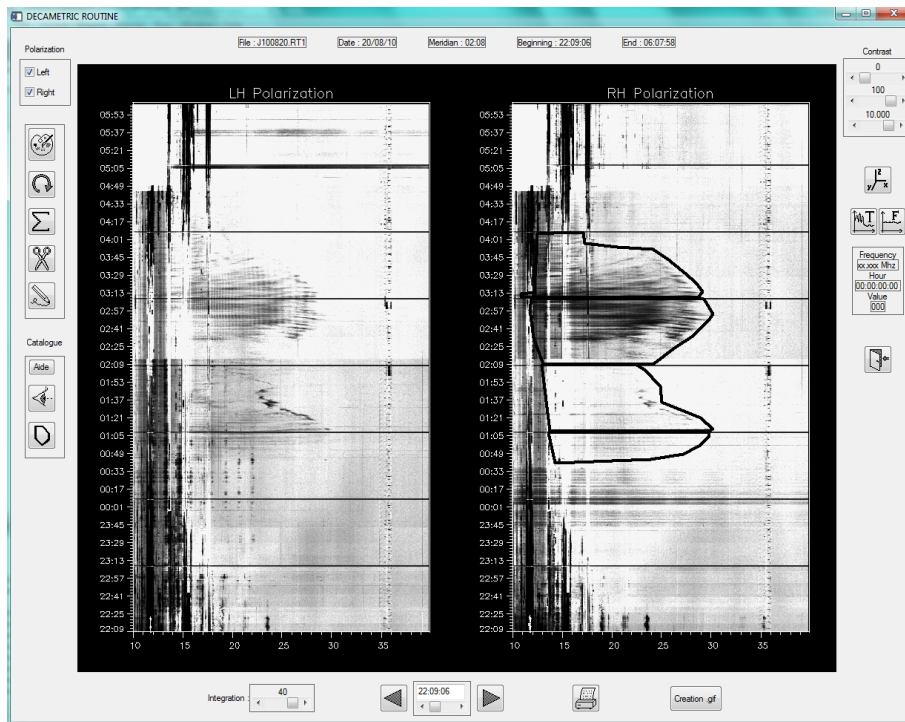
Emission recognition is visual, because no automated procedure is available at present to recognize efficiently Jupiter emissions and distinguish them from Radio-Frequency Interference (RFI - e.g. radio broadcast stations, RADAR, lightning, etc.). Following visual identification of an emission on the dynamic spectrum of the polarization (LH or RH), where this emission is more intense, a polygonal contour is drawn around each emission (with the mouse) and the emission type is selected following the criteria.

The method to recognize emissions consists in using the shape of the emission along

Table 3.1 - Criteria for cataloguing each emission type adopted in this work

Source	Maximum Frequency (MHz)	Dominant polarization	Arc curvature (vertex)
Io-A	38	RH	late
Io-B	40	RH	early
Io-C	30	LH	late
Io-D	30	LH	early
non-Io-A	38	RH	late
non-Io-B	38	RH	early
non-Io-C	32	LH	late
non-Io-D	24	LH	early

Figure 3.4 - Example of Io-emission arcs used in the construction of the catalog.
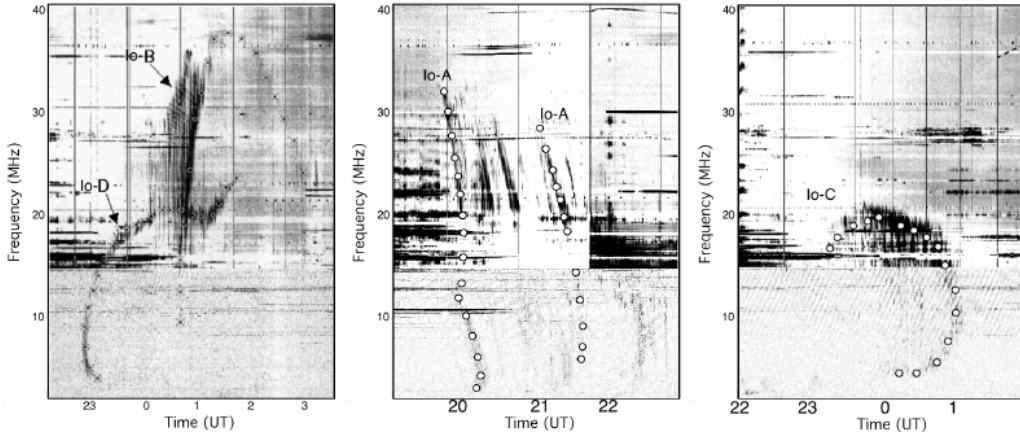
SOURCE: Adapted by Hess et al. (2010) from Queinnec and Zarka (1998).

with its polarization and maximum frequency, as described in chapter 2, to discriminate the emissions from different sources. The method allows to separate emissions of different types that are located in overlapping regions in the "CML-Φ_{Io}" diagram. After extensive examination of hundreds of emissions and crossing the above described parameters and comparing observations with known emission types discussed in the literature, the basic criteria was defined to catalogue each emission type, as listed in Table 3.1. In Figure 3.4, examples of the Io-emission arcs, which have typical shapes, are shown. They were well described by Queinnec and Zarka (1998). Unfortunately non-Io-emissions are highly variable, so, they do not exhibit

a characteristic emission envelope like the Io ones. Therefore we have used only the curvature of the arcs together with the other properties listed.

Figure 3.5 - Construction of the catalog: merging polygons and computing fmin and fmax at 1-min resolution (step #2).
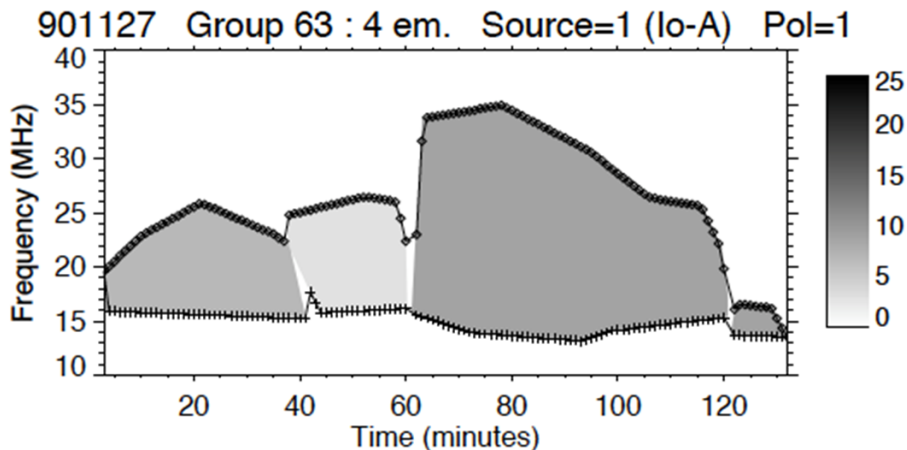
For each emission, the software calculates the minimum and maximum frequencies, the start and end times, the average intensity ($<$I$>$ in dB above the background) of the emission inside the contour, the average intensity in the symmetrical contour in the dynamic spectrum of opposite polarization, and the circular polarization ratio (Stokes parameter V, computed as ($<$ILH$>$-$<$IRH$>$)/($<$ILH$>$+$<$IRH$>$)). Average intensities and polarization are computed over the pixels above the background inside the emission contour. The background corresponds to the Galactic background and is computed at each frequency from the whole daily observation file. True intensity may be reconstructed from the value in dB and the background flux density $S = 2kT/A$ with $T(K) \sim 60\lambda^{2.55}$ and $A(m^2) = min(24\lambda^2, 3500)$. All these parameters characterizing globally the emission are stored in the database. All this process was developed during the visit in Paris Observatory and took a year.

After this step, each contour is interpolated at t-f envelope at 1 min resolution and merged in a simple emission, with global characteristics recomputed accordingly, for emissions of the same type on the same day separated by less than 10 minutes. For this step we developed a program in IDL language. The interpolated frequency shows an accuracy estimated to be better than ±300 kHz (4 channels, resulting

24

from the uncertainty in the visual determination of the emission limits and the subsequent interpolation of the contour). This step is illustrated in Figure 3.5. All these parameters together with the observation parameters are stored in a database. When the emissions are not detected during an observation, only the observation parameters are stored.

Finally, the complete ephemeris (CML, phase and longitude of Io, and of the other Galilean satellites and Amalthea, Jovicentric latitude of the Earth (usually noted D_E) and of the Sun, Right Ascension) are computed for each observation and emission at a timescale of 1 minute and stored in the database, in order to be easily available when exploiting the catalogue. Ephemeris were calculated using JPL's Horizons system (`http://ssd.jpl.nasa.gov/horizons.cgi`).

The phase of the Io (Φ_{Io}), or of any other Jovian satellite, is the departure of its superior geocentric conjunction, measured in projection on Jupiter's equatorial plane. It was computed in four steps: (1) the CML, i.e. the Earth's Jovicentric longitude, is obtained from the ephemeris server, at consecutive observation times at Earth t_E, taking into account the light travel time between Jupiter and Earth dt_E ; (2) Io's longitude Λ_{Io} is obtained similarly, setting Io as the observer, at consecutive times at Io t_{Io} with a light travel time dt_{Io} ; these angles are recomputed as a monotonously increasing series over the 26 years studied ; (3) Λ_{Io} is re-interpolated from a time axis t_E to a time axis $t_E - (dt_E - dt_{Io})$, to correct for the different travel times ; (4) the phase, e.g. of Io, is derived as $\Phi_{Io} = CML - \Lambda_{Io} + 180°$, and angles are restored in the range $[0°, 360°]$. We also developed all this process using IDL language.

During the construction of the database, a few percent of the emissions appeared with all characteristics of a given emission type but with opposite polarization, or even sometimes when an emission started in one dominant polarization and then switched to the opposite polarization. The origin of the problem was identified as a desynchronization of the swept-frequency analyzer with the acquisition PC, resulting in a missing spectrum in the sequence of spectra recorded alternatively with LH and RH polarization, and thus to an apparent inversion of the polarization of the emission (only the rank of the spectrum in the file defines its polarization). This problem appears only at a few occasions during the 26 years studied, corresponding to specific observation set-ups (due to its rarity, that remained unnoticed until this work). This problem was solved by relying only on the other characteristics defining each emission type, and - in these particular cases only - on the occurrence in the

25

CML-Φ_{Io} plane. As a result the fraction of erroneously catalogued emissions were estimated in the final database, due to the polarization, to be $\leq 1\%$.

4 THE NDA JUPITER CATALOG

In this chapter the catalog and its validation will be shown through statistical analysis. These results will be compared, whenever possible, with the literature. We will also discuss the implication of the adopted classification criteria and the description the radio sources.

4.1 Catalog

The catalog is composed of 8163 observations that correspond to 54.578 hours of measurements. Figure 4.1 shows the distribution of the duration of the observations. The broad variation, from 1 hour (or less) to 10 hours, depends on various factors (technical and/or observational), but the vast majority lasted for ∼7.5 hours (the standard duration of a daily Routine observation). Longer observations occurred at specific occasions (e.g. the collision of debris from the comet Shoemaker-Lely 9 with Jupiter in 1994), while shorter ones depend on the competition with NDA Solar observations or technical factors.

Figure 4.2 shows the occurrence of observations as function of CML and Φ_{Io}. Observations are decomposed into consecutive 1 minute intervals, and the figure displays the number of minutes of observation per $5° \times 5°$ bins. This number varies between 505 and 798 across the entire plane, over the 26 years interval analyzed. Inhomogenities of coverage results from previous knowledge about Io emissions: when Jupiter and the Sun are less than 8h apart in Right Ascension, priority is given to one target or the other according to the context. Jupiter was generally the priority when the observation track crossed a region of enhanced Io emission probability in the CML-Φ_{Io} plane, hence the coverage of Figure 4.2.

4.1.1 Emission tracks in the CML-Φ_{Io} plane and overall occurrence probabilities

In Figure 4.3, we show the catalog of emission tracks as function of CML and Φ_{Io} together with the corresponding overall emission occurrence probability versus CML (top) and Φ_{Io} (right). The source regions are indicated with different colors for each emission type as recorded in the catalog. The occurrence probability corresponds to the number of minutes of emissions per $5°$ bin of each coordinate and it has been normalized by the total number of observations in the same bin (see Figure 4.2). Addition results are shown in Appendix B.1.

From Figure 4.3, two important effects of DAM emissions can be seen. The first

Figure 4.1 - Duration of observations.
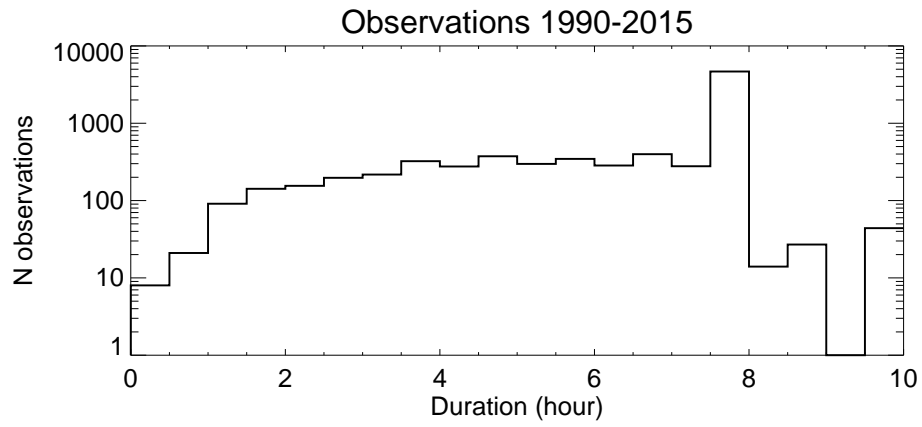
Figure 4.2 - Coverage of the CML-Φ_{Io} plane with observations.
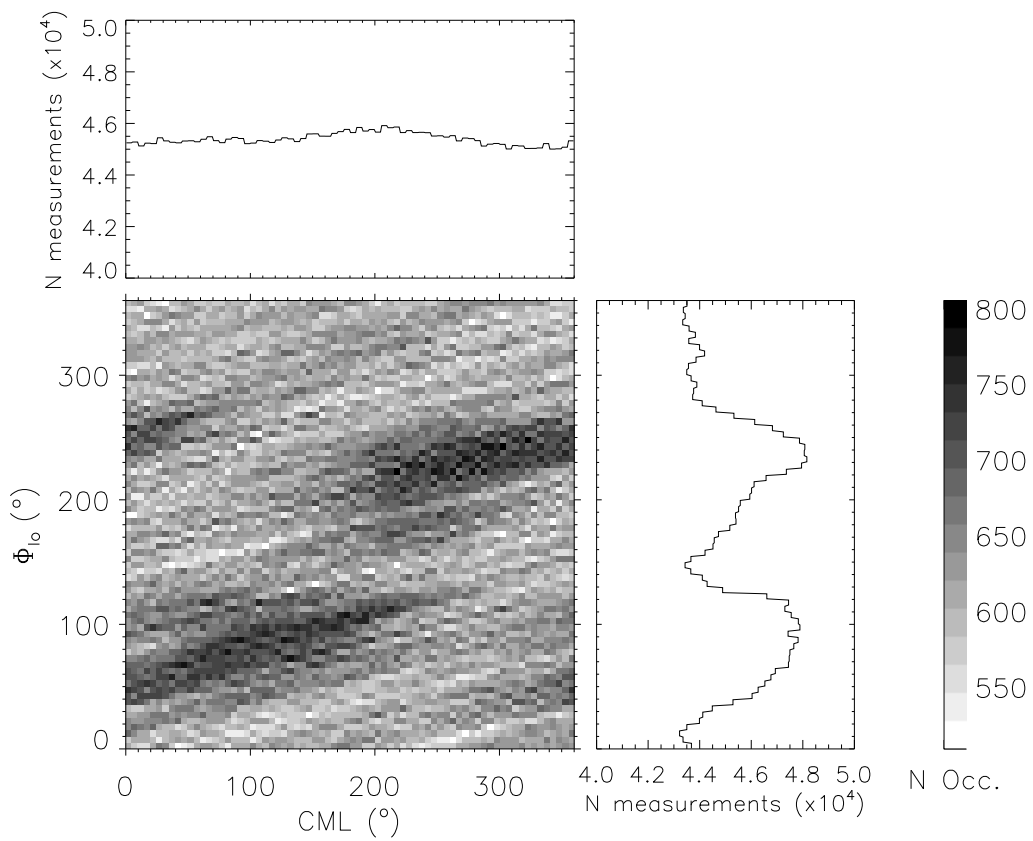
Figure 4.3 - Distribution of all emissions in the CML-Φ_{Io} plane. Tracks $\longrightarrow$ possible over-lap of some emissions.
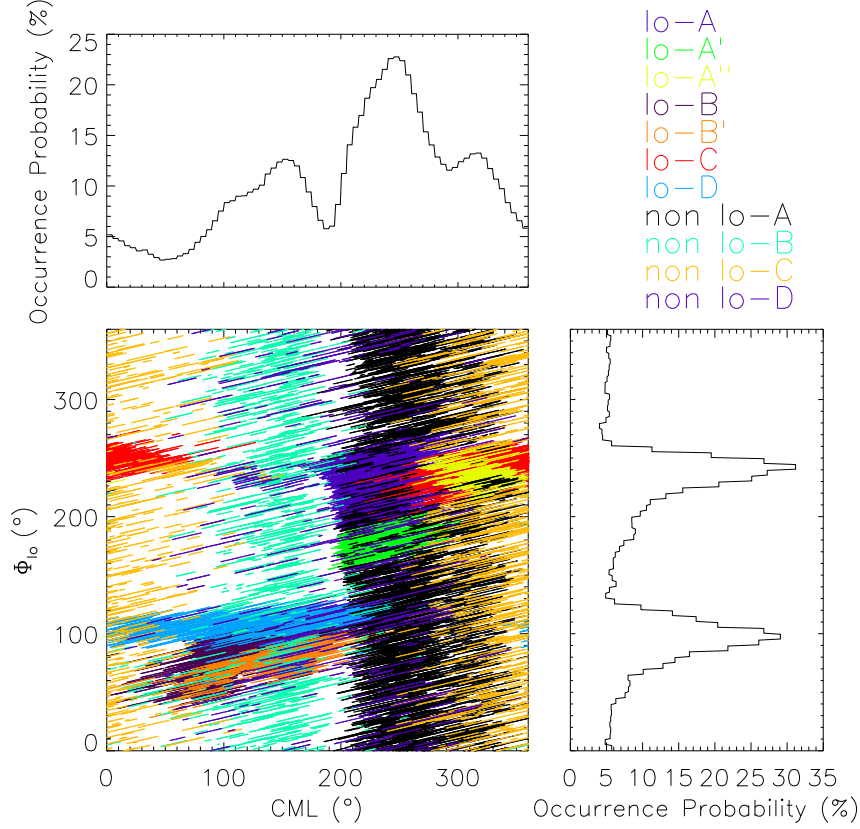
effect is related to the fast rotation of the Jupiter's magnetic field. This may be seen in the occurrence probability as a function of CML, with peaks at $\sim150°$, $\sim240°$ and $\sim320°$, corresponding to the source regions A, B and C (Io and non-Io). The second effect is caused by the Io-Jupiter interaction, it restricts most of the emissions in two specific regions of Φ_{Io}, with peaks at $\sim90°$ and $\sim240°$ corresponding to Io-B/-D and Io-A/-C emission regions, respectively. Both effects observed have been shown to be consistent with previous work (CARR et al., 1983; GENOVA et al., 1989).

In Figure 4.4, we show the emissions separated in Io-DAM and non-Io-DAM. The well-known emission regions can be clearly seen. In the case of Io emissions, the two secondary peaks around $\sim50°$ and $\sim190°$ which corresponds to new Io-emission regions, labeled Io-A" and Io-B'. For non-Io-emissions, the faint band of purple tracks between CML $\sim60°$ and $\sim300°$ reveals another new emission region, labeled non-Io-D. In addition, the large database (Figure 4.3) showed that with the adopted

Figure 4.4 - Distribution of Io (a) and non-Io (b) emissions in the CML-Φ_{Io} plane. Tracks $\longrightarrow$ possible overlap of some emissions.
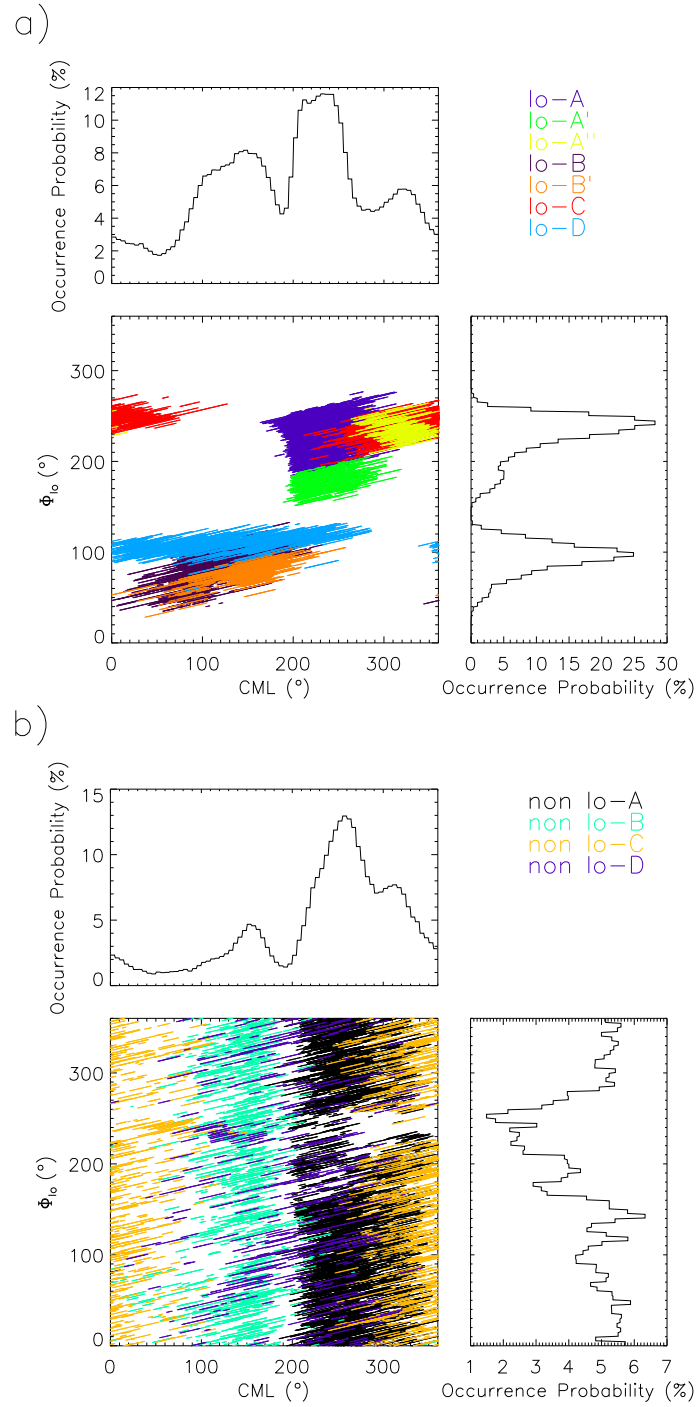
classification criteria, it was possible to distinguish the emissions between Io-DAM and non-Io-DAM even in regions dominated by Io. However the same criteria created

overlapping regions between different types of emissions and consequently changes in the CML and Φ_{Io} boundaries on emission region when they are compared with published values. These boundaries as well as the three new regions will be discussed in more details below.

4.2   Statistical anaysis

In order to check the relevance of the catalog we carried out a statistical analysis of four parameters, computed for each of the 6203 emission events of the database, which can provide important informations to the DAM emission mechanism and scenario:

- average intensity is related to the emitted power; because the galactic background is bright at decameter wavelengths, the phased beam of the NDA is large ($\sim 6° \times 10°$), and DAM is very bursty, average emission intensities are only a few dB above the background in spite of the fact that individual bursts can exceed 20-30 dB.

- overall emission duration results from the convolution of the source extent – in longitude and latitude as well as vertically along the active field lines (according to the frequency extent of the emission) – and the solid angle in which emission is beamed from every point source; emission duration is also affected by intrinsic time variations of the emission.

- maximum frequency constrains the source location, as discussed in section 2.2; it may be slightly underestimated when the signal/noise ratio is low; the minimum emission frequency may not be constrained using NDA observations due to prominent radio interference at the lowest observed frequencies, as well as the Earth's ionospheric cutoff at $\sim$10 MHz, however it may be accessed via spacecraft measurements (ZARKA et al., 2001).

- dominant circular polarization reveals the hemisphere of origin of the emission, as discussed in section 2.2; a quantitative measurement of the circular polarization ratio (Stokes parameter V, computed as explained in chapter 3) provides a finer constrain on the emission mode, mechanism and propagation; as shown below, the determination of V from Routine data is very approximate due to the low average emission intensities.

In Figure 4.5 we show the distributions of power (dB), duration (min.), maximum frequency (MHz) and circular polarization parameter (V) for All, Io and non-Io

31

Figure 4.5 - Histograms of emission power, duration, maximum frequency, and circular polarization parameter (Stokes V) for All / Io / non-Io emissions.
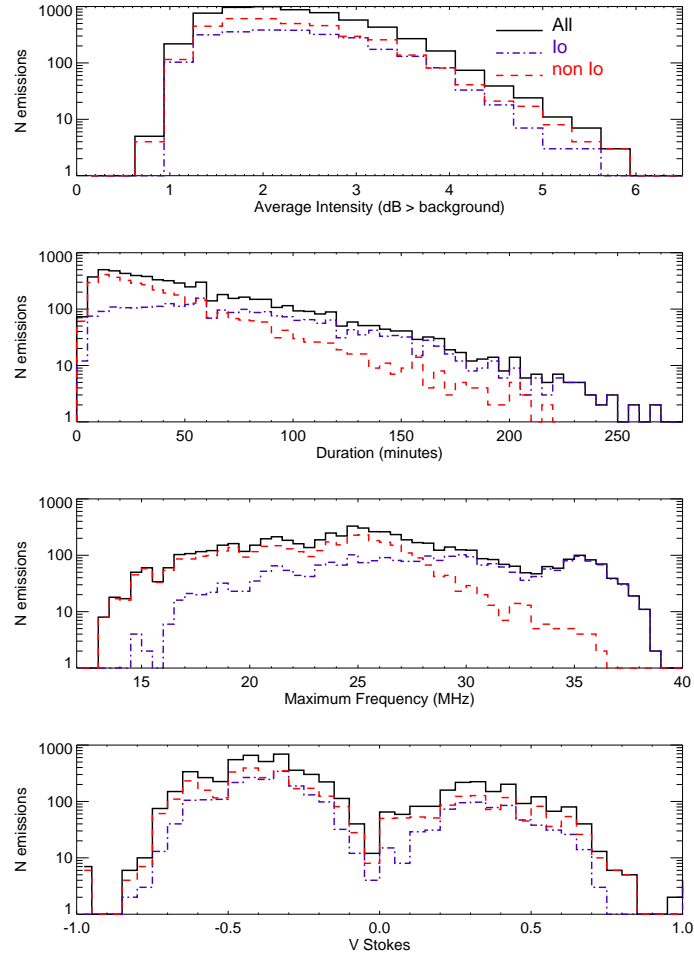
emissions (from Figures 4.3 and 4.4). Figures 4.6 and 4.7 show the same analysis. However, the distributions are further separated in Northern/Southern hemisphere sources (from the dominant circular polarization sense), and in Dawnside/Duskside sources (from the arc vertex - cf. Figure 2.11), respectively. The corresponding numerical results are summarized in Table 4.1, together with occurrence probabilities for each data selection.

During the 26 years of observations, Jovian DAM was detected 10.4% of the time. Io emissions are visible for a larger fraction of time than non-Io ones (respectively 5.9% versus 4.5%, cf. Table 4.1), which confirms earlier results (CARR et al., 1983; GENOVA et al., 1989; ZARKA, 1998; HESS et al., 2008). But the number of non-Io

Figure 4.6 - Histograms of emission power, duration, maximum frequency, and circular
           polarization parameter (Stokes V) for Io (left) and non-Io (right) in terms of
           NH and SH emission.
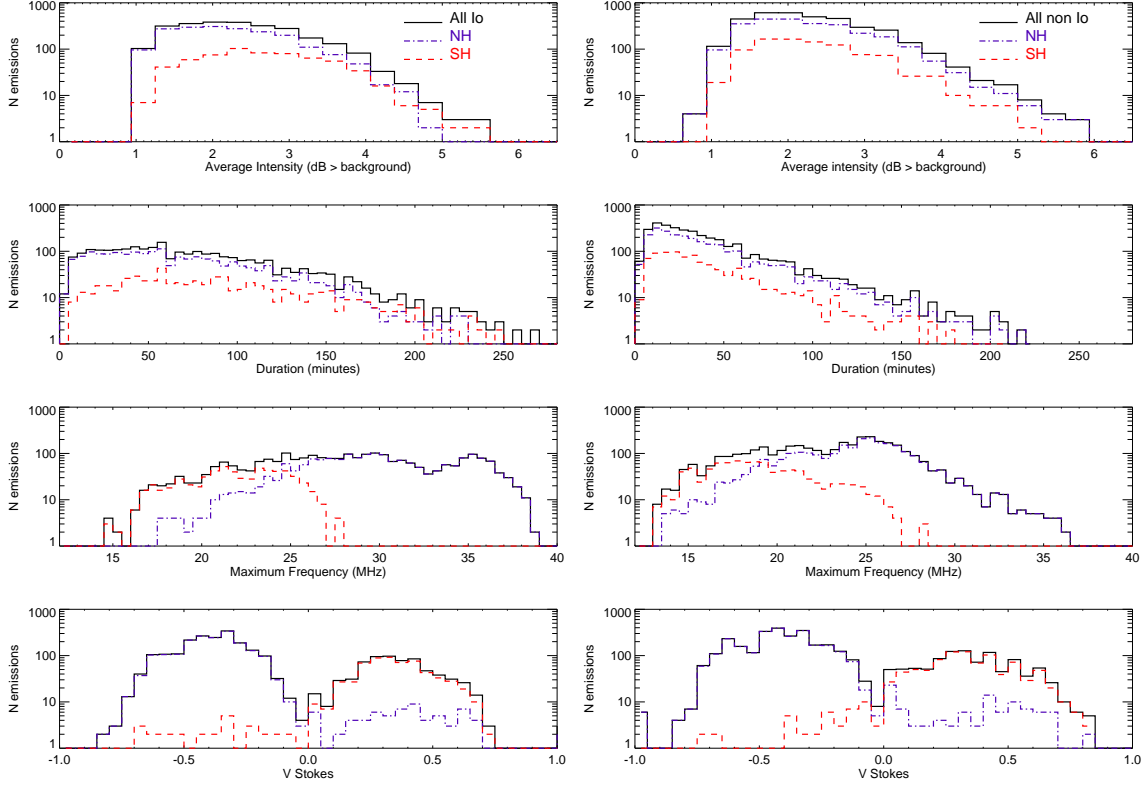
emissions is larger and consequently their duration shorter. This may be due to the
fact that Io arcs are longer than non-Io ones, likely, due to a combination of the
visibility of the source (taking into account its anisotropic beaming) and the orbital
motion of Io. The latter depends on the rotation of Jupiter, which is ~4 times faster
than Io's orbital motion. But the source of Io emissions is a restricted set of field
lines close to the Io flux tube (IFT), whereas non-Io emissions could be produced
anywhere in the auroral (or even polar) regions (cf. discussion in section 2.3). If
non-Io comes from an extended source, the visibility of the source that results from
the convolution of its extent in latitude and longitude with its beaming pattern
(ZARKA, 2004) would cause emissions with longer duration. The fact that it is not
the case suggests that non-Io emissions are related to small-scale, possibly bursty
auroral structures, seen e.g. as bright spots in the UV (PRANGÉ et al., 1998; GÉRARD
et al., 2013), rather than being the radio counterpart of the main auroral oval as a
whole. One reason for the lack of main oval radio emissions may be related to the

energy of precipitating electrons there ($\simeq$100s keV (GÉRARD et al., 2014; GUSTIN et al., 2016)), which is larger than optimal for the CMI. Conversely, the Io-Jupiter electrodynamic interaction appears more steady than the mechanism at the source of non-Io emissions.

Figure 4.7 - Histograms of emission power, duration, maximum frequency, and circular polarization parameter (Stokes V) for Io (left) and non-Io (right) in terms of the dawn and dusk emissions.
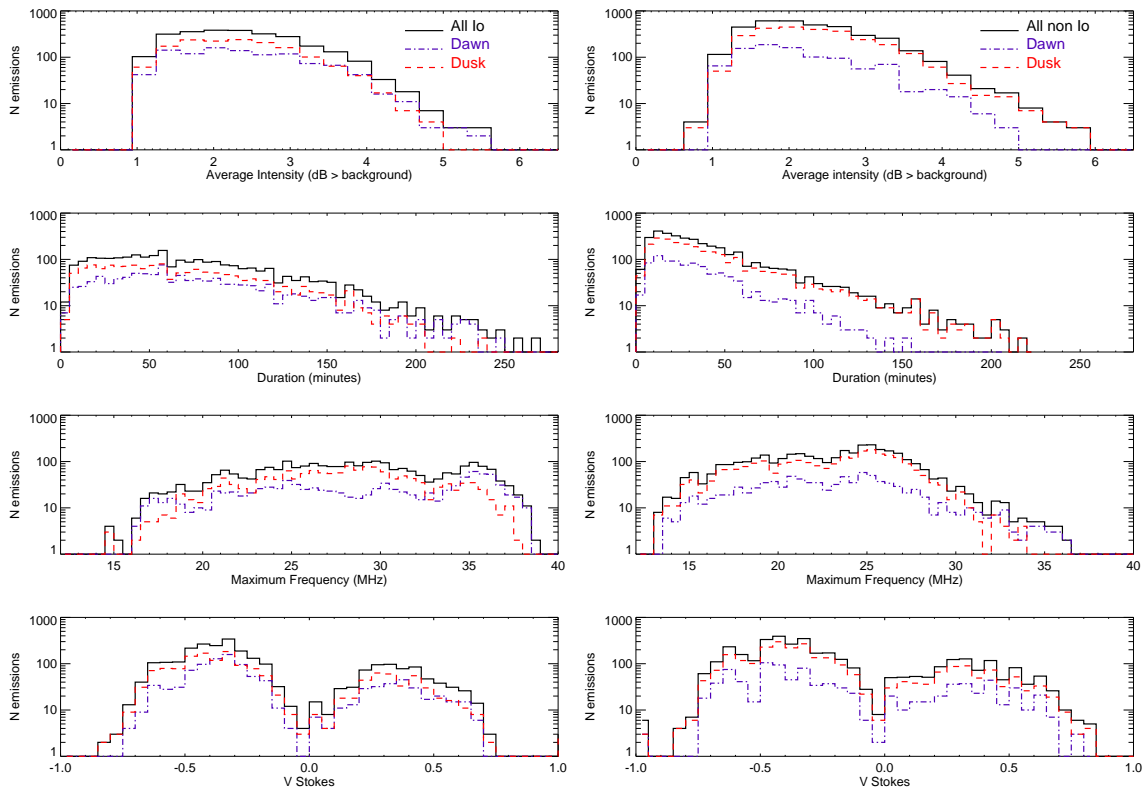
Intensities of Io and non-Io emissions are very similar. Io-emissions have a higher maximum frequency ($\sim$ 39 MHz) than non-Io-emissions ($\sim$37 MHz). Although they may occasionally reach ($\sim$ 37 MHz) the vast majority of non-Io emissions have a maximum frequency $\leq$28 MHz, as already reported by (BARROW; DESCH, 1980). Both types of emissions have very similar distributions of circular polarization ratio. V reaches marginally higher values for non-Io emissions. The most common value of $|V|$ is $\sim$0.4 to 0.5, which implies partially polarized or elliptical emission. The latter is more likely (DULK et al., 1992; DULK et al., 1994; QUEINNEC; ZARKA, 2001). We find here a more symmetrical distribution of LH and RH polarizations than discussed

in these papers, but as they addressed a limited number of cases, this question will need a more in-depth study, component by component. The same four parameters discussed above will be analyzed for each Io and non-Io component.

Table 4.1 - Statistical parameters of All, Io and non-Io emissions.

Type		Occurrence probability [%]	Power [dB] Avg.(Med.)±σ	Duration [min.] Avg.(Med.)±σ Max.	Max. frequency [MHz] Avg.(Med.)±σ Max.	Stokes V of emission event Avg.(Med.)±σ
All events		10.4	2.25(2.19)±0.79	55(42)±45 / 300.	25.1(25.0)±5.3 / 38.9	-0.20(-0.33)± 0.37
Io-	All	5.9	2.31(2.19)±0.80	74(65)±49 / 300	28.1(28.3)±5.3 / 38.9	-0.20(-0.33)±0.35
	NH	4.1	2.20(2.19)±0.76	69(59)±46 / 300	30.2(29.9)±4.2 / 38.9	-0.36(-0.38)±0.20
	SH	1.8	2.64(2.56)±0.84	90(81)±54 / 282	21.9(22.0)±2.8 / 29.4	0.31(0.33)±0.20
	Dawn	2.6	2.33(2.19)±0.85	80(68)±52 / 300	28.9(29.4)±6.1 / 38.9	-0.18(-0.32)±0.35
	Dusk	3.3	2.29(2.19)±0.77	70(61)±47 / 282	27.6(27.9)±4.6 / 38.6	-0.21(-0.33)±0.36
non-Io-	All	4.5	2.22(2.19)±0.77	41(31)±35 / 222	23.0(23.5)±4.1 / 37.4	-0.21(-0.33)±0.38
	NH	3.3	2.21(2.19)±0.78	41(30)±35 / 222	24.3(24.7)±3.6 / 37.4	-0.39(-0.42)±0.21
	SH	1.2	2.26(2.19)±0.74	42(32)±34 / 208	19.1(18.8)±3.0 / 28.5	0.32(0.33)±0.21
	Dawn	1.1	2.07(1.87)±0.78	36(30)±29 / 208	23.1(23.1)±4.5 / 37.4	-0.18(-0.33)±0.40
	Dusk	3.4	2.27(2.19)±0.76	43(31)±36 / 222	22.9(23.6)±3.9 / 35.9	-0.22(-0.33)±0.36

Figure 4.6 shows the same distributions, separately for Io and non-Io emissions. Further, we split emissions by hemisphere of origin (according to the emission type, A & B from the northern hemisphere (NH) and C & D from the southern hemisphere (SH)). I can be seen that Northern emissions are more frequent than southern ones. This higher northern "activity" might be due to stronger Pedersen currents and magnetic field amplitude in the northern hemisphere (NICHOLS et al., 2009, e.g.), and/or to the fact that stronger magnetic field amplitude in the northern hemisphere results in more keV electrons reflected back by mirror effect, generating more CMI radio emission (ZARKA et al., 1996). The latter suggestion is supported by the fact that the UV spot at the southern end of the IFT (or rather of the active flux tube close to the IFT) is stronger than the northern one (BONFOND et al., 2013), thus there are more precipitated and less reflected electrons in the South. However, southern emissions surprisingly appear to reach higher intensities than northern ones.

For the main oval, the UV brightness is rather higher in the North (CLARKE et al., 2009) but, as discussed above, non-Io-emissions may be related only to hot spots, along the main oval or at higher latitude (cf. discussion in section 2.3). A puzzling feature of Figure 4.6 is that while northern non-Io emissions are more frequent than southern ones for all intensities and durations, northern Io emissions are more frequent than southern ones mainly for low intensity and low duration values.

Maximum frequencies reach, for non-Io-emissions, $\sim$37 MHz in the North, $\sim$28.5 MHz in the South. For Io emissions reach $\sim$39 MHz in the North and $\sim$28 MHz in the South. These high frequency limits provide strong constraints on source locations and magnetic field models (GENOVA; AUBIER, 1985; HESS et al., 2011). The polarization is consistent with X-mode emission: mainly RH from the North, and LH from the South (cf. discussion in section 2.2). Polarization with an opposite sign is observed in $\sim$1% of the cases, which we attribute to instrumental errors (cf. chapter 3) rather than detection of O-mode (that is expected to be much weaker than X-mode (WU, 1985)).

Figure 4.7 displays histograms for Io and non-Io emissions, separated by local time of origin (according to the emission type, B & D from the dawn side of the planet and A & C from the dusk side). For Io-DAM no significant difference between the dusk and dawn sides is observed. But for non-Io-DAM, dusk emissions dominate in number, intensity and duration. The higher dusk "activity" might be due to emissions triggered by fast forward interplanetary shocks (FFS), as demonstrated by Hess et al. (2012) and Hess et al. (2014). These authors showed that FFS-triggered DAM

emissions onset in the afternoon sector. These results suggested that the relatively empty "cushion" on the dawn side of Jupiter's magnetosphere absorbs FFS-triggered compressions, whereas dusk emissions were favored by compressions of the thick current sheet on that side of the planet (KIVELSON; SOUTHWOOD, 2005), possibly heating the plasma via viscous interaction or adiabatic compression.

We note in Figure 4.7 that the highest observed maximum frequencies of DAM emissions are slightly higher on the dawn side that on the dusk side. Distributions of V are similar for Io and non-Io emissions, and for dawn and dusk sources.

The properties deduced from histograms are statistical and global. Their detailed analysis, in the context of our present knowledge of radio and UV emissions from Jupiter's aurora and Jupiter-Io interaction, must take into account the temporal variations of the parameters studied, that may depend on the solar wind fluctuations, seasonal variations of the ionospheric conductivity, Io's volcanic outbursts, and the way all these fluctuations affect the solar wind/magnetosphere/ionosphere/satellite couplings and consequently the magnetospheric activity. The study of these time variations is made possible using our catalog, and it will be discussed later.

4.3   Distributions versus CML and Io longitude

Another way of considering the variations of the four above parameters characterizing DAM emissions is to plot them as a function of the periodic coordinates that may affect emission generation and visibility.

In the case of Io emissions, this coordinate is the Jovicentric longitude of Io (Λ_{Io} where Λ_{Io} = CML - Φ_{Io} + 180°), i.e. the position of the satellite in the rotating Jovian magnetic field, that modulates the Alfvénic current intensity and topology (SAUR et al., 2004, e.g.) and the maximum frequency at the foot of the active field line. The corresponding plots are displayed in Figure 4.8. From Figure 4.8, it can be seen that Io emissions are mainly detected for 90° $\leq \Lambda_{Io} \leq$ 340° and that the distribution of maximum frequency is well structured versus Λ_{Io}. This structure is discussed in more details below.

In the case of non-Io-emissions, the periodic coordinate is the CML, which is related to the longitude of dawn or dusk sources via their beaming angle. The corresponding plots are displayed in Figure 4.9. We recognize easily the emission regions from Figure 4.4 (especially A, B, and C) as separate blobs of points, and the quasi-absence of emissions for 180° $\leq$ CML $\leq$ 200°. Non-Io-A emissions have the highest intensity

Figure 4.8 - Io-emissions' power, duration, maximum frequency, and polarization ratio as a function of Λ_{Io}.
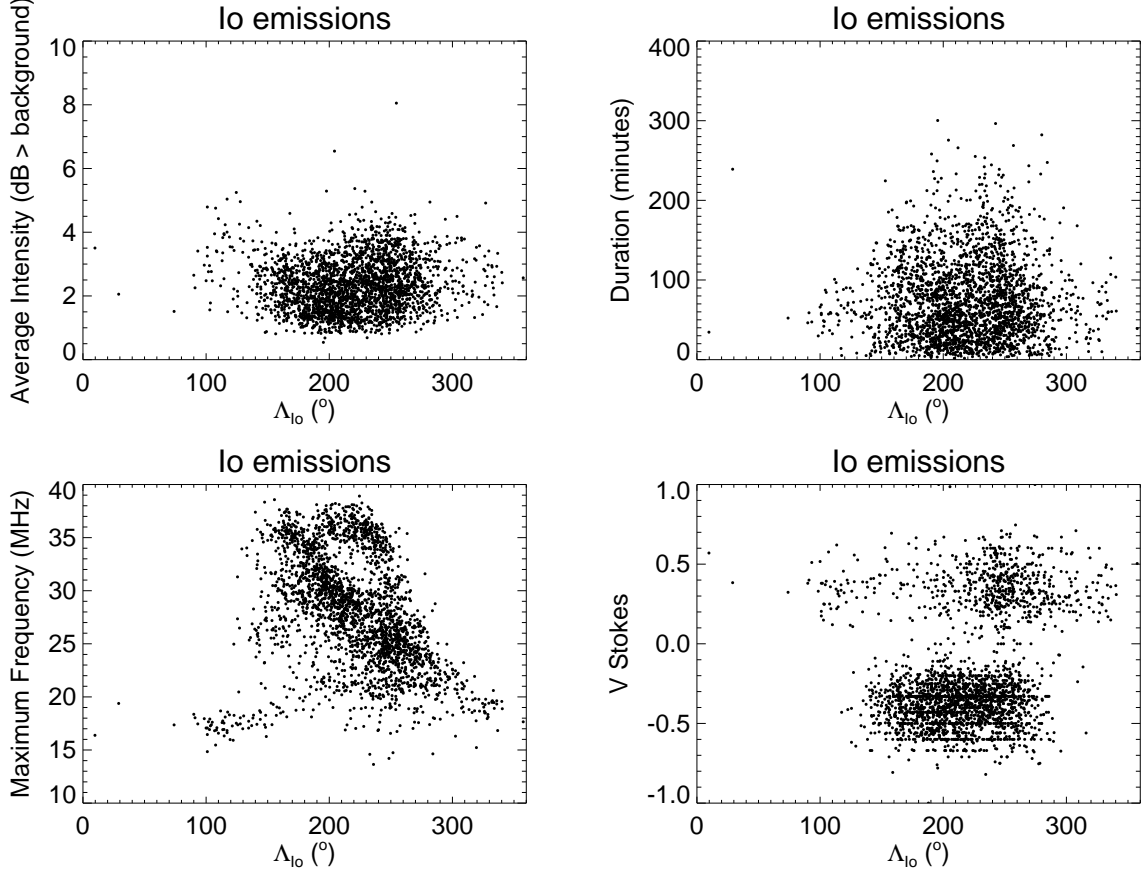
and longest duration (albeit with a large scattering), followed by non-Io-B and non-Io-C components. A and B emissions, well identified as the RH ($V < 0$) blobs on the bottom right panel in restricted CML ranges, reach maximum frequencies above 30 MHz in similarly restricted CML ranges (respectively $\sim 220° - 300°$ and $\sim 80° - 180°$). This can be interpreted as the passage of a single source region respectively near the duskside and near the dawnside limbs. Elementary 2D geometry points at a source at the midpoint of the above CML ranges, i.e. $\sim 195°$, located on the negative gradient (downwards slope) of the strong magnetic field anomaly in Jupiter's northern hemisphere relative to the rotation of the planet (HESS et al., 2011). Along such a negative gradient, part of the electron population mirroring on the magnetic anomaly now precipitates deeper, being eventually lost by collisions and generating a loss-cone distribution than can drive radio wave generation by the

Figure 4.9 - non-Io-emissions' power, duration, maximum frequency, and polarization ratio
as a function of CML.
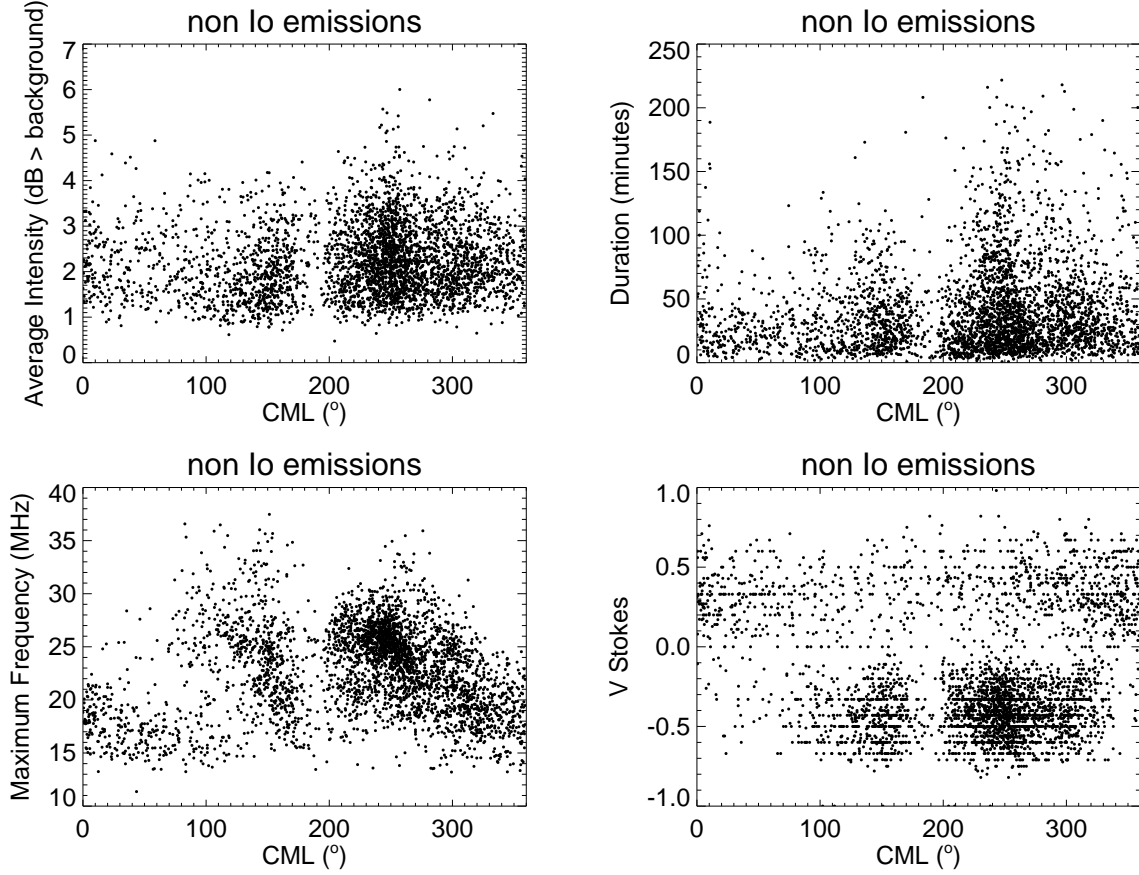
CMI. With a source at $\sim 195°$, the center of each CML range above implies an emission at $\sim 65°$ from the magnetic field, consistent with the CMI widely open hollow cone beams. Of course the problem must be studied in 3D geometry, and the non-Io sources are extended or rather spread over a broad longitude range, so that the above values are only indicative. In the southern hemisphere, LH ($V > 0$) non-Io emissions are more uniformly spread at all CML, and their maximum frequency is lower. This is consistent with the weaker and more even magnetic field in Jupiter's southern hemisphere, without any magnetic anomaly comparable to the northern one.

Note that for Io and non-Io emissions, scatter plots of any of the above 4 parameters against any each other do not show any significant correlation, suggesting that

the histograms of Figures 4.5 to 4.7 and the scatter plots in Figures 4.8 and 4.9 summarize well the statistical properties of these emissions.

Figure 4.10 - Maximum frequency versus Λ_{Io} for Io and non-Io emissions.
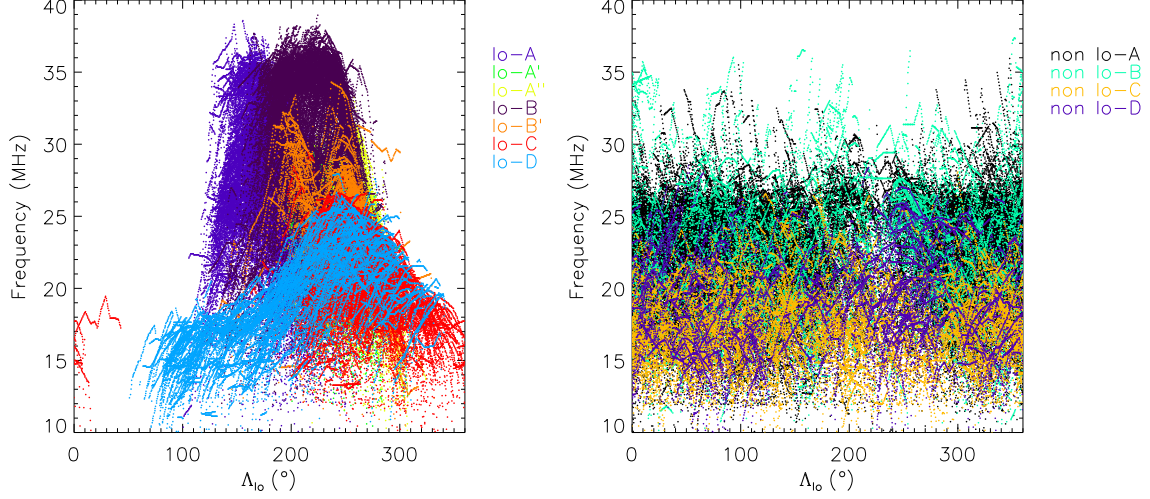
Each emission component is color coded as in Figures 4.3 and 4.4.

Figure 4.10 focusses on the distribution of maximum frequencies of Io and non-Io emissions, similar to the bottom left panels of Figures 4.8 and 4.9, but with two major differences: each emission component is color coded as in Figures 4.3 and 4.4, and instead of a single point per emission event, the complete variation of the maximum frequency during each emission is plotted, at the time resolution of 1 minute. The plots are thus more densely populated and accurate. Figure 4.11 shows the same result as in Figure 4.10, but, it was divided in components for better understanding. Figures 4.10(left) and 4.11(Io-A/A'/A", Io-B/B', Io-C and Io-D) display the Io emissions versus the Λ_{Io}, showing that Io-A and Io-B emissions reach the highest frequencies (up to 39 MHz) and demonstrating clearly the distinct natures of Io-A' and Io-C emissions as well as Io-B and Io-B' emissions. Figures 4.10(right) and 4.11(non Io-A, non Io-B, non Io-C and non Io-D) display the non-Io emissions versus the Λ_{Io}, highlighting Figure 4.11(non Io-D) which shows the non-Io-D component. From these figures it can be seen that Io-emissions cluster in a limited range of Io's longitude ($\sim 120° - 300°$ for northern sources (Io-A/A'/A" and Io-B/B') and $\sim 70° - 360°$ for southern ones (Io-C and Io-D)), with an envelope that draws an overall high-frequency limits as a function of Λ_{Io}.

Figure 4.11 - Maximum frequency versus Λ_{Io} for Io and non-Io components.
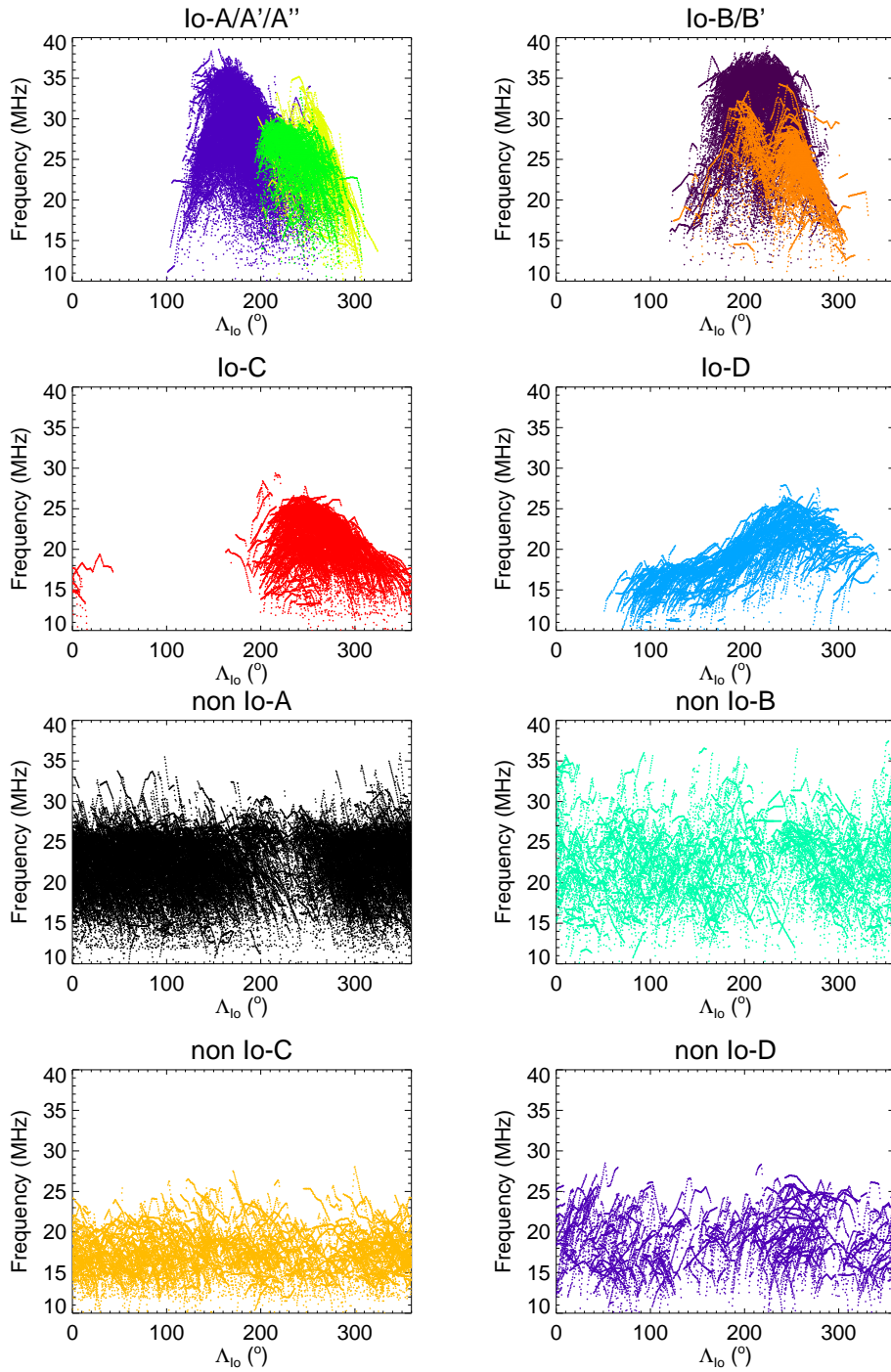
Each emission component is color coded as in Figures 4.3 and 4.4.

This envelope is a strong constraint on the magnetic field model and lead angle of the active field line close to the IFT (GENOVA; AUBIER, 1985; ZARKA et al., 2002; HESS et al., 2011). It also shows the distinctive character of the various Io-DAM

components, that can have distinct maximum frequency envelopes at the same Λ_{Io}. Full understanding of each component characteristics will deserve a specific study. Finally, non-Io-emissions versus Λ_{Io} show, as expected, no modulation in Λ_{Io}, except the lack of points around 230° that corresponds to the gap at the Io-A/C phase on Figure 4.4b. It also illustrates differently the statistical distribution in Figure 4.6 of RH (Northern) and LH (Southern) maximum frequencies of ~36 MHz and ~27 MHz, respectively.

4.4 Description of source regions

In order to investigate each type of emission we display in Figure 4.12 examples of dynamic spectra of all DAM components of Io and non-Io emissions in their dominant polarizations. In Figure 4.13, we show statistical analysis of the same emission parameters as in Figures 4.5, 4.6 and 4.7, but separated by component. Table 4.2 lists statistical values, as in Table 4.1, by components.

Figure 4.12 - Examples of dynamic spectra of Io and non-Io arc shapes components in its dominant polarizations.
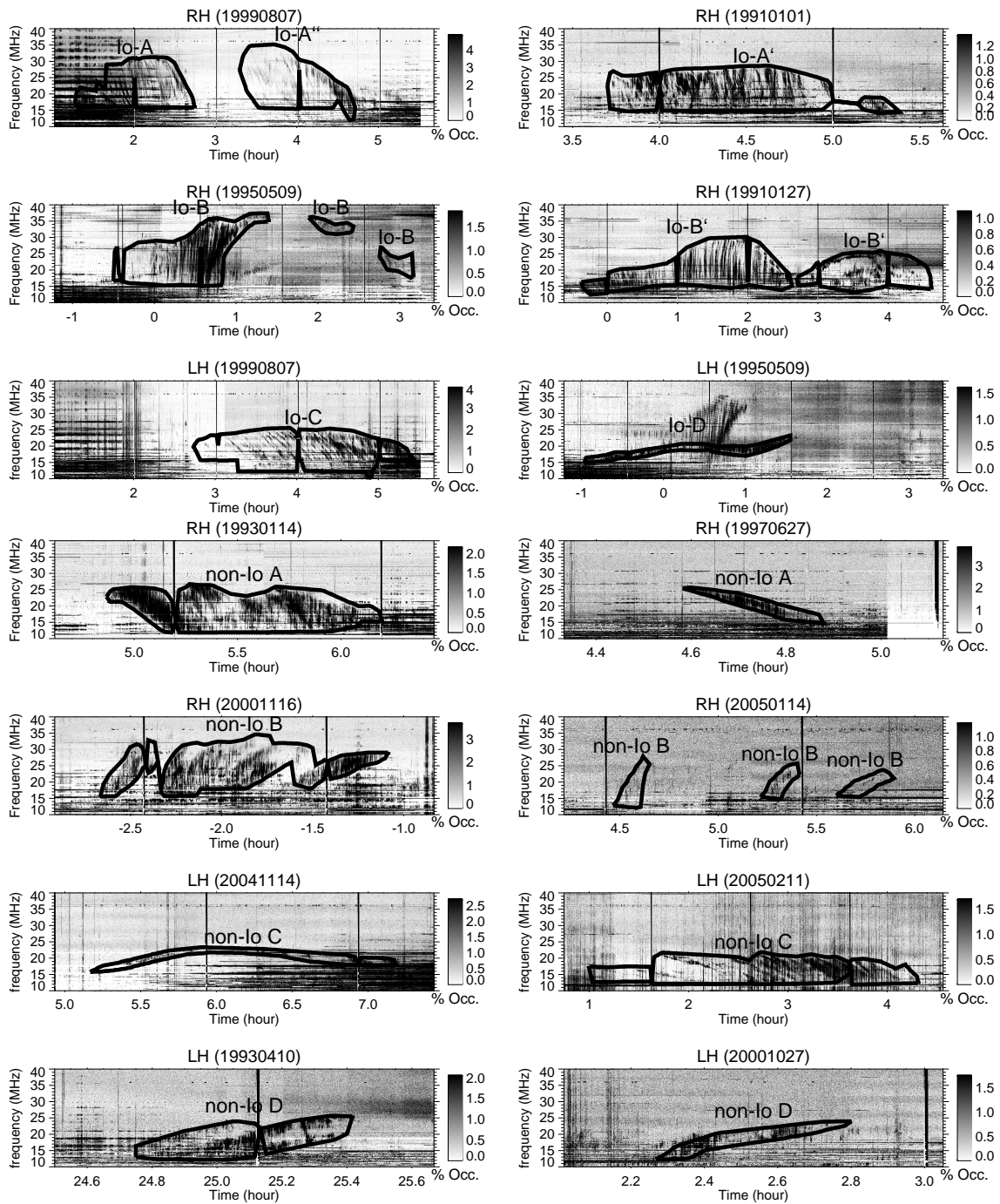
Table 4.2 - Summary of the characteristics for all sources

Type		CML (°)	Φ_{Io} (°)	Occ. prob. [%]	Power [dB] Avg.(Med.)±σ	Duration [min.] Avg.(Med.)±σ Max.	Max. Frequency [MHz] Avg.(Med.)±σ Max.	Stokes V of emission Avg.(Med.)±σ
Io-	A	180-310	180-280	1.67	2.14(2.14)±0.67	71(66)±43 224	30.5(30.4)±3.6 38.6	-0.37(-0.40)±0.22
	A'	190-300	150-200	0.36	2.07(1.87)±0.73	48(40)±36 180	26.8(27.2)±2.3 33.4	-0.39(-0.43)±0.20
	A"	270-360	210-270	0.24	2.25(2.19)±0.70	52(51)±27 136	27.7(27.8)±3.2 35.2	-0.35(-0.38)±0.21
	B	0-230	40-120	1.44	2.26(2.19)±0.86	77(65)±53 300	32.9(34.3)±3.8 38.9	-0.35(-0.36)±0.18
	B'	0-260	40-110	0.40	2.40(2.34)±0.79	75(64)±49 258	26.0(25.9)±3.2 34.3	-0.36(-0.38)±0.17
	C	240-100	210-270	1.04	2.76(2.71)±0.83	92(81)±56 282	22.2(22.3)±2.6 29.4	0.30(0.32)±0.20
	D	350-285	80-130	0.72	2.47(2.39)±0.83	88(81)±51 249	21.5(21.6)±2.9 27.9	0.34(0.36)±0.19
non-Io-	A	190-360	0-360	2.66	2.29(2.19)±0.77	43(32)±37 222	24.3(24.8)±3.2 35.9	-0.38(-0.41)±0.22
	B	0-220	0-360	0.67	1.94(1.87)±0.75	33(27)±25 173	24.3(24.5)±4.4 37.4	-0.41(-0.43)±0.20
	C	240-140	0-360	0.80	2.22(2.19)±0.73	41(30)±34 200	18.6(18.3)±2.7 28.1	0.30(0.33)±0.21
	D	10-330	0-360	0.39	2.35(2.19)±0.78	45(35)±34 208	20.3(20.3)±3.4 28.5	0.35(0.38)±0.19

Figure 4.13 - Histograms of emission power, duration, maximum frequency, and polarization ratio, per emission component.
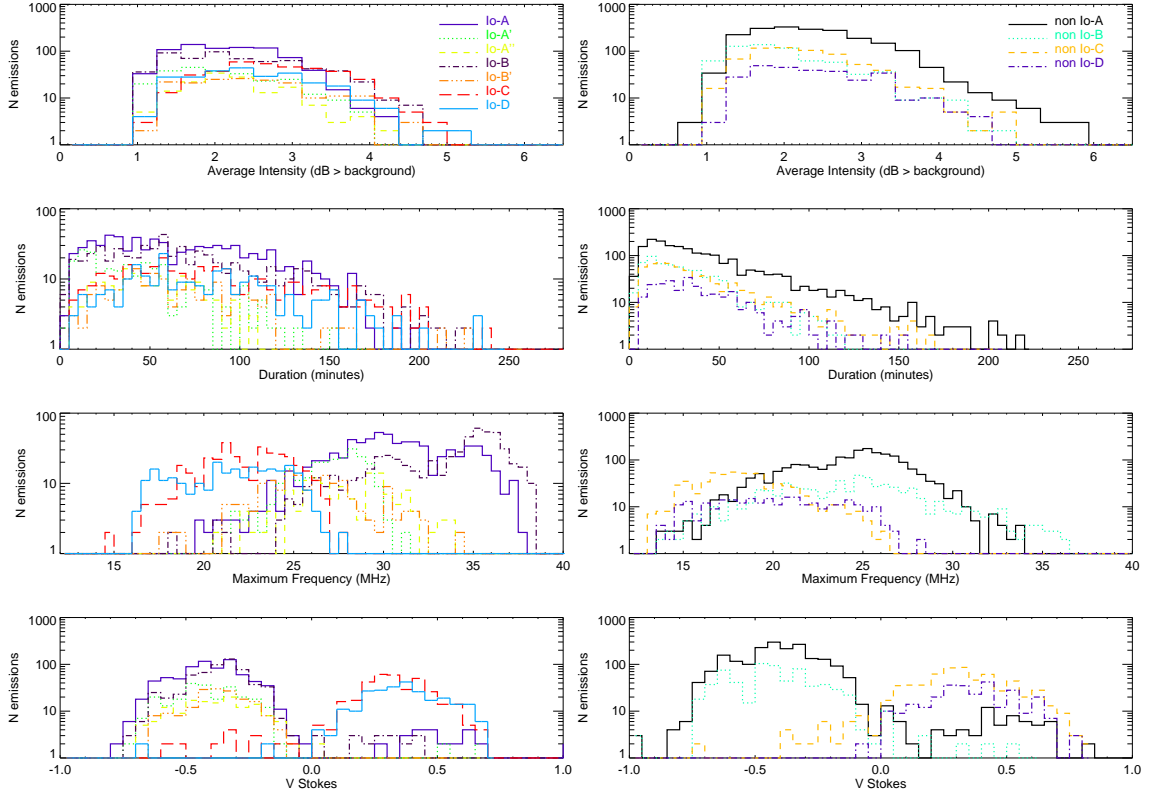
Io-A emission characteristics derived here are consistent with previously published ones (CARR et al., 1983; GENOVA et al., 1989; QUEINNEC; ZARKA, 1998; HESS et al., 2008). It is mainly observed within CML=180°-310° and Φ_{Io}=180°-280°, and is composed of multiple vertex late arc structures with RH dominant polarization, average duration of 71 min, and maximum frequency of 38.6 MHz. Io-A' emission is composed of vertex late arcs (also RH) with very weak curvature (CARR et al., 1983), and covers the range CML=190°-300° and Φ_{Io}=150°-200°. It exhibits a maximum frequency of 33.4 MHz, higher than the value given in Carr et al. (1983). Our classification criteria allowed us to identify a new emission region with unique spectral characteristics. The emission often exhibits only one vertex late arc with RH dominant polarization, maximum frequency up to 35.2 MHz and an average duration of 50 minutes. We observed it within CML=270°-360° and Φ_{Io}=210°-270°, overlapping with Io-C. It was previously described as "Io-C RH" by Boudjada et al. (1995), who suggested that this component comes from the same source in the same hemisphere

as Io-C. But this suggestion is incompatible with the now well established theoretical modeling by Hess et al. (2008), so we concluded that it is an emission coming from the northern hemisphere and we called this newly identified component Io-A". We show a representative example in Figure 4.12.

Figure 4.14 - Occurrence probability of Io emissions versus CML-Φ_{Io} per component.
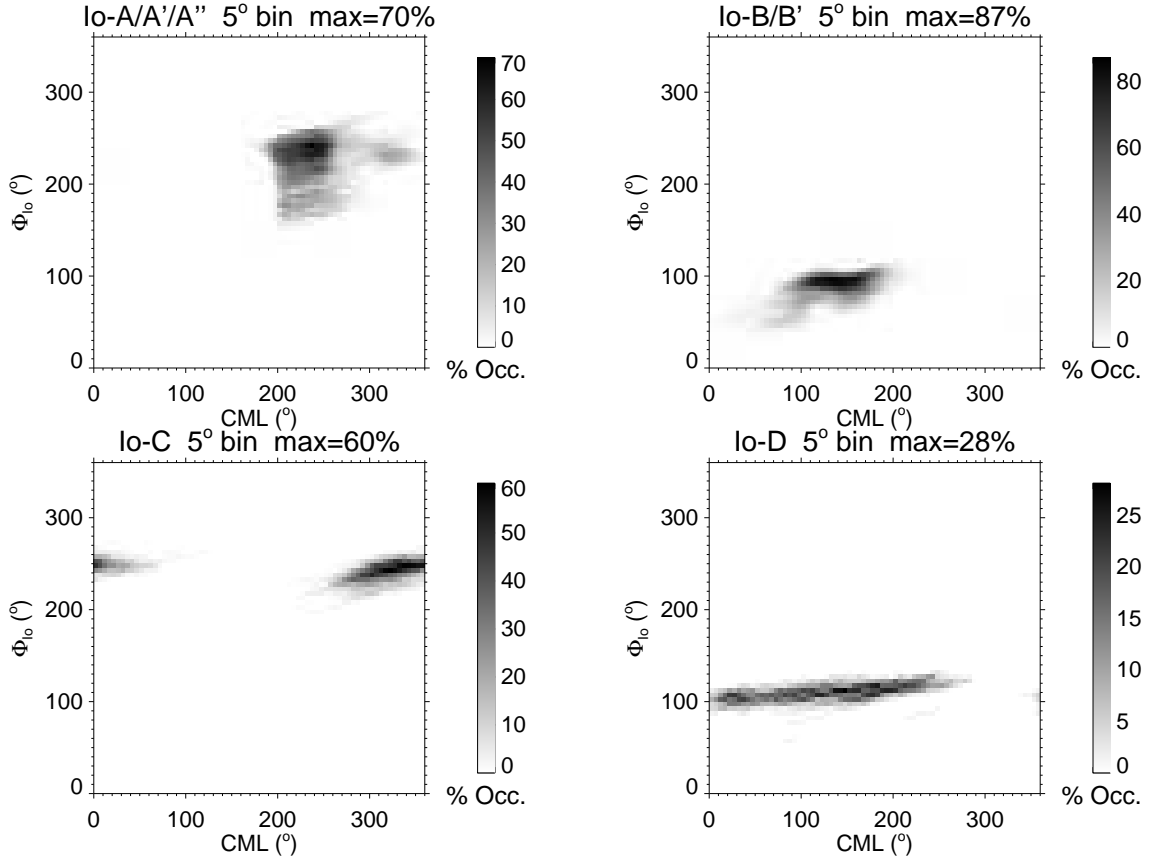
Io-B emission displays two types of morphology. The classical Io-B great arc with precursor fringes and a long $t - f$ tail has been described by Carr et al. (1983) and studied in details by Queinnec and Zarka (1998). It is RH polarized and we find here an average duration of 77 min. for its main part (see Figure 4.12 and Table 4.2). Figures 4.4 and 4.5 show that the Io-B emission regions start at lower CML that previously thought. It reaches a maximum frequency ∼38.9 MHz, slightly below that derived from Voyager observations (CARR et al., 1983), but this may be due to the lower sensitivity of NDA compared to Voyager at Jupiter. Below the Io-B

47

Figure 4.15 - Contours of the Io-emission regions computed from 10%, 25% and 50% occurrence levels with bins 5° and all frequencies included.
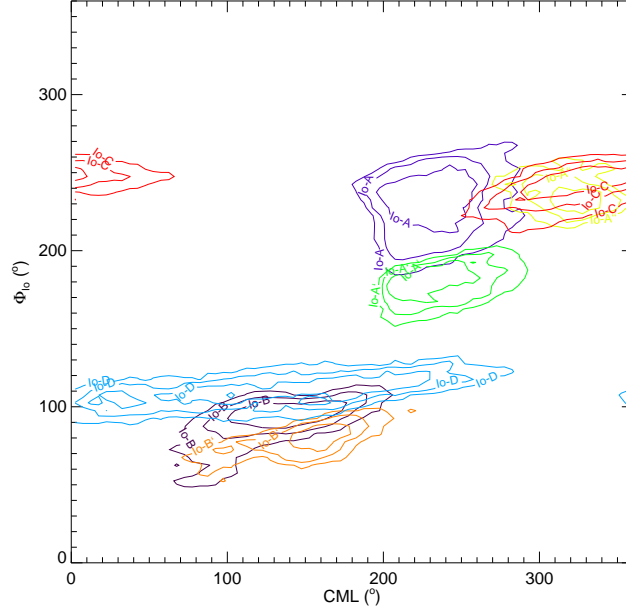
emission region (i.e. at lower values of Φ_{Io}) we have noticed a series of narrowband emissions with $t - f$ characteristics different from Io-B, that we have labeled Io-B'. This emission generally consists of two consecutive groups of vertex early arcs separated by a gap without emission, such as the example shown in Figure 4.12. Both groups have similar envelopes with a maximum frequency up to 34.3 MHz and dominant RH polarization. Leblanc (1981) and Clarke et al. (2014) discussed similar cases which they observed in the same CML-Φ_{Io} region.

We have noted in Figures 4.4 and 4.5 that the Io-C emission starts before the CML=280° mentioned in Carr et al. (1983). This has also been seen by Clarke et al. (2014) in their analysis of a single Io-C event. However, as discussed below in Figures 4.14 and 4.15, the extension of the Io-C region to CML < 270° (down to CML~240°) corresponds to occurrence probabilities <10%. The Io-C emission is predominantly LH polarized, made of vertex late arcs, of highest average intensity of all Io emissions (cf. Table 4.2). Average duration is 1.5 hour and maximum frequency reaches 29.4 MHz. This is much lower than the 36 MHz noted by Carr et al. (1983), and is due to the fact that we have distinguished and removed the new RH component A", now clearly distinct of Io-C.

Figure 4.16 - Occurrence probability of non-Io emissions versus CML-Φ_{Io} per component.
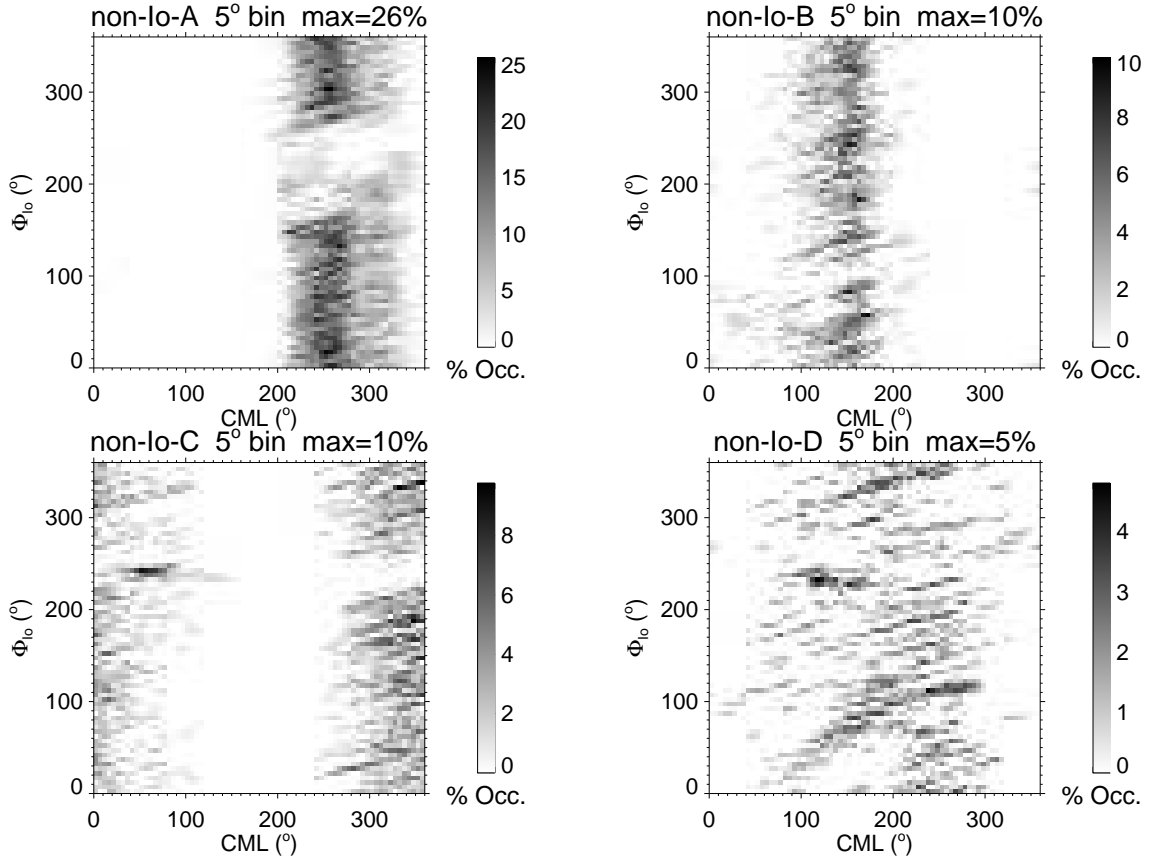
The Io-D emission is composed of a single vertex early arc with a maximum frequency up to 27.9 MHz (Figure 4.12). This maximum frequency is much higher than the 18 MHz described in Carr et al. (1983), and corroborates statistically the example shown in Queinnec and Zarka (1998) and modelled in Hess et al. (2008). Io-D emission is predominantly LH polarized and may last up to 1.5 hour too. It has been detected beyond CML $\sim$200°, and its new boundaries are shown in Figures 4.14 and 4.15. The values in Table 4.2 confirm the histogram of Figure 4.6, i.e. that southern Io emissions reach higher intensities than northern ones.

Non-Io emissions have envelopes less extensive than Io ones, i.e. few emissions exceed $\sim$28 MHz (they may reach $\sim$ 37 MHz in the northern hemisphere, cf. Table 4.2 and Figures 4.10b and 4.13). But the arc shapes are repeatable and recognizable. This allowed us to separate to a large extent Io and non-Io emissions overlapping in the

CML-Φ_{Io} plane (Figure 4.4). With our new database, the CML boundaries of non-Io emissions have been modified when compared to previous studies (CARR et al., 1983; GENOVA et al., 1989). For example, non-Io-C starts at CML=255° (and even down to $\sim 240°$ at very low occurrence level) and ends at CML=95° (up to $\sim 140°$ at very low occurrence level). The maximum frequency of non-Io-C (28 MHz) is also lower than previously thought for the same reason as Io-C (distinction and removal of embedded Io-A" emissions).

Non-Io-A emissions have maximum frequencies of 35.9 MHz, quite consistent with the literature. Non-Io-A events are by far more numerous. They include a "zoo" of various arc types (Figure 4.12), possibly from different elementary sources, that may include emissions induced by satellites other than Io, not identified until now. Non-Io-B have the highest maximum frequency (37.4 MHz), also consistent with the literature, and the strongest circular polarization (cf. Table 4.2 and (QUEINNEC; ZARKA, 2001)).

We have identified around 289 events ($\sim 0.4\%$ occurrence) with LH polarization, vertex early arcs and maximum frequency about 28.5 MHz, distributed over a very broad range of CML (10° - 340°) for all Φ_{Io} (see limits in Table 4.2). This new component has all the required characteristics for being identified as the non-Io-D emission. It is actually mentioned in the review by Bose et al. (2008) (within the CML range $\sim 0 - 200°$) but without any supporting observation. Being much less frequent than the other non-Io components and diluted over a broad range of CML overlapping with other non-Io components, the large statistical basis of the catalog, discussed here, was necessary to clearly establishes its existence and characteristics.

Figure 4.14 shows the occurrence probability as a function of CML and Io phase for each Io emission component. It is obtained by dividing the number of minutes of emissions of a given type, in bins of 5° × 5° in the CML−Φ_{Io} plane, by the number of minutes of observations per bin of Figure 4.2. Io emissions are grouped by hemisphere and limb, and maximum probability (in %) is indicated at the top of each plot. Northern hemisphere emissions reach very high occurrence probabilities in restricted areas. Figure 4.15 shows the overall limits in CML and Φ_{Io} of the region, for each component, corresponding to an occurrence probability $\geq 10\%$, 25% and 50% (where occurrence reaches high enough values), for Io-emission.

Figure 4.16 provides similar informations for non-Io components. As their occurrence probability is generally weaker, Table 4.2 lists the minimum and maximum CML value of each non-Io region (without any dependence in Φ_{Io} of course) determined

from its integrated occurrence versus the CML.

4.5 Summary & Conclusion

We have carried out a statistical analysis of the database, developed in this work, focussing on occurrence rates, intensity, duration, maximum frequency and polarization of the events. This study suggests a number of results listed below, the confirmation of which will motivate specific in-depth analyses:

- non-Io-DAM appears to be related to small-scale, possibly bursty auroral structures;

- northern emission are more frequent but southern ones are more intense;

- in the case of Io emissions, the excess of northern emissions specifically concerns low intensity and low duration emissions;

- in the case of non-Io emissions, dusk emissions dominate dawn ones by occurrence, intensity and duration;

- the distribution of non-Io emissions versus the CML suggests that radiosources are preferably located above auroral regions where $d|B|/dCML{<}0$;

- the distribution of the maximum frequency of Io emissions is densely clustered versus Io's longitude Λ_{Io}; its $t - f$ envelope imposes a strong constraint on the Io-Jupiter interaction mechanism (lead angle), provided that the Jovian internal - and surface - magnetic field is well known.

The results obtained for each emission type are generally in good agreement with previous works, but a few new results can be highlighted:

- two new Io-induced radio emission types were discovered or identified: Io-A" and Io-B', that have spectral characteristics distinct of other emission types;

- the CML$-\Phi_{Io}$ contours and maximum frequency of known emission types, especially Io-C and Io-D, are redefined (differently from the values in the literature); Io-C is detected at lower CML, has a maximum frequency $\sim$29 MHz and exclusively LH polarization; Io-D is observed beyond published

51

limits and has a maximum frequency higher than described in previous works;

- the non-Io-D type was discovered in a broad CML range (and all Io phases), with LH polarization, maximum frequency ∼28 MHz, and low occurrence probability.

These new results are due to the exceptional length of the database, the digital data format, the new classification method adopted (with a set of consistent, minimum, necessary and sufficient criteria), and the care and accuracy in its application. This catalog will be the basis for the next chapter and future works.

5 THE LONG-TERM VARIABILITIES ON DAM EMISSIONS

In this chapter, we show a preliminary analysis of the long-term variabilities of the DAM emission and how they can affect the occurrence probability in CML-Φ_{Io} plane.

5.1 Distribution of DAM occurrence probability in the time

In order to analyse the variabilities for catalogued emissions, shown in Figures 4.3 and 4.4 and discussed in chapter 4, we organized the catalog as two time series of occurrence probability per observation, shown in Figure 5.1, as following: Io-emissions (Figure 5.1 tob panel) and non-Io-emissions (Figure 5.1 bottom panel). The occurrence probability per observation was calculated by the ratio between the duration of emission and the duration of observation and it was distributed in the mid-point of each observing or activity time.

As discussed in section 4.2 and seen in Figure 5.1, Io emissions are visible for a larger fraction of time than non-Io ones, which explains the higher values of occurrence probability per emission than non-Io. However the number of non-Io emissions is larger and consequently their duration shorter. We also observe a horizontal line with values of occurrence probability equal to zero that correspond to 89.6% of the observation time which emissions were not detected. Without any spectral analysis, it can be noted clearly two strong long-term periods in the DAM emission, one with $\sim$400 days and another with $\sim$12 years. The first one is known as Jupiter's synodic period, which is caused by the conjunction of Jupiter with the Sun-Earth line, and the second is believed to be a contribution of two effects with periods that are very close, the declination of the Earth with respect to the Jovigraphic equatorial plane (D_E) with $\sim$11.8 years and the solar activity with $\sim$11 years. Although not visible in time series, the DAM emission exhibits strong short-term periodicities related to the rotation of the Jupiter's magnetosphere (9.9249 h, System III), Io orbital period (42.46 h), already discussed in chapter 4, as well as the beat period between System III and Io orbital period, 12.95 h (BIGG, 1966; CARR et al., 1983; KAISER, 1993; QUEINNEC; ZARKA, 1998). The background observation also introduces two strong short-term periodicities in the series, the first one comes from the size of observation windows $\sim$8 h (seen Figure 4.1 in section 4.1) and another is caused by the interval between observations ($\sim$1 day). Although we have highlighted here the short-term variabilities, the focus of this chapter is the study of long-term variability and how they can affect the occurrence probability in CML and Φ_{Io}.

Figure 5.1 - Distribution of the occurrence probability for emissions at observation day. Io-emissions (top panel) and non-Io-emissions (bottom panel).
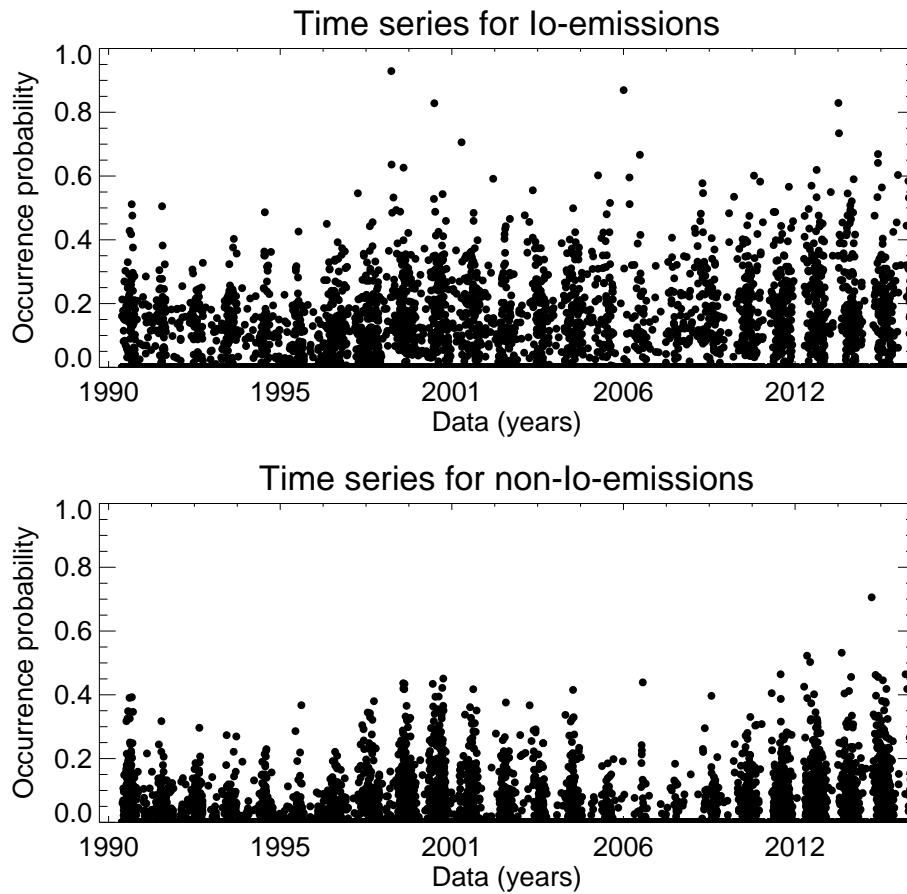
In order to search the long-term periodicities in DAM emissions and analyze how they can affect the emissions, it was studied Io and non-Io emissions separately. The reason for this approach is that each type of emission (Io and non-Io) exhibits different behaviour, as shown in chapter 4, for example, Io emissions are strongly dominated by the Io's orbital period and it can suppress the others effects.

5.2   Long-term periodicities

In order to analyze the long-term variability effects in the catalogued emissions, Io and non-Io-emission time series were subjected to a Lomb-Scargle analysis to search for periodicities in the range 100-9000 days (LOMB, 1976; SCARGLE, 1982). In the Lomb-Scargle periodogram for Io and non-Io emissions, shown in Figure 5.2, three main periods can be observed for Io and non-Io-emissions, as indicated, with higher

significance levels at 99.9999999%.

Figure 5.2 - Lomb-Scargle periodogram for Io-emissions (top panel) and non-Io-emissions (bottom panel) time series (shown in Figure 5.1) in the range 100 to 9000 days.
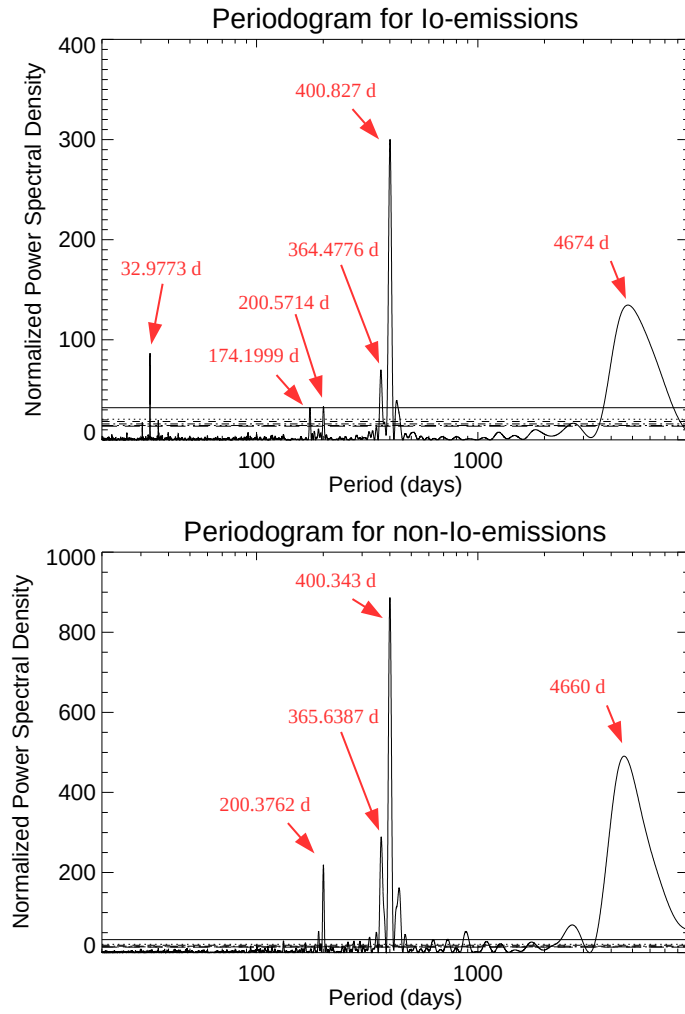
The horizontal lines show the significance levels for the method, following bottom-up, 90%, 95%, 99%, 99.9%, 99.99% and 99.9999999%.

The period of about of 4600 days is possibly caused by the D_E. This effect is responsible for the long-term variability in the occurrence probability as well as in the shift in Io-A, Io-B and Io-C positions in the CML-Φ_{Io} diagram (CARR et al., 1970; CARR et al., 1983; BOUDJADA; LEBLANC, 1992; LEBLANC et al., 1993). However, D_E period is close to the long-term solar activity period (11 years cycle) which can also induce variabilities, mainly, in non-Io-emissions (TERASAWA et al., 1978; BARROW et

al., 1986; ZARKA; GENOVA, 1983; GENOVA et al., 1987; ZARKA; GENOVA, 1989; BOSE; BHATTACHARYA, 2003; ECHER et al., 2010b; HESS et al., 2012; HESS et al., 2014). Unfortunately, the catalog covers only two cycles, cf.Figure 5.2, preventing the separation of the two periods by spectral analysis. The periods around ∼400 days are possibly caused by successive conjunctions of Jupiter with the Sun-Earth line, i.e., a period where Jupiter is blocked by the Sun. This period is known by Jupiter's synodic period (398.88 days). The 365 d period is the Earth year. The subsequent periods (around 200 days) are harmonics of this synodic period. The variabilities of the found periods are discussed separately in the following sections.

5.2.1 Declination and Solar activity effects on DAM-emissions

As discussed early, the D_E and the solar activity exhibit close periods which prevents one to distinguish both, from the catalog (two solar cycles), by spectral analysis. Thus, in Figure 5.3 we show a comparison of the Io and non-Io time series with the D_E and the solar activity (from sunspot number - S_n). The maximum and minimum values of the D_E and solar activity are indicated by the red and blue vertical lines, respectively.

It can be seen an increase in the number of emissions during the maximum values of the declination and the solar activity. The opposite behaviour is observed during the minimum values of declination and solar activity. Nevertheless, if we carefully analyze the non-Io-emission time series, it can be observed a difference in the number of emissions between the two minima. This difference may be caused by the smaller minimum of solar activity in 2009 (ECHER et al., 2011, e.g.).

In Figure 5.4, we show the occurrence probability as function of the D_E and the sunspot number for Io-emissions (top panel) and non-Io-emissions (bottom panel). It can be noted that the occurrence probabilities are distributed in bands, in both cases, possibly due to viewing geometry of observation which could favor them. In Appendix C.1, we show each band of occurrence probability distributed in CML-Φ_{Io} plane. We can also observe a trend of increasing emission density and the maximum value of the occurrence probability with declination. However, the same behaviour is not observed in occurrence probability as function of the sunspot number. Moreover, when we compare Io and non-Io emissions it can be seen a significant increase in the number and maximum value of non-Io-emission occurrence probability around of the mean value reached in the maximum solar activity (indicated by red arrows). This enhancement is more significant during the last maximum solar cycle (sunspot number mean value reached equal to 90), perhaps due to the longer duration when it

Figure 5.3 - Comparison between the declination and solar activity with Io- and non-Io-emission time series (cf. Figure 5.1).
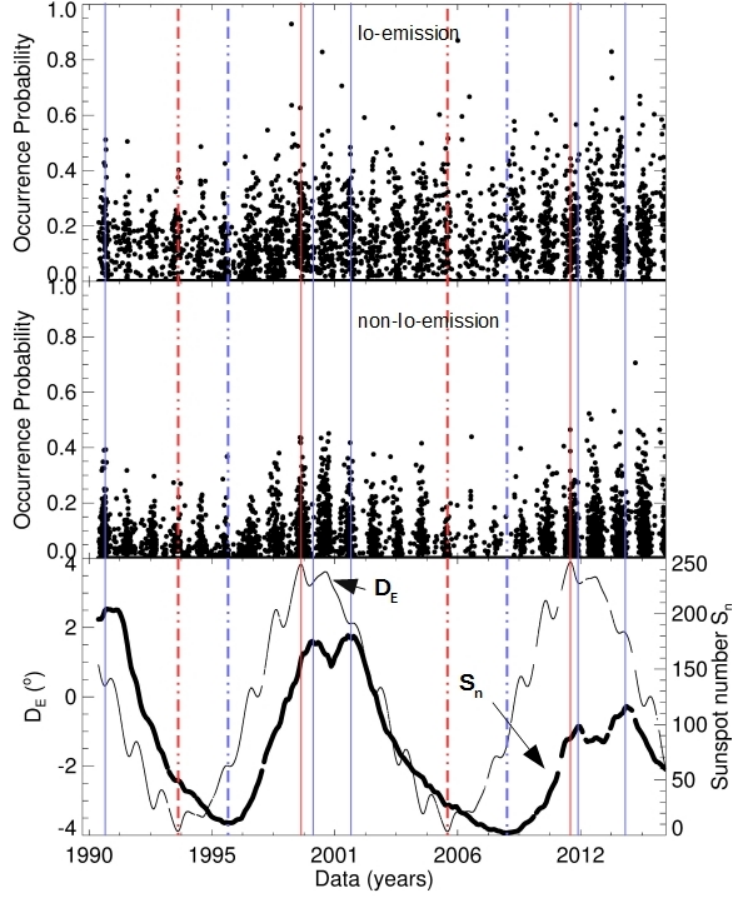
The dotted lines show the minimum values for DE (red) and sunspot number (S_n) (blue) and the continuous lines show the maximum values, respectively. The sunspot number is from SILSO (Sunspot Index and Long-term Solar Observations) in web (http://sidc.be/silso/home).

is compared to the other maxima. We also observed a decrease in emission numbers in the solar minimum period.

In Figure 5.5, we use the phase of the Jupiter's orbital period (4330.595 days) to analyze the effect of the two periods for Io and non-Io time series. The 0° of the phase of Jupiter's orbital period ($\Phi_{Jupiter's\ orbital\ period}$ or Jupiter's longitude in heliocentric system) points to the centre of the galaxy at Sagittarius A. In both cases, it can be observed a dependence of occurrence probability with the $\Phi_{Jupiter's\ orbital\ period}$ with maximum occurrence probability reaching ∼15% for Io-emission and ∼22% for non-Io-emission at 65°, that corresponds to the maximum declination and solar ac-

57

Figure 5.4 - Occurrence probability as function of D_E (left) and S_n (right) for Io (top panel) and non-Io emission (bottom panel).
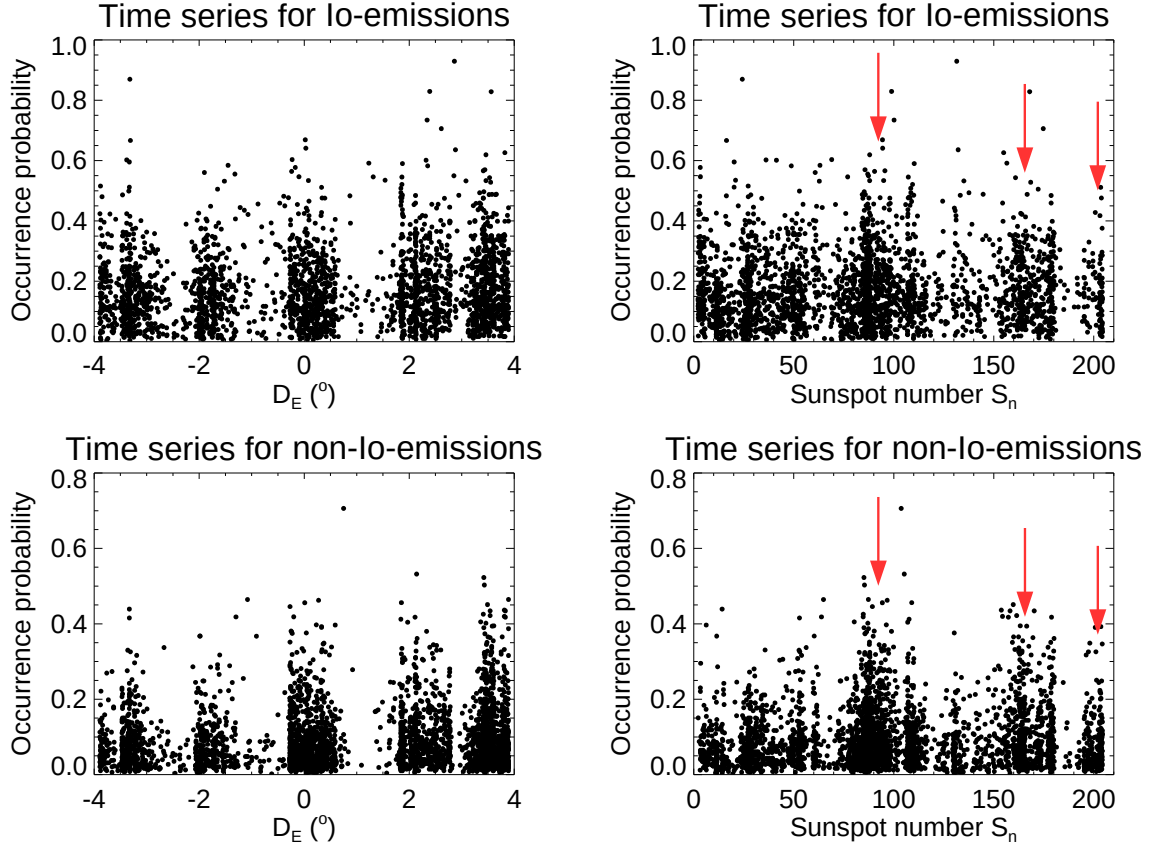
The red arrows indicate the mean value reached in the solar maximum.

tivity. However, the minimum values in both emissions, seem to follow the minimum D_E. It can also be noted in non-Io-emission that the declining phase of occurrence probability is more active than the ascending phase.

Figure 5.6 shows the occurrence probability as function of phase of the Jupiter's orbital period for Io (left) and non-Io (right) emissions separated by northern (top panel) and southern (middle panel) hemisphere. It can be observed that the northern hemisphere is more active in both cases, as shown in section 4.2, and also more affected by long-term variability, mainly for Io-emission. However, non-Io-emission shows, in both cases, that the declining phase of occurrence probability is more active than the ascent phase.

Finally in Figure 5.7, we show the occurrence probability as function of

Figure 5.5 - Occurrence probability, D_E and sunspot number as function of $\Phi_{Jupiter's\,orbital\,period}$ for Io and non-Io emissions with $0°$ points to the centre of the galaxy at Sagittarius A.
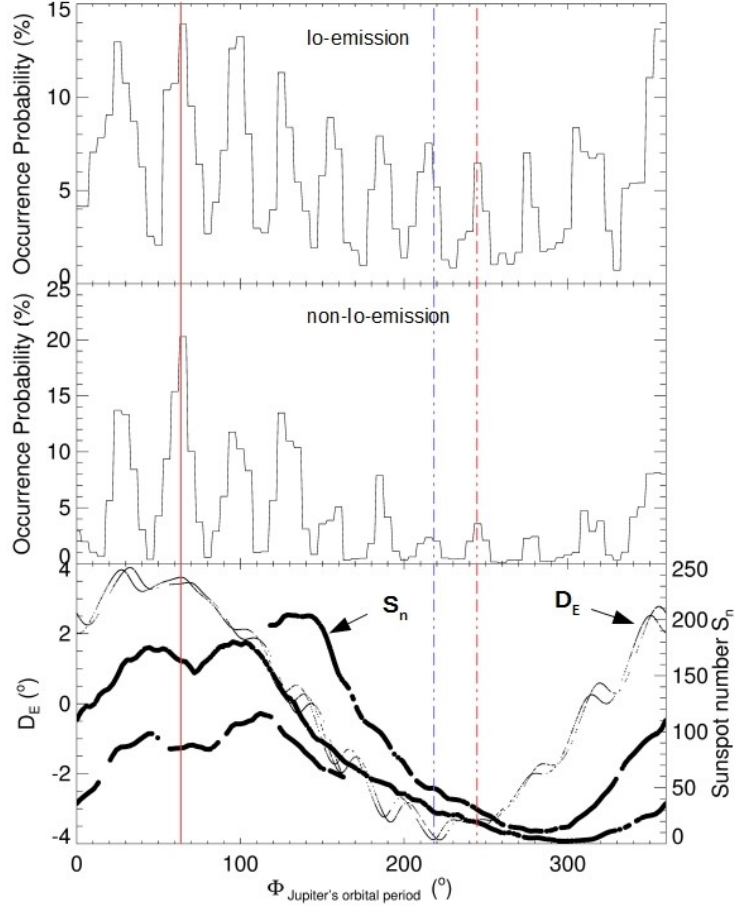
The dotted and continued vertical lines show the minimum and maximum values of the occurrence probability, respectively.

$\Phi_{Jupiter's\,orbital\,period}$, CML (left) and Φ_{Io} (right) for Io (top panel) and non-Io (bottom panel) emissions. It can be noted a contraction of the emission region in CML and Φ_{Io}, mainly in CML, during the minimum (solar and declination), especially in the dawn side (i.e. Io-B/B' and Io-D). It can also be observed a drift in the maximum value of occurrence probability in Φ_{Io} for Io-emission and CML for non-Io-emission, in the dusk side. As shown in section 4.2, the dusk side of Jupiter has a more active emission region.

The previous results indicate that there is an increase of source region (increase in the occurrence probability) as well as an increase of activity (increase in the

Figure 5.6 - Occurrence probability, D_E and sunspot number as function of $\Phi_{Jupiter's\,orbital\,period}$ for Io (left) and non-Io (right) emissions separated by northern hemisphere (top panel) and southern hemisphere (middle panel) with 0° points to the centre of the galaxy at Sagittarius A.
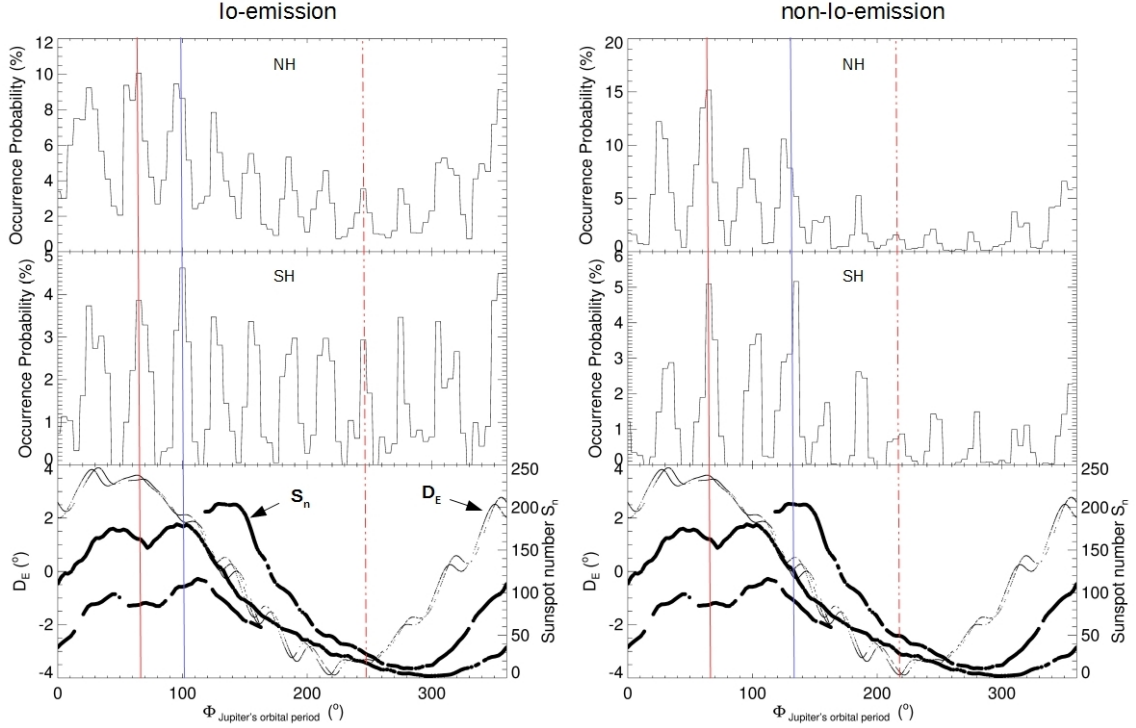
The dotted and continued vertical lines show the minimum and maximum values of the occurrence probability, respectively.

number of events) with enhancement of the declination and solar activity for both types of emission (Io and non-Io). However, the D_E effect comes from the fact that we observe different parts of a narrow emission beam that corotates with Jupiter during different apparitions of the planet (CARR et al., 1983), i.e. it is an effect from geometry of observation. This effect is known to increase the occurrence probability (cf. Figures 5.4 and 5.5) as well as in the drift in the maximum value of occurrence probability in the CML-Φ_{Io} diagram (cf. Figure 5.7).

On the other hand, several spacecraft that visited Jupiter in different conditions of solar activity (Pioneer 10 and 11 during solar minimum, Voyager 1 and 2 close to solar maximum, Ulysses during the declining phase, Galileo covered an entire ascending phase from minimum to maximum, and Cassini flew by the planet during solar maximum) showed that in general, the magnetosphere tends to be more expanded

Figure 5.7 - Occurrence probability as a function of $\Phi_{Jupiter's\ orbital\ period}$, CML (Left) and Φ_{Io} (right) for Io (top panel) and non-Io (bottom panel) emissions.
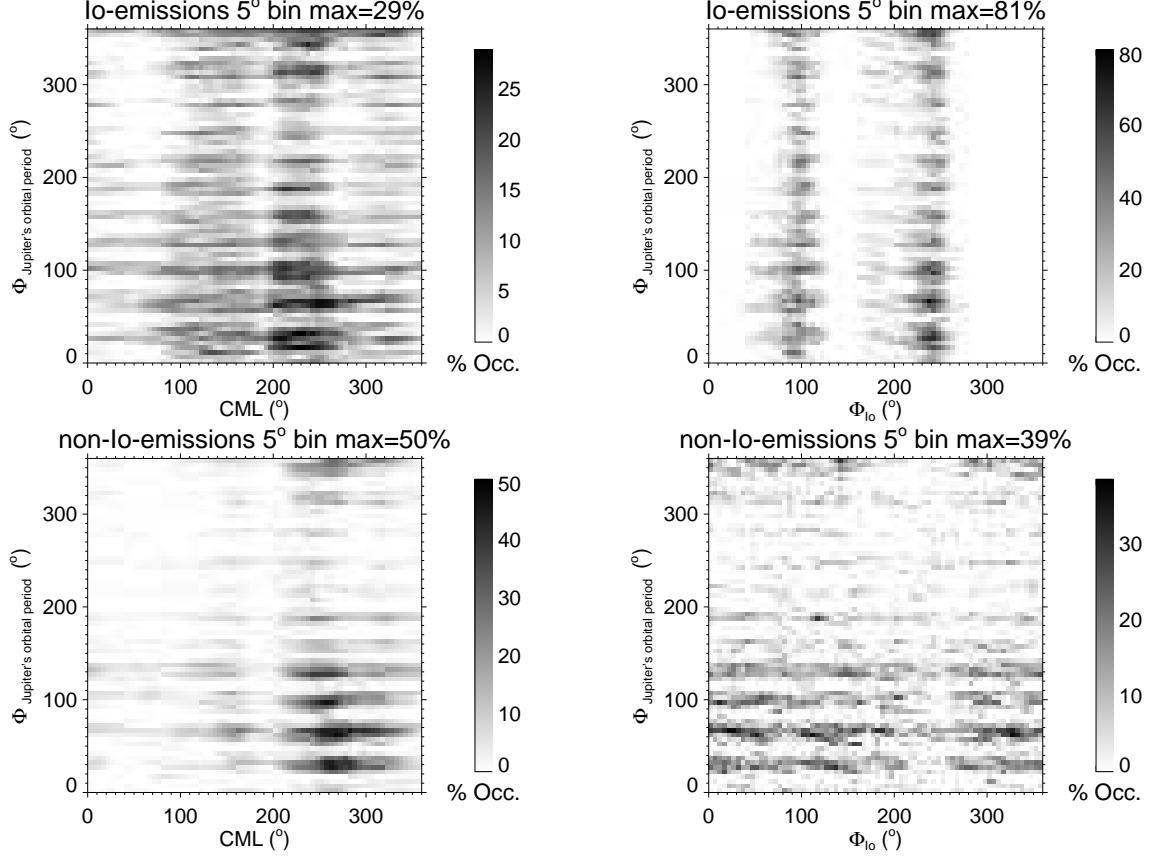
during solar minimum and compressed during solar maximum, as expected (KRUPP et al., 2004, and references therein). Furthermore, several observations have shown that during times of higher solar wind pressure the auroral and radio emissions are enhanced (cf. Figure 5.4) (BARROW et al., 1986; GENOVA et al., 1987; ZARKA; GENOVA, 1989). Moreover, other works show that radio emissions are also triggered by interplanetary shocks (TERASAWA et al., 1978; BOSE; BHATTACHARYA, 2003; ECHER et al., 2010b; HESS et al., 2012; HESS et al., 2014) which are associated with corotating interaction regions (CIRs) (SMITH; WOLFE, 1976; ECHER et al., 2010a; ECHER et al., 2010b, and references therein) present during the declining and minimum solar activity (cf. Figures 5.5 and 5.6) which plays a dominant role as a source of geomagnetic disturbances. Coronal mass ejections (CMEs or ICMEs) are also the main interplanetary phenomena which cause magnetic storms around solar maximum.

5.2.1.1 Summary & Conclusion

The results showed in this section suggest that the occurrence probability of the Io and non-Io emissions are affected by the declination and solar activity, as shown in literature. A few other results can be highlighted:

- Io-emissions seems to be modulated by the declination effect mainly in the northern hemisphere;

- long-term solar activity seems to relate to non-Io-emissions in two situations: high solar activity and declining phase;

- the results suggest that Io-emissions can also be related to the solar activity during high solar activity.

The most notable result is the possible relation between Io-emissions and the solar activity during high solar activity. However, this result needs further studied to be confirmed.

5.2.2 Synodic period effect on DAM-emissions

Jupiter's synodic period is the length of time during which Jupiter makes one orbit of the Sun relative to the Earth. At some point of this period, DAM-emission is blocked by the Sun (conjunction[1]) and we expect a decrease in the number of emission. Figure 5.8 shows the occurrence probability as function of $\Phi_{Jupiter's\, synodic\, period}$ for Io (left) and non-Io (right) emissions. The $\Phi_{Jupiter's\, synodic\, period}$ was calculated by the difference between right ascension of the Sun and Jupiter with $0°$ at the conjunction period. It can be clearly seen that both emissions have the maximum occurrence probability during the opposition, at $180°$, of the $\Phi_{Jupiter's\, synodic\, period}$ and it decreases when it goes to the conjunction. It can also be observed a peak at $330°$ of the $\Phi_{Jupiter's\, synodic\, period}$ for Io-emission and a less intense for non-Io-emission, created due to the period when Jupiter and the Sun are less than 8h apart in right ascension, as discussed in section 4.1.

Figure 5.9 shows the minimum frequency (MHz) as function of the $\Phi_{Jupiter's\, synodic\, period}$. It can be observed that the cut-off frequency due to the interplanetary plasma closer to the Sun is responsible to cut-off emissions with low

---

[1]conjunction occurs when two astronomical objects have either the same right ascension or the same ecliptic longitude, usually as observed from Earth.

frequency as consequence the occurrence probability decrease. The cut is more effective for non-Io-emission that for Io-emission due to its low frequency, as shown in chapter 4.

Finally, in Figure 5.10, we show the effect of the synodic period on the CML (left) and the Φ_{Io} (right) for Io (top panel) and non-Io (bottom panel) emissions, through the occurrence probability. It can be noticed a significant contraction of the emission source in the dawn side during the conjunction, however, no significant contraction and/or expansion was observed in the dusk side. non-Io-emissions exhibit a drift to the maximum value of occurrence probability to hight CML. Any contraction and/or expansion was observed to non-Io-emission for Φ_{Io}.

Figure 5.8 - Occurrence probability as function of $\Phi_{Jupiter's\,synodic\,period}$ for Io and non-Io emissions with 0° at the conjunction period.
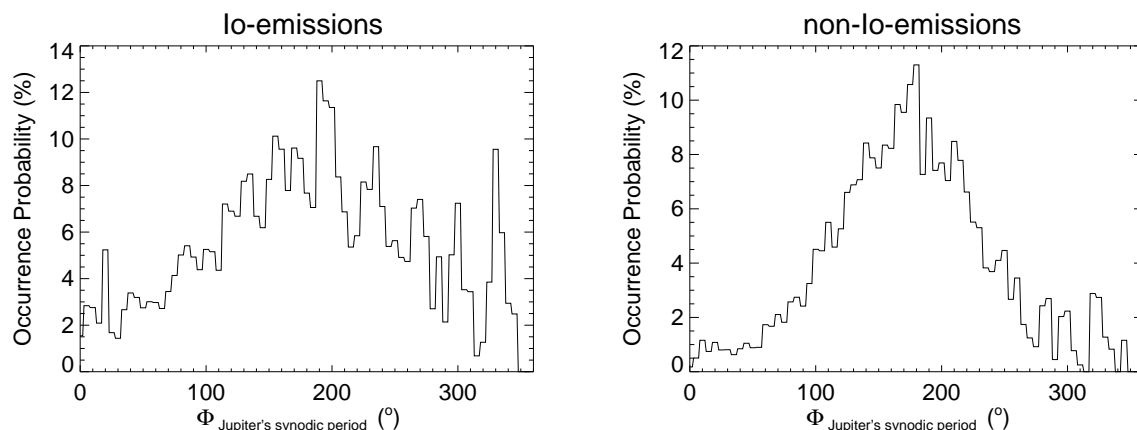
5.2.2.1 Summary & Conclusion

The synodic effect is due to the geometry of observation. However, it shows a cut-off frequency due to the the plasma surrounding the Sun which explains the gap observed in the time series distribution (cf. Figure 5.1). This study is unpublished, thus, all results are highlighted:

- cut-off frequency due to the the plasma surrounding the Sun;

- cut-off is more effective for non-Io-emission;

- contraction of the emission source in the dawn side during the conjunction.

Figure 5.9 - Minimum frequency as function of $\Phi_{Jupiter's\,synodic\,period}$.
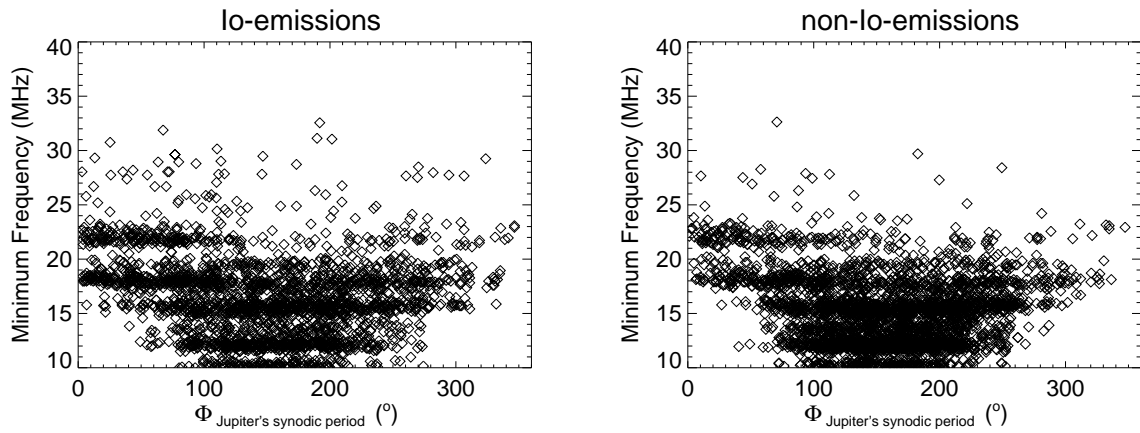
These results show important implications for detecting radio emissions from exoplanets, as highlighted bellow:

- they confirm the theoretical prediction made by Hess et al. (2011) that the star can attenuate the radio emissions of the planet;

- they also suggest that the occurrence probability depends on the position of the planet (source) and star with respect to the observed.

Figure 5.10 - Occurrence probability as function of $\Phi_{Jupiter's\,synodic\,period}$ and CML (Left) and Φ_{Io} (right) for Io (top panel) and non-Io (bottom panel) emissions.
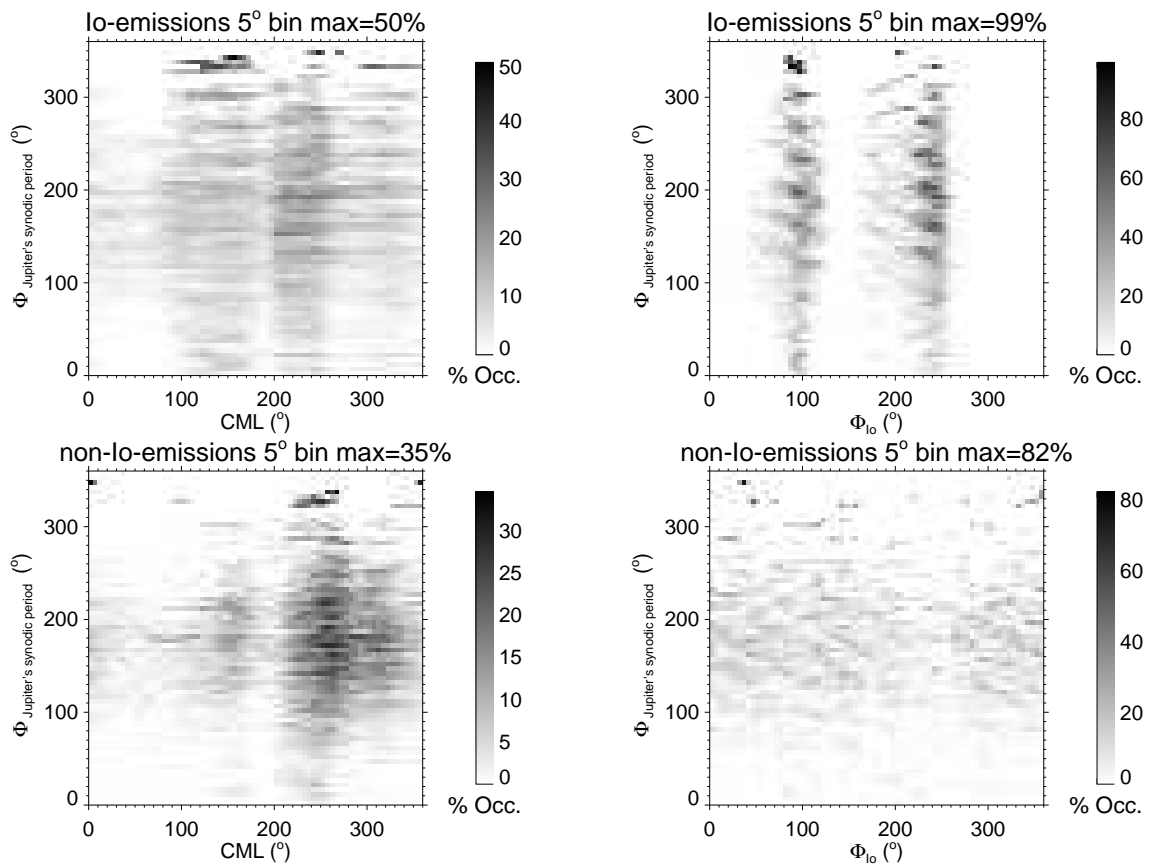
6 SUMMARY OF CONCLUSIONS AND FUTURE PERSPECTIVES

In this work, we have built a database of 26 years of observations of the DAM emissions conducted by NDA, using new criteria for the event classification into Io and non-Io emission types (Table 3.1). The cataloguing of the DAM events was performed in a way that allowed us to record extensive information on each emission. Then we have carried out a statistical analysis of this database, focussing on occurrence rates, intensity, duration, maximum frequency and polarization of the events. This study suggests a number of results listed below, the confirmation of which will motivate specific in-depth analyses:

- non-Io-DAM appears to be related to small-scale, possibly bursty auroral structures;

- northern emissions are more frequent but southern ones are more intense;

- in the case of Io emissions, the excess of northern emissions specifically concerns low intensity and low duration emissions;

- in the case of non-Io emissions, dusk emissions dominate dawn ones by occurrence, intensity and duration;

- the distribution of non-Io emissions versus the CML suggests that radiosources are preferably located above auroral regions where $d|B|/dCML{<}0$;

- the distribution of the maximum frequency of Io emissions is densely clustered versus Io's longitude Λ_{Io}; its $t-f$ envelope imposes a strong constraint on the Io-Jupiter interaction mechanism (lead angle), provided that the Jovian internal - and surface - magnetic field is well known.

The results obtained for individual emission type are generally in good agreement with previous works, but we have highlighted a few new results:

- two new Io-induced radio emission types were discovered or identified: Io-A" and Io-B', that have spectral characteristics distinct of other emission types;

- the CML$-\Phi_{Io}$ contours and maximum frequency of known emission types, especially Io-C and Io-D, are redefined (differently from the values in the

67

literature); Io-C is detected at lower CML, has a maximum frequency ∼29 MHz and exclusively LH polarization; Io-D is observed beyond published limits and has a maximum frequency higher than described in previous works;

- the non-Io-D type was detected in a broad CML range (and all Io phases), with LH polarization, maximum frequency ∼28 MHz, and low occurrence probability.

Moreover, the preliminary long-term study showed that the occurrence probability is affected by the long-term variabilities as following:

- Io-emissions seem to be modulated by the declination effect mainly in the northern hemisphere;

- long-term solar activity seems to relate to non-Io-emissions in two situations: high solar activity and declining phase;

- the results suggest that Io-emission can also be affected by the solar activity during maximum solar cycle.

- cut-off frequency due to the the plasma surrounding the Sun is more effective for non-Io-emission;

- contraction of the emission source in the dawn side during the conjunction period.

All these results, listed above, show important implications, as for examples, it may be used in future theoretical studies of Jovian DAM (e.g. by Galopeau et al. (2004), Galopeau et al. (2007)) or to extrapolate theoretical models to study radio emissions from exo-planets, or to confirm the theoretical predictions made by Hess et al. (2011). They can also be used as a reliable basis for future observations by professional as well as amateur radioastronomers (CECCONI et al., 2015, e.g.) via the detailed plots and tables of the occurrence probability of each component (Figs. 4.14 and 4.16, Table 4.2. Furthermore, it provides a framework for the study of Jovian DAM with the Juno mission (BAGENAL et al., 2014), as well as from reanalyses of past spacecraft observations (Voyager, Cassini - cf. Louis et al., submitted). One expected major outcome of the Juno mission should be a near-perfect Jovian internal field model, that will remove all uncertainty on the surface magnetic field and provide a new and

accurate frame for the analysis and interpretation of data from this database (e.g. maximum frequency variations will directly provide the lead angle of the active field line versus Λ_{Io} and the radio beaming of Io emissions).

Finally, the present database will be the support of several future works, including the control of Jovian DAM by satellites other than Io, long-term variations of the emissions (season), Faraday rotation, the solar wind influence on the outer Jovian magnetosphere, new periodicities, correlations with Spacecraft observations, and more.

REFERENCES

BAGENAL, F. The magnetosphere of jupiter: coupling the equator to the poles. **Journal of Atmospheric and Solar-Terrestrial Physics**, Elsevier, v. 69, n. 3, p. 387–402, 2007. 12, 14

BAGENAL, F.; ADRIANI, A.; ALLEGRINI, F.; BOLTON, S. J.; BONFOND, B.; BUNCE, E. J.; CONNERNEY, J. E. P.; COWLEY, S. W. H.; EBERT, R. W.; GLADSTONE, G. R.; HANSEN, C. J.; KURTH, W. S.; LEVIN, S. M.; MAUK, B. H.; MCCOMAS, D. J.; PARANICAS, C. P.; SANTOS-COSTA, D.; THORNE, R. M.; VALEK, P.; WAITE, J. H.; ZARKA, P. Magnetospheric Science Objectives of the Juno Mission. **Space Science Reviews**, feb. 2014. 68

BARROW, C. H.; DESCH, M. D. Non-io decametric radiation from jupiter at frequencies above 30 mhz. **Astronomy and Astrophysics**, v. 86, p. 339–341, 1980. 34

BARROW, C. H.; GENOVA, F.; DESCH, M. D. Solar wind control of jupiter's decametric radio emission. **Astronomy and Astrophysics**, v. 165, p. 244–250, 1986. 2, 16, 55, 56, 61

BIGG, E. K. Influence of the satellite io on jupiter's decametric emission. **Nature**, v. 203, p. 1008–1010, 1964. 1, 5, 6, 14

_____. Periodicities in jupiter's decametric radiation. **Planetary and Space Science**, Elsevier, v. 14, n. 8, p. 741–758, 1966. 1, 53

BOISCHOT, A.; AUBIER, M. The jovian decametric arcs as an interference pattern. **Journal of Geophysical Research: Space Physics**, Wiley Online Library, v. 86, n. A10, p. 8561–8563, 1981. 4, 5

BOISCHOT, A.; ROSOLEN, C.; AUBIER, M. G.; DAIGNE, G.; GENOVA, F.; LEBLANC, Y.; LECACHEUX, A.; NOE, J. de L. et al. A new high-grain, broadband, steerable array to study jovian decametric emission. **Icarus**, Elsevier, v. 43, n. 3, p. 399–407, 1980. 2, 18, 19

BONFOND, B.; HESS, S.; GÉRARD, J.-C.; GRODENT, D.; RADIOTI, A.; CHANTRY, V.; SAUR, J.; JACOBSEN, S.; CLARKE, J. T. Evolution of the Io footprint brightness I: Far-UV observations. **Planetary and Space Science**, v. 88, p. 64–75, nov. 2013. 37

BOSE, S. K.; BHATTACHARYA, A. B. Solar plasma activated decametric radio emission of non-io origin from jupiter magnetosphere. **Indian Journal of Radio and Space Physics**, PUBLICATIONS & INFORMATION DIRECTORATE, CSIR, v. 32, n. 1, p. 43–51, 2003. 2, 16, 55, 56, 61

BOSE, S. K.; SARKAR, S.; BHATTACHARYYA, A. B. Jovian decametric radio emissions: An overview of the planetary radio astronomical observations. **Indian Journal of Radio and Space Physics**, v. 37, p. 77–108, 2008. 50

BOUDJADA, M. Y.; LEBLANC, Y. The variability of jovian decametric radiation from 1978 to 1988. **Advances in Space Research**, Elsevier, v. 12, n. 8, p. 95–98, 1992. 55

BOUDJADA, M. Y.; RUCKER, H. O.; LADREITER, P. H. The io-c jovian decameter emissions. **Astronomy and Astrophysics**, v. 303, p. 255, 1995. 46

BURKE, B. F.; FRANKLIN, K. L. Observations of a variable radio source associated with the planet jupiter. **Journal of Geophysical Research**, Wiley Online Library, v. 60, n. 2, p. 213–217, 1955. 1, 3

CARR, T. D.; DESCH, M. D.; ALEXANDER, J. K. **Phenomenology of magnetospheric radio emissions**. [S.l.: s.n.], 1983. 226–284 p. 1, 6, 16, 17, 29, 32, 46, 47, 48, 49, 50, 53, 55, 60

CARR, T. D.; SMITH, A. G.; DONIVAN, F. F.; REGISTER, H. I. Twelve-year periodicities in jupiter's decametric radiation. In: **Bulletin of the American Astronomical Society**. [S.l.: s.n.], 1970. v. 2, p. 186. 55

CECCONI, B.; HESS, S. L. G.; SIDANER, P. L.; SAVALLE, R.; ERARD, S.; COFFRE, A.; THÉTAS, E.; ANDRÉ, N.; GÉNOT, V.; THIEMAN, J.; TYPINSKI, D.; SKY, J.; HIGGINS, C. Virtual Observatory tools and Amateur Radio Observations Supporting Scientific Analysis of Jupiter Radio Emissions. **European Planetary Science Congress 2015, held 27 September - 2 October, 2015 in Nantes, France, Online at <A href="http://meetingorganizer.copernicus.org/EPSC2015/EPSC2015"> http://meetingorganizer.copernicus.org/EPSC2015</A>, id.EPSC2015-140**, v. 10, p. EPSC2015–140, oct. 2015. 68

CLARKE, J. T.; GRODENT, D.; COWLEY, S. W. H.; BUNCE, E. J.; ZARKA, P.; CONNERNEY, J. E. P.; SATOH, T. Jupiter's aurora. In: _____. **Jupiter: the planet, satellites and magnetosphere**. [S.l.: s.n.], 2004. p. 639–670. 13, 14

CLARKE, J. T.; NICHOLS, J.; GÉRARD, J.-C.; GRODENT, D.; HANSEN, K. C.; KURTH, W.; GLADSTONE, G. R.; DUVAL, J.; WANNAWICHIAN, S.; BUNCE, E. et al. Response of jupiter's and saturn's auroral activity to the solar wind. **Journal of Geophysical Research: Space Physics**, Wiley Online Library, v. 114, n. A5, 2009. 37

CLARKE, T. E.; HIGGINS, C. A.; SKARDA, J.; IMAI, K.; IMAI, M.; REYES, F.; THIEMAN, J.; JAEGER, T.; SCHMITT, H.; DALAL, N. P. et al. Probing jovian decametric emission with the long wavelength array station 1. **Journal of Geophysical Research: Space Physics**, Wiley Online Library, v. 119, n. 12, p. 9508–9526, 2014. 48

CONNERNEY, J. E. P. Magnetic fields of the outer planets. **Journal of Geophysical Research: Planets**, Wiley Online Library, v. 98, n. E10, p. 18659–18679, 1993. 10

DULK, G. A.; LEBLANC, Y.; LECACHEUX, A. The complete polarization state of Io-related radio storms from Jupiter: A statistical study. **Astronomy and Astrophysics**, v. 286, p. 683–700, jun. 1994. 34

DULK, G. A.; LECACHEUX, A.; LEBLANC, Y. The complete polarization state of a storm of millisecond bursts from jupiter. **Astronomy and Astrophysics**, v. 253, p. 292–306, 1992. 34

ECHER, E.; TSURUTANI, B. T.; GONZALEZ, W. D. Extremely low geomagnetic activity during the recent deep solar cycle minimum. **Proceedings of the International Astronomical Union**, Cambridge Univ Press, v. 7, n. S286, p. 200–209, 2011. 56

ECHER, E.; TSURUTANI, B. T.; GUARNIERI, F. L. Forward and reverse cir shocks at 4–5au: Ulysses. **Advances in Space Research**, Elsevier, v. 45, n. 6, p. 798–803, 2010. 61

ECHER, E.; ZARKA, P.; GONZALEZ, W. D.; MORIOKA, A.; DENIS, L. Solar wind effects on jupiter non-io dam emissions during ulysses distant encounter (2003–2004). **Astronomy & Astrophysics**, EDP Sciences, v. 519, p. A84, 2010. 2, 16, 55, 56, 61

GALLET, R. M. Radio Observations of Jupiter. II. In: _____. **Planets and Satellites**. [S.l.: s.n.], 1961. p. 500. 4

GALOPEAU, P. H. M.; BOUDJADA, M. Y.; RUCKER, H. O. Evidence of jovian active longitude: 1. efficiency of cyclotron maser instability. **Journal of Geophysical Research: Space Physics**, Wiley Online Library, v. 109, n. A12, 2004. 8, 10, 68, 81

_____. Evidence of jovian active longitude: 2. a parametric study. **Journal of Geophysical Research: Space Physics**, Wiley Online Library, v. 112, n. A4, 2007. 10, 68

GENOVA, F.; AUBIER, M. G. Io-dependent sources of the jovian decameter emission. **Astronomy and Astrophysics**, v. 150, p. 139–150, 1985. 37, 42

GENOVA, F.; AUBIER, M. G.; LECACHEUX, A. Modulations in jovian decametric spectra-propagation effects in terrestrial ionosphere and jovian environment. **Astronomy and Astrophysics**, v. 104, p. 229–239, 1981. 4

GENOVA, F.; ZARKA, P.; BARROW, C. H. Voyager and nancay observations of the jovian radio-emission at different frequencies-solar wind effect and source extent. **Astronomy and Astrophysics**, v. 182, p. 159–162, 1987. 2, 16, 55, 56, 61

GENOVA, F.; ZARKA, P.; LECACHEUX, A. Jupiter decametric radiation. **NASA Special Publication**, v. 494, 1989. 5, 6, 7, 8, 29, 32, 46, 50

GÉRARD, J.-C.; BONFOND, B.; GRODENT, D.; RADIOTI, A.; CLARKE, J. T.; GLADSTONE, G. R.; WAITE, J. H.; BISIKALO, D.; SHEMATOVICH, V. I. Mapping the electron energy in Jupiter's aurora: Hubble spectral observations. **Journal of Geophysical Research: Space Physics**, v. 119, p. 9072–9088, nov. 2014. 34

GÉRARD, J.-C.; GRODENT, D.; RADIOTI, A.; BONFOND, B.; CLARKE, J. T. Hubble observations of Jupiter's north-south conjugate ultraviolet aurora. **Icarus**, v. 226, p. 1559–1567, nov. 2013. 33

GUSTIN, J.; GRODENT, D.; RAY, L. C.; BONFOND, B.; BUNCE, E. J.; NICHOLS, J. D.; OZAK, N. Characteristics of north jovian aurora from STIS FUV spectral images. **Icarus**, v. 268, p. 215–241, apr. 2016. 34

HESS, S.; CECCONI, B.; ZARKA, P. Modeling of io-jupiter decameter arcs, emission beaming and energy source. **Geophysical Research Letters**, Wiley Online Library, v. 35, n. 13, 2008. 1, 10, 11, 16, 32, 46, 47, 49

HESS, S.; ZARKA, P.; MOTTEZ, F. Io-jupiter interaction, millisecond bursts and field-aligned potentials. **Planetary and Space Science**, Elsevier, v. 55, n. 1, p. 89–99, 2007. 4, 5, 7

HESS, S. L. G.; BONFOND, B.; ZARKA, P.; GRODENT, D. Model of the jovian magnetic field topology constrained by the io auroral emissions. **Journal of Geophysical Research: Space Physics**, Wiley Online Library, v. 116, n. A5, 2011. 37, 39, 42, 64, 68

HESS, S. L. G.; ECHER, E.; ZARKA, P. Solar wind pressure effects on jupiter decametric radio emissions independent of io. **Planetary and Space Science**, Elsevier, v. 70, n. 1, p. 114–125, 2012. 2, 4, 5, 16, 37, 55, 56, 61

HESS, S. L. G.; ECHER, E.; ZARKA, P.; LAMY, L.; DELAMERE, P. A. Multi-instrument study of the jovian radio emissions triggered by solar wind shocks and inferred magnetospheric subcorotation rates. **Planetary and Space Science**, Elsevier, v. 99, p. 136–148, 2014. 2, 16, 37, 55, 56, 61

HESS, S. L. G.; PÉTIN, A.; ZARKA, P.; BONFOND, B.; CECCONI, B. Lead angles and emitting electron energies of io-controlled decameter radio arcs. **Planetary and Space Science**, Elsevier, v. 58, n. 10, p. 1188–1198, 2010. 23

HESS, S. L. G.; ZARKA, P. Modeling the radio signature of the orbital parameters, rotation, and magnetic field of exoplanets. **Astronomy and Astrophysics**, EDP Sciences, v. 531, p. A29, 2011. 1

HIGGINS, C. A.; CARR, T. D.; REYES, F.; GREENMAN, W. B.; LEBO, G. R. A redefinition of jupiter's rotation period. **Journal of Geophysical Research: Space Physics**, Wiley Online Library, v. 102, n. A10, p. 22033–22041, 1997. 1, 4, 5

HIGGINS, C. A.; MENIETTI, J. D.; CHRISTOPHER, I. W. Europa control of jovian radio emission: A galileo study. **Geophysical research letters**, v. 33, n. 14, 2006. 1, 15

HILL, T. W. The jovian auroral oval. **Journal of geophysical research**, v. 106, p. 8101–8107, 2001. 14

IMAI, K.; WANG, L.; CARR, T. D. A model for the production of jupiter's decametric modulation lanes. **Geophysical research letters**, v. 19, n. 9, p. 953–956, 1992. 4

KAISER, M. L. Time-variable magnetospheric radio emissions from jupiter. **Journal of Geophysical Research: Planets**, Wiley Online Library, v. 98, n. E10, p. 18757–18765, 1993. 53

KEPLER, S. O.; SARAIVA, M. F. Astronomia e astrofísica. **Porto Alegre: Editora da**, 2004. 19

KHURANA, K. K.; KIVELSON, M. G.; VASYLIUNAS, V. M.; KRUPP, N.; WOCH, J.; LAGG, A.; MAUK, B. H.; KURTH, W. S. The configuration of jupiter's magnetosphere. In: _____. **Jupiter: the planet, satellites and magnetosphere**. [S.l.]: Cambridge University Press, New York, 2004. v. 1, p. 593–616. 12, 13, 14

KIVELSON, M. G.; BAGENAL, F.; KURTH, W. S.; NEUBAUER, F. M.; PARANICAS, C.; SAUR, J. Magnetospheric interactions with satellites. In: _____. **Jupiter: the planet, satellites and magnetosphere**. [S.l.]: Cambridge University Press Cambridge, UK, 2004. p. 513–536. 15

KIVELSON, M. G.; SOUTHWOOD, D. J. Dynamical consequences of two modes of centrifugal instability in Jupiter's outer magnetosphere. **Journal of Geophysical Research: Space Physics**, v. 110, p. A12209, dec. 2005. 38

KRUPP, N.; VASYLIUNAS, V. M.; WOCH, J.; LAGG, A.; KHURANA, K. K.; KIVELSON, M. G.; MAUK, B. H.; ROELOF, E. C.; WILLIAMS, D. J.; KRIMIGIS, S. M. et al. Dynamics of the jovian magnetosphere. In: _____. **Jupiter: the planet, satellites and magnetosphere**. [S.l.: s.n.], 2004. v. 1, p. 617–638. 16, 61

LADREITER, H. P.; ZARKA, P.; LECACHEUX, A. Direction finding study of jovian hectometric and broadband kilometric radio emissions: Evidence for their auroral origin. **Planetary and Space Science**, v. 42, n. 11, p. 919–931, 1994. 15

LAMY, L.; ZARKA, P.; CECCONI, B.; HESS, S.; PRANGÉ, R. Modeling of saturn kilometric radiation arcs and equatorial shadow zone. **Journal of Geophysical Research: Space Physics**, Wiley Online Library, v. 113, n. A10, 2008. 1

LEBLANC, Y. On the arc structure of the dam jupiter emission. **Journal of Geophysical Research: Space Physics**, Wiley Online Library, v. 86, n. A10, p. 8546–8560, 1981. 48

LEBLANC, Y.; GERBAULT, A.; DENIS, L.; LECACHEUX, A. A catalogue of jovian decametric radio observations from january 1988 to december 1990. **Astronomy and Astrophysics Supplement Series**, v. 98, p. 529–546, 1993. 2, 18, 21, 55

LEBLANC, Y.; GERBAULT, A.; LECACHEUX, A. A catalogue of jovian decametric radio observations from january 1982 to december 1984. **Astronomy and Astrophysics Supplement Series**, v. 77, p. 425–438, 1989. 2, 18, 21

LEBLANC, Y.; GERBAULT, A.; LECACHEUX, A.; BOUDJADA, M. Y. A catalogue of jovian decametric radio observations from january 1985 to december 1987. **Astronomy and Astrophysics Supplement Series**, v. 86, p. 191–207, 1990. 2, 18, 21

LEBLANC, Y.; GERBAULT, A.; RUBIO, M.; GENOVA, F. A catalogue of jovian radio observations from january 1980 to december 1981. **Astronomy and Astrophysics Supplement Series**, v. 54, p. 135–148, 1983. 2, 18, 21

LEBLANC, Y.; NOE, J. de L.; GENOVA, F.; GERBAULT, A.; LECACHEUX, A. A catalogue of jovian decametric radio observations from january 1978 to december 1979. **Astronomy and Astrophysics Supplement Series**, v. 46, p. 135–149, 1981. 2, 18, 21

LECACHEUX, A.; KONOVALENKO, A. A.; RUCKER, H. O. Using large radio telescopes at decametre wavelengths. **Planetary and Space Science**, Elsevier, v. 52, n. 15, p. 1357–1374, 2004. 4, 19

LOMB, N. R. Least-squares frequency analysis of unequally spaced data. **Astrophysics and space science**, Springer, v. 39, n. 2, p. 447–462, 1976. 54

LOUARN, P.; PARANICAS, C. P.; KURTH, W. S. Global magnetodisk disturbances and energetic particle injections at jupiter. **Journal of Geophysical Research: Space Physics**, v. 119, n. 6, p. 4495–4511, 2014. 15

MENIETTI, J. D.; GURNETT, D. A.; CHRISTOPHER, I. Control of jovian radio emission by callisto. **Geophys. Res. Lett**, v. 28, n. 15, p. 3047–3050, 2001. 1, 15

MENIETTI, J. D.; GURNETT, D. A.; KURTH, W. S.; GROENE, J. B. Control of jovian radio emission by ganymede. **Geophysical research letters**, v. 25, n. 23, p. 4281–4284, 1998. 1, 15

NICHOLS, J. D.; BADMAN, S. V.; BUNCE, E. J.; CLARKE, J. T.; COWLEY, S. W. H.; CRARY, F. J.; DOUGHERTY, M. K.; GÉRARD, J.-C.; GRODENT, D.; HANSEN, K. C.; KURTH, W. S.; MITCHELL, D. G.; PRYOR, W. R.; STALLARD, T. S.; TALBOYS, D. L.; WANNAWICHIAN, S. Saturn's equinoctial auroras. **Geophys. Res. Lett**, v. 36, p. L24102, dec. 2009. 37

PRANGÉ, R.; REGO, D.; PALLIER, L.; CONNERNEY, J.; ZARKA, P.; QUEINNEC, J. Detailed study of FUV Jovian auroral features with the post-COSTAR HST faint object camera. **Journal of Geophysical Research: Planets**, v. 103, p. 20195–20216, sep. 1998. 33

PRANGÉ, R.; REGO, D.; SOUTHWOOD, D.; ZARKA, P.; MILLER, S.; IP, W. Rapid energy dissipation and variability of the Io–jupiter electrodynamic circuit. **Nature**, v. 379, n. 6563, p. 323–325, 1996. 14

QUEINNEC, J.; ZARKA, P. Io-controlled decameter arcs and io-jupiter interaction. **Journal of Geophysical Research: Space Physics**, Wiley Online Library, v. 103, n. A11, p. 26649–26666, 1998. 1, 4, 7, 16, 23, 46, 47, 49, 53

_____. Flux, power, energy and polarization of Jovian S-bursts. **Planetary and Space Science**, v. 49, p. 365–376, mar. 2001. 34, 50

RYABOV, V. B.; ZARKA, P.; HESS, S.; KONOVALENKO, A.; LITVINENKO, G.; ZAKHARENKO, V.; SHEVCHENKO, V. A.; CECCONI, B. Fast and slow frequency-drifting millisecond bursts in jovian decametric radio emissions. **Astronomy & Astrophysics**, EDP Sciences, v. 568, p. A53, 2014. 4

SAUR, J.; NEUBAUER, F. M.; CONNERNEY, J. E. P.; ZARKA, P.; KIVELSON, M. G. Plasma interaction of io with its plasma torus. In: _____. **Jupiter: the planet, satellites and magnetosphere**. [S.l.]: Cambridge University Press Cambridge, UK, 2004. v. 1, p. 537–560. 38

SCARGLE, J. D. Studies in astronomical time series analysis. ii-statistical aspects of spectral analysis of unevenly spaced data. **The Astrophysical Journal**, v. 263, p. 835–853, 1982. 54

SMITH, E. J.; FILLIUS, R. W.; WOLFE, J. H. Compression of jupiter's magnetosphere by the solar wind. **Journal of Geophysical Research: Space Physics**, v. 83, n. A10, p. 4733–4742, 1978. 16

SMITH, E. J.; WOLFE, J. H. Observations of interaction regions and corotating shocks between one and five au: Pioneers 10 and 11. **Geophysical Research Letters**, Wiley Online Library, v. 3, n. 3, p. 137–140, 1976. 61

TERASAWA, T.; MAEZAWA, K.; MACHIDA, S. Solar wind effect on jupiter's non-io-related radio emission. Nature Publishing Group, 1978. 2, 16, 55, 56, 61

THIEMAN, J. R. A catalog of jovian decameter-wave radio observations from 1957-1978. **NASA STI/Recon Technical Report N**, v. 79, 1979. 2, 18

THIEMAN, J. R.; SMITH, A. G.; MAY, J. Motion of jupiter's decametric sources in io phase. **Astrophysical Letters**, v. 16, p. 83–86, 1975. 2, 18

TREUMANN, R. A. The electron–cyclotron maser for astrophysical application. **The Astronomy and Astrophysics Review**, v. 13, n. 4, p. 229–315, 2006. 1, 7

WARWICK, J. W.; DULK, G. A.; RIDDLE, A. C. **Observations of Jupiter's sporatic radio emission in the range 7.6-80 MHz 10 December 1971-21 March 1975**. [S.l.: s.n.], 1975. 2, 18

WU, C. S. Kinetic cyclotron and synchrotron maser instabilities: Radio emission processes by direct amplification of radiation. **Space Science Reviews**, Springer, v. 41, n. 3-4, p. 215–298, 1985. 8, 37, 81

WU, C. S.; LEE, L. C. A theory of the terrestrial kilometric radiation. **The Astrophysical Journal**, v. 230, p. 621–626, 1979. 1, 7, 8, 81, 83

ZARKA, P. Auroral radio emissions at the outer planets: Observations and theories. **Journal of Geophysical Research: Planets**, Wiley Online Library, v. 103, n. E9, p. 20159–20194, 1998. 1, 3, 7, 14, 15, 16, 32

_____. Fast radio imaging of jupiter's magnetosphere at low-frequencies with lofar. **Planetary and Space Science**, v. 52, n. 15, p. 1455–1467, 2004. 9, 15, 33

ZARKA, P.; FARGES, T.; RYABOV, B. P.; ABADA-SIMON, M.; DENIS, L. A scenario for jovian s-bursts. **Geophysical research letters**, Wiley Online Library, v. 23, n. 2, p. 125–128, 1996. 37

ZARKA, P.; GENOVA, F. Low-frequency jovian emission and solar wind magnetic sector structure. **Nature**, Nature Publishing Group, v. 306, n. 5945, p. 767–768, 1983. 2, 16, 55, 56

_____. Solar wind effect on jovian low-frequency magnetospheric radio emissions from ground-based and spacecraft observations. **NASA Special Publication**, v. 494, 1989. 2, 16, 55, 56, 61

ZARKA, P.; LANGMAYR, D.; GERBAULT, A.; DENIS, L.; COFFRE, A.; KORVER, F. Lead angle of io-controlled radio emission: Alfvén wave or slow shock. **Magnetospheres of the Outer Planets**, 2002. 42

ZARKA, P.; QUEINNEC, J.; CRARY, F. J. Low-frequency limit of Jovian radio emissions and implications on source locations and Io plasma wake. **Planetary and Space Science**, v. 49, p. 1137–1149, aug. 2001. 31

ZARKA, P.; TAGGER, M.; CECCONI, B. Radioastronomie basses frequences, ecole thematique du cnrs, goutelas (loire). In: OBSERVATOIRE DE PARIS ET SOCIETE FRANCAISE D'ASTRONOMIE ET D'ASTROPHYSIQUE (SF2A), Paris, France. **Radioastronomie Basses Frequences, Ecole thematique du CNRS, Goutelas (Loire), Proceedings of the conference held 4-8 juin 2007. Edited by P. Zarka, M. Tagger, and B. Cecconi. Paris:**. [S.l.], 2011. v. 1. 16

APPENDIX A

A.1 Cyclotron Maser Instability (CMI)

The Cyclotron Maser Instability (CMI) is created due the interaction between the electrons distribution with a relativistic speed $\vec{v}$ and an elliptically polarized wave, with frequency ω and wave vector $\vec{k}$. We have shown here a few details of how we can obtain the growth rate of the CMI. If the reader are interested in to get more details, please see Wu and Lee (1979), Wu (1985) and Galopeau et al. (2004).

To demonstrate the theoretical deduction of the CMI we should consider a magnetized plasma, which can be described by the Vlasov equation (eq. A.1) (each specie of the plasma is characterized by its index α):

$$\frac{\partial f_\alpha}{\partial t} + \vec{v} \cdot \frac{\partial f_\alpha}{\partial \vec{r}} + \vec{F} \cdot \frac{\partial f_\alpha}{\partial \vec{p}} = 0, \tag{A.1}$$

as the medium of propagation of electromagnetic waves, described by the Maxwell equations (eq. A.2):

$$\begin{aligned}
\nabla \cdot \vec{E} &= \frac{\rho}{\epsilon_0}, \\
\nabla \times \vec{E} &= -\frac{\partial \vec{B}}{\partial t}, \\
\nabla \cdot \vec{B} &= 0, \\
\nabla \times \vec{B} &= \mu_0 \vec{J} + \epsilon_0 \mu_0 \frac{\partial \vec{E}}{\partial t}.
\end{aligned} \tag{A.2}$$

The distribution function $f_\alpha = f_\alpha(t, \vec{r}, \vec{p})$ is defined in order that $d^6 n = f_\alpha(t, \vec{r}, \vec{p}) d^3\vec{r} d^3\vec{v}$ is the number of specie (ions or electrons) contained in a size box $d^3\vec{r} d^3\vec{v}$ in phase space $(\vec{r}, \vec{p})$. The charge and current density are:

$$\begin{aligned}
\rho &= \int \int \int \sum_\alpha q_\alpha f_\alpha(t, \vec{r}, \vec{p}) d^3\vec{p}, \\
\vec{J} &= \int \int \int \sum_\alpha q_\alpha f_\alpha(t, \vec{r}, \vec{p}) \vec{v} d^3\vec{p},
\end{aligned} \tag{A.3}$$

where q_α is the charge of specie α.

We assumed the plasma to be homogeneous and immersed in a uniform magnetic field $\vec{B}_0$, with perturbation waves proportional to $exp^{i(\vec{k}\cdot\vec{r}-\omega t)}$. So, taking into account the considerations proposed and introducing the following notation:

$$E_\pm = E_x \pm iE_y$$
$$E_\parallel = E_z$$

with the z axis parallel to the $\vec{B}_0$ (where E_+ and E_- denote the electric field circular left and right polarization, respectively), we can find the electric field of the perturbation wave using the equations (A.1, A.2, A.3):

$$D(\vec{k},\omega) \cdot \begin{pmatrix} E_+ \\ E_- \\ E_\parallel \end{pmatrix} = \begin{pmatrix} 0 \\ 0 \\ 0 \end{pmatrix}, \tag{A.4}$$

where $D(\vec{k},\omega)$ is a square matrix:

$$D(\vec{k},\omega) = \begin{pmatrix} \frac{k}{2} - \frac{i\mu_0\omega}{4}J_+ & \frac{k}{2} - \frac{i\mu_0\omega}{4}J_- & i\mu_0 c^2 k_\perp R \\ \frac{k}{2i} - \frac{\mu_0\omega}{4}J_+ & -\frac{k}{2i} + \frac{\mu_0\omega}{4}J_- & 0 \\ 0 & 0 & K + i\mu_0 c^2 k_\parallel R - i\mu_0\omega J_\parallel \end{pmatrix}, \tag{A.5}$$

with

$$K = \left(k^2 - \frac{\omega^2}{c^2}\right),$$

and

$$R = \frac{e^2}{2i\pi} \int \int_D \frac{\partial f/\partial p_\parallel}{\gamma m\omega - k_\parallel p_\parallel} \gamma m p_\perp dp_\parallel dp_\perp,$$

82

$$J_\pm = \frac{e^2}{2i\pi} \int \int_D \frac{\partial f/\partial p_\perp}{\gamma m\omega - k_\parallel p_\parallel \pm m\omega_c} p_\parallel p_\perp dp_\parallel dp_\perp,$$

$$J_\parallel = \frac{e^2}{2i\pi} \int \int_D \frac{\partial f/\partial p_\parallel}{\gamma m\omega - k_\parallel p_\parallel} p_\parallel p_\perp dp_\parallel dp_\perp,$$

where $\omega_c = eB_0/m$, e and m being respectively the charge and mass of electron, γ referring to the Lorentz factor and the integration domain is $D = \left\{ \left(p_\parallel, p_\perp\right) \in \mathbf{R} \times \mathbf{R}_+ \right\}$. We have also assumed only a electron distribution function $f_e = f$.

The general dispersion equation of waves can be obtained by putting the determinant of the matrix (eq. A.5) equals to zero. In the case described here, we consider only the growth rate of waves with right-hand polarization, which has a stronger interaction with the electron population with cyclotron motion. Thus, $E_+ = E_\parallel = 0$ in the eq. (A.5), and we can assume that the electron distribution to be non relativistic, in other words, we can define $\vec{p} = m\vec{v}$ or $\gamma = 1$ in everywhere except at the denominator where $\omega \simeq \omega_c$. One can also introduce the distribution function in velocity, $f(v_\parallel, v_\perp) = m^3 f(p_\parallel, p_\perp)$. So we can rewrite the eq. A.5 as following:

$$k^2 - \frac{\omega^2}{c^2} - \frac{\mu_0 e^2 \omega}{4\pi m} \int \int_D \frac{\partial f/\partial v_\perp}{\omega - k_\parallel v_\parallel - \omega_c/\gamma} v_\perp^2 dv_\parallel dv_\perp = 0, \qquad (A.6)$$

with $\omega = \omega_r + i\omega_i \in \mathbf{C}$. The imaginary part of the ω represents the growth rate of the waves ($\omega_i > 0$ corresponds to an instability). Assuming that $|\omega_i| << \omega_r$, and apply Plemelj's formula[1] to eq. (A.6) we derive the growth rate of the unstable waves:

$$\omega_i = \frac{\omega_p}{8} \int_0^{+\infty} v_\perp^2 dv_\perp \int_{-\infty}^{+\infty} \frac{\partial f}{\partial v_\perp} \delta \left(\omega_r - k_\parallel v_\parallel - \frac{\omega_c}{\gamma} \right) dv_\parallel, \qquad (A.7)$$

the distribution function ($f(v_\parallel, v_\perp)$) was normalized to unity and the plasma frequency ($\omega_p^2 = ne^2/m\epsilon_0$ being n the electron density) was introduced. This result was derived for the first time by Wu and Lee (1979).

---

[1] $P \int_{-\infty}^{+\infty} \frac{f(x)}{x-x_0} dx = \lim_{\epsilon \to 0^+} \left[\int_{-\infty}^{x_0-\epsilon} \frac{f(x)}{x-x_0} dx + \int_{x_0+\epsilon}^{+\infty} \frac{f(x)}{x-x_0} dx \right]$, where P indicates the principal value of Cauchy

APPENDIX B

B.1 Emission tracks in the CML-Φ_{Io} plane - Additional results

Here, we show the emissions tracks as function of CML and Φ_{Io} together with the corresponding emission occurrence probability versus CML (top) and Φ_{Io} (right) per year of observation. The source regions are indicated with different colors for each emission type as recorded in the catalog. The occurrence probability corresponds to the number of minutes of emissions per 5° bin of each coordinate and it has been normalized by the total number of observations held during the year in the same bin.
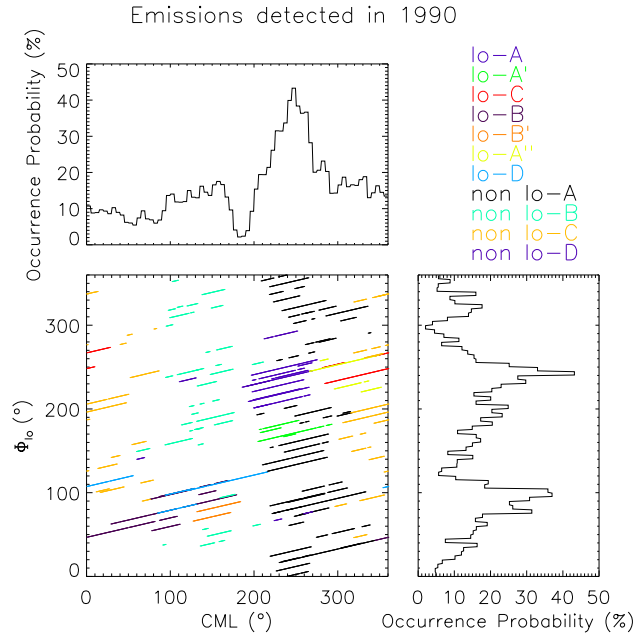
Figure B.1 - Distribution of emissions in the CML-Φ_{Io} plane detected in 1990.
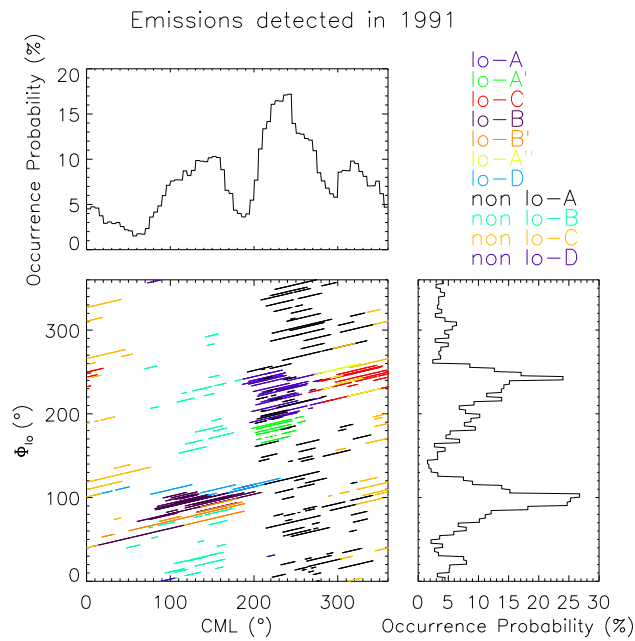
Figure B.2 - Distribution of emissions in the CML-Φ_{Io} plane detected in 1991.
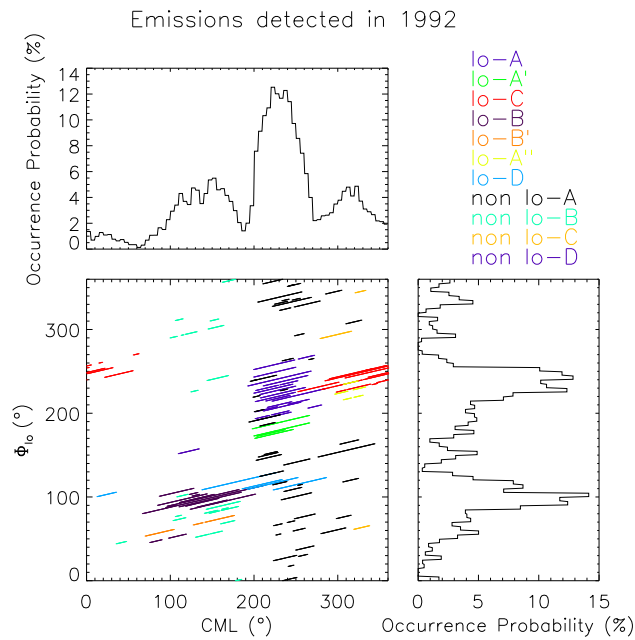
Figure B.3 - Distribution of emissions in the CML-Φ_{Io} plane detected in 1992.
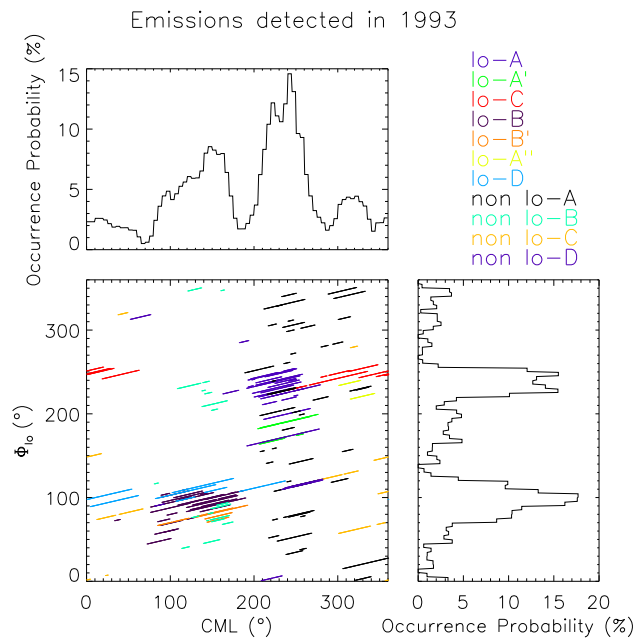
Figure B.4 - Distribution of emissions in the CML-Φ_{Io} plane detected in 1993.
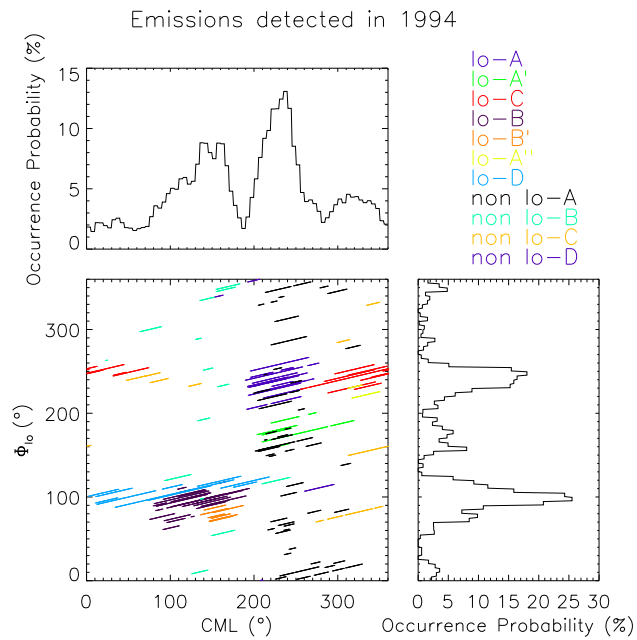
Figure B.5 - Distribution of emissions in the CML-Φ_{Io} plane detected in 1994.
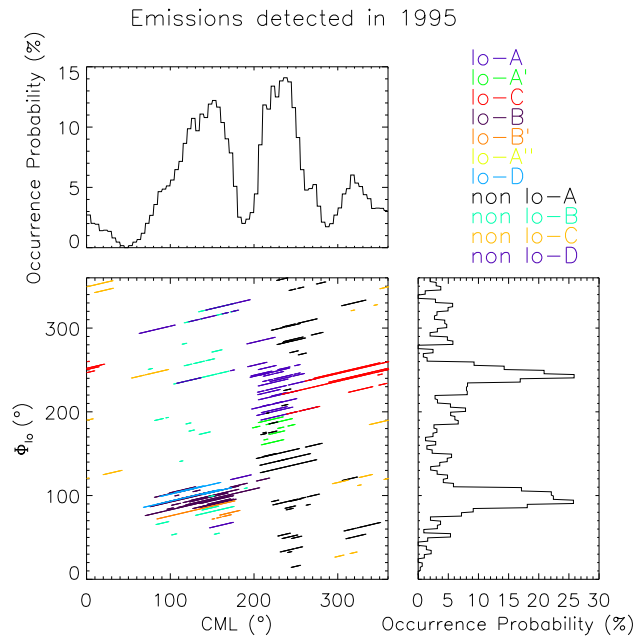
Figure B.6 - Distribution of emissions in the CML-Φ_{Io} plane detected in 1995.
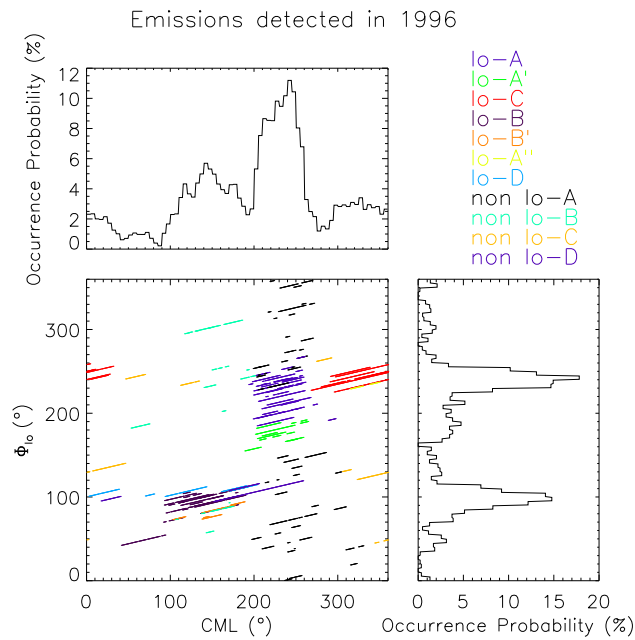
Figure B.7 - Distribution of emissions in the CML-Φ_{Io} plane detected in 1996.
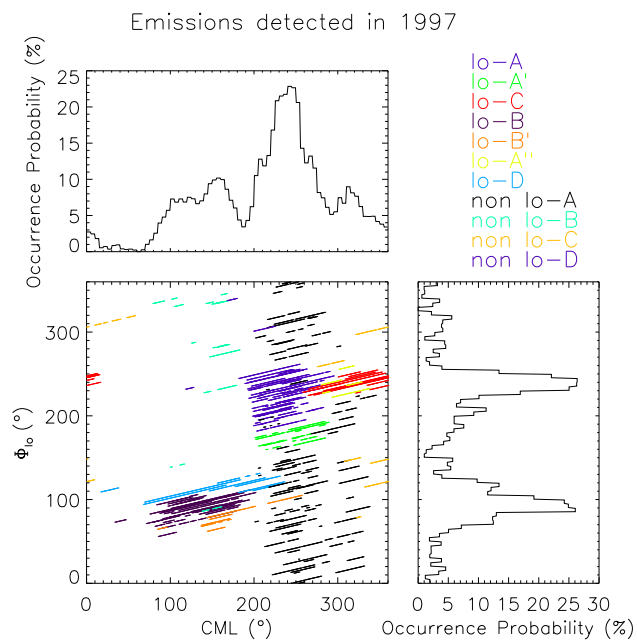
Figure B.8 - Distribution of emissions in the CML-Φ_{Io} plane detected in 1997.
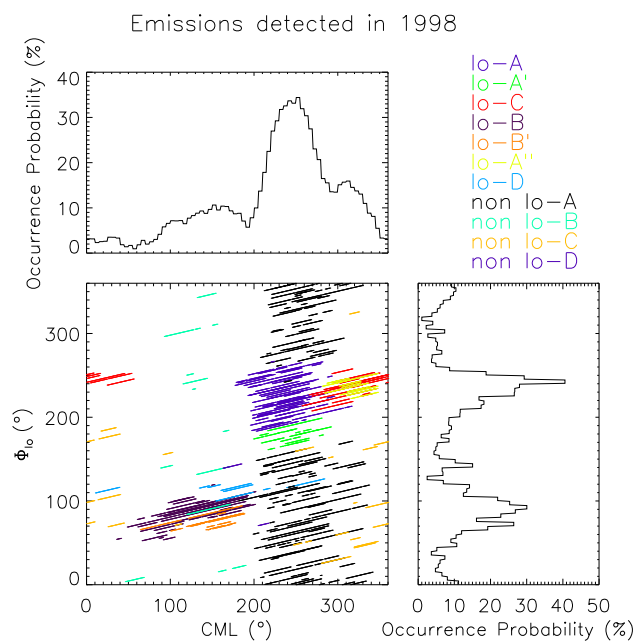
Figure B.9 - Distribution of emissions in the CML-Φ_{Io} plane detected in 1998.
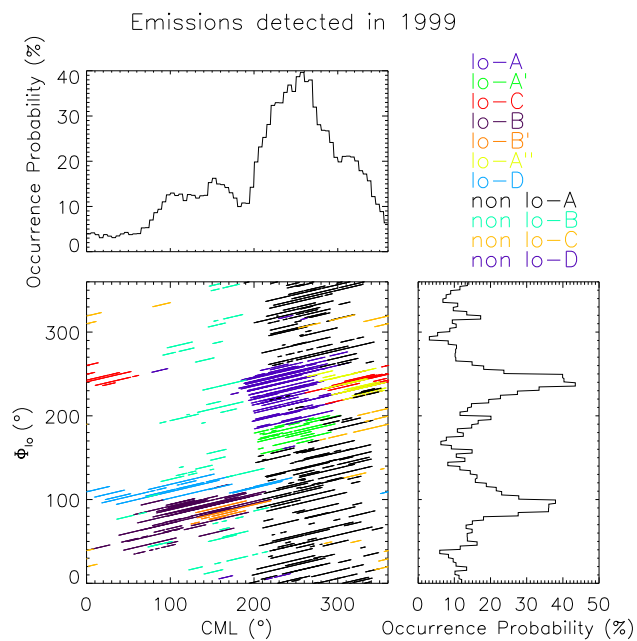
Figure B.10 - Distribution of emissions in the CML-Φ_{Io} plane detected in 1999.
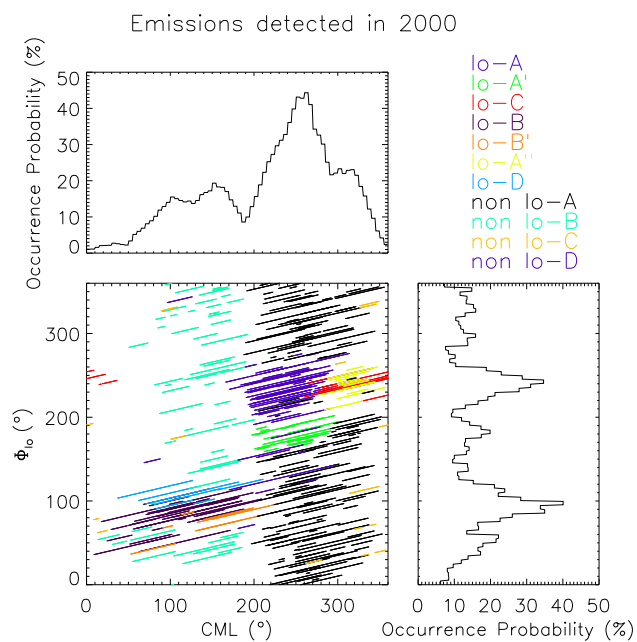
Figure B.11 - Distribution of emissions in the CML-Φ_{Io} plane detected in 2000.
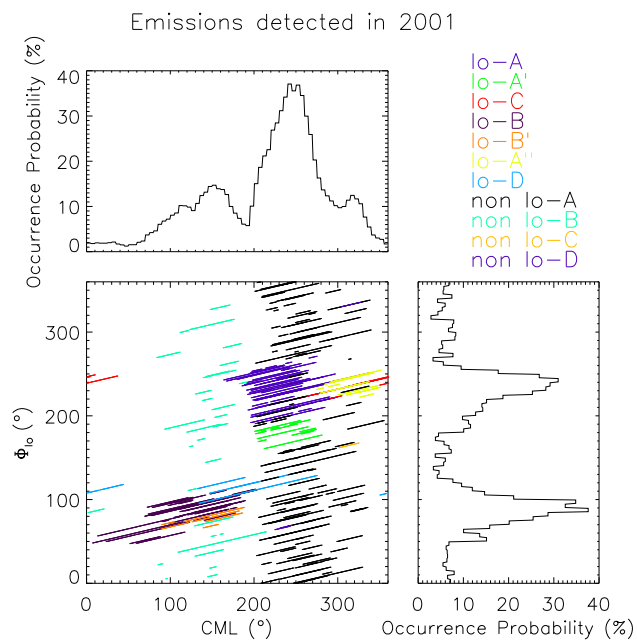
Figure B.12 - Distribution of emissions in the CML-Φ_{Io} plane detected in 2001.
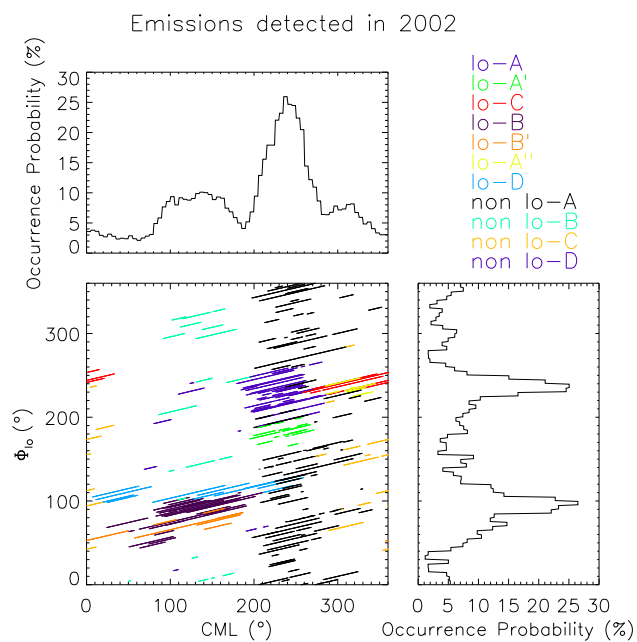
Figure B.13 - Distribution of emissions in the CML-Φ_{Io} plane detected in 2002.
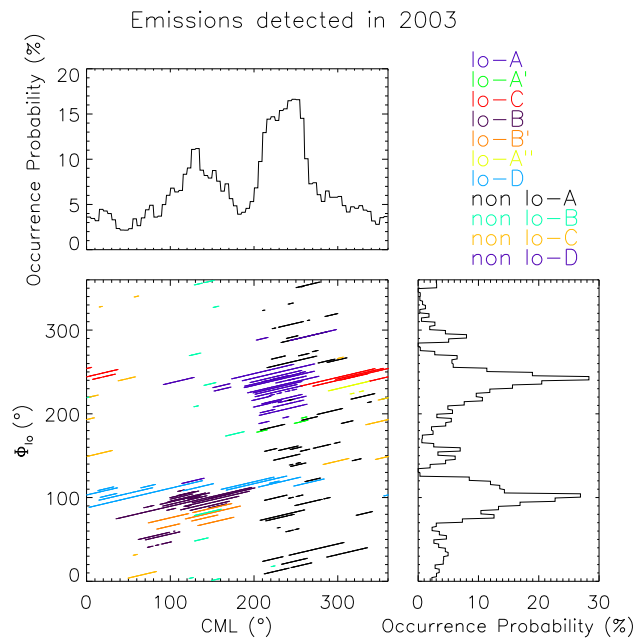
Figure B.14 - Distribution of emissions in the CML-Φ_{Io} plane detected in 2003.
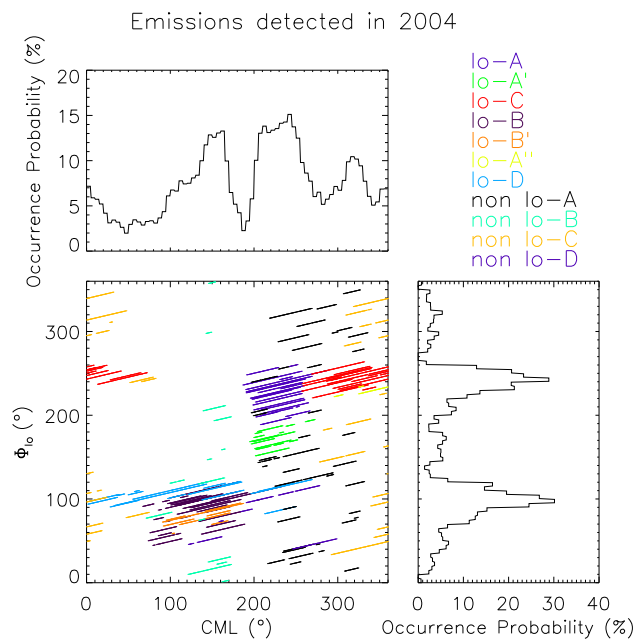
Figure B.15 - Distribution of emissions in the CML-Φ_{Io} plane detected in 2004.
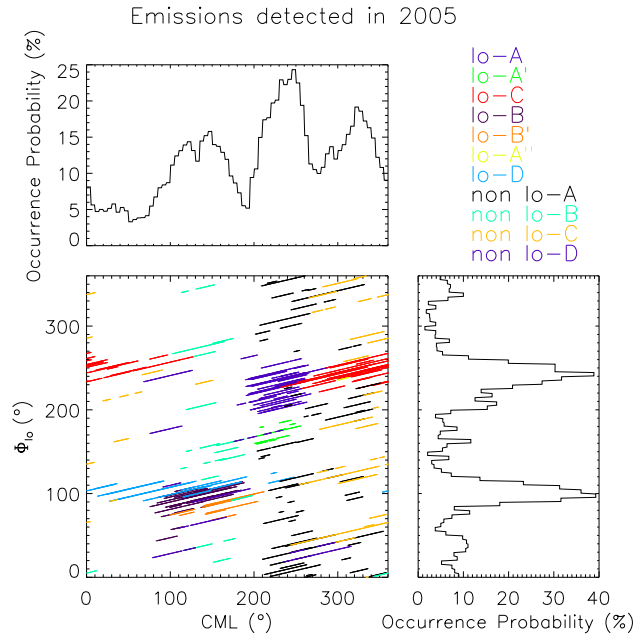
Figure B.16 - Distribution of emissions in the CML-Φ_{Io} plane detected in 2005.
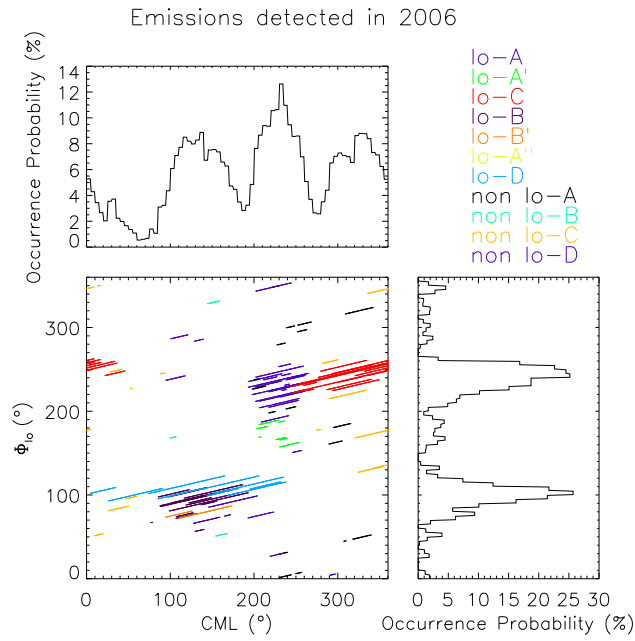
Figure B.17 - Distribution of emissions in the CML-Φ_{Io} plane detected in 2006.
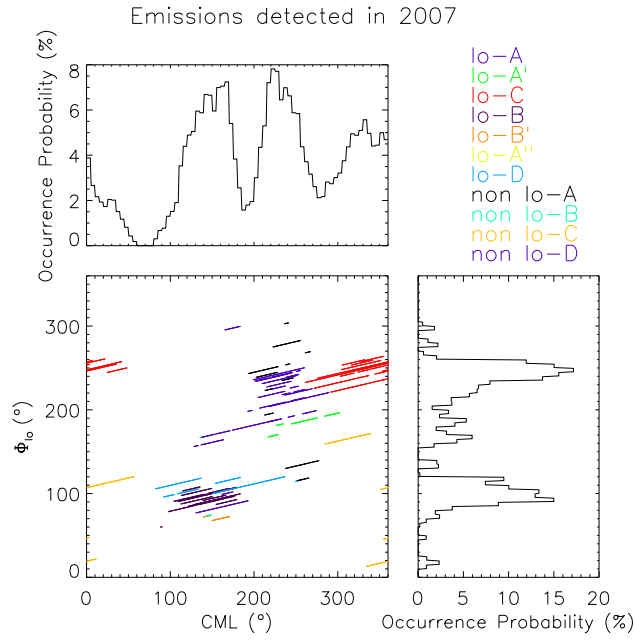
Figure B.18 - Distribution of emissions in the CML-Φ_{Io} plane detected in 2007.
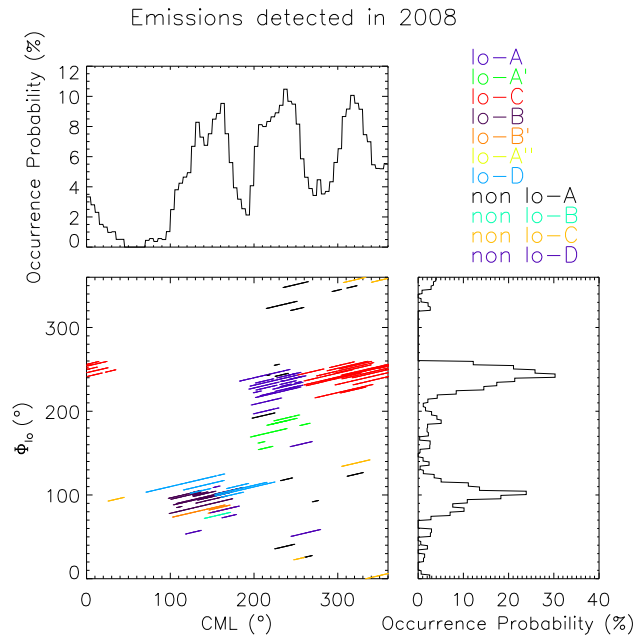
Figure B.19 - Distribution of emissions in the CML-Φ_{Io} plane detected in 2008.
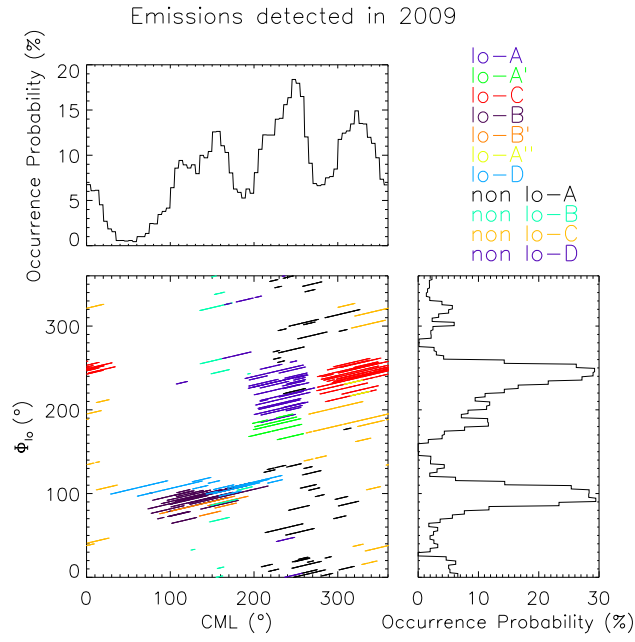
Figure B.20 - Distribution of emissions in the CML-Φ_{Io} plane detected in 2009.
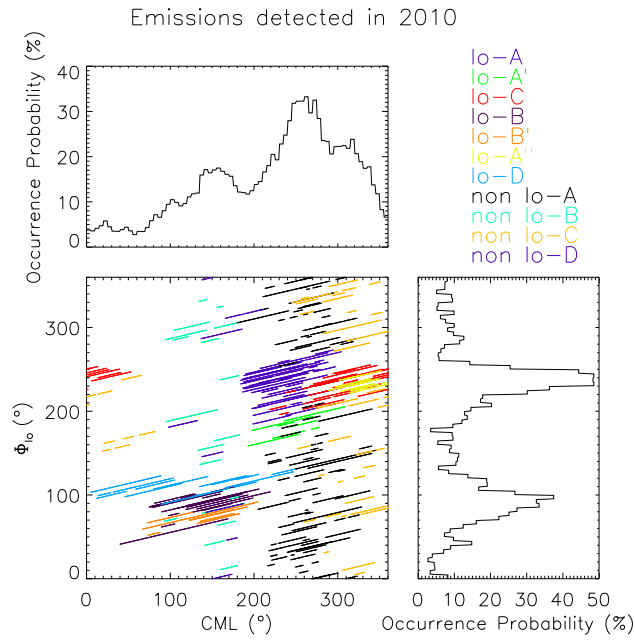
Figure B.21 - Distribution of emissions in the CML-Φ_{Io} plane detected in 2010.

95
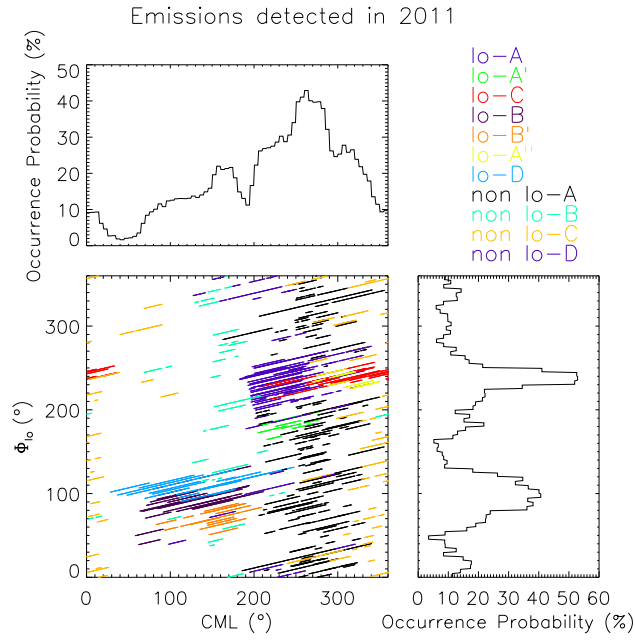
Figure B.22 - Distribution of emissions in the CML-Φ_{Io} plane detected in 2011.
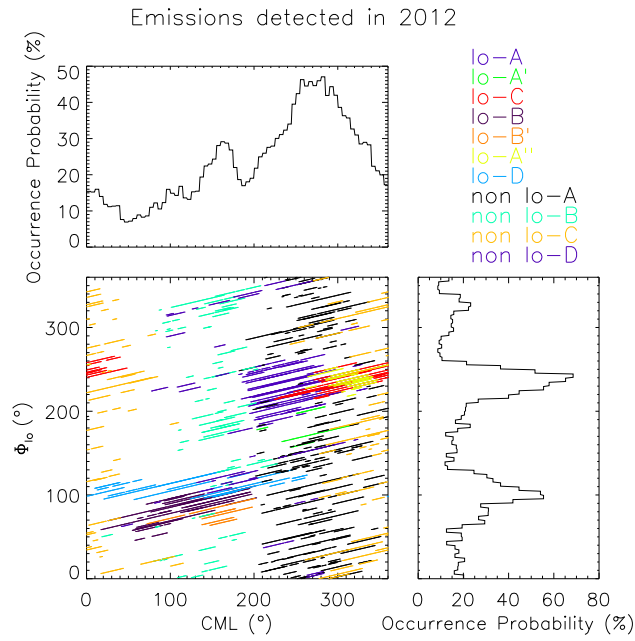
Figure B.23 - Distribution of emissions in the CML-Φ_{Io} plane detected in 2012.
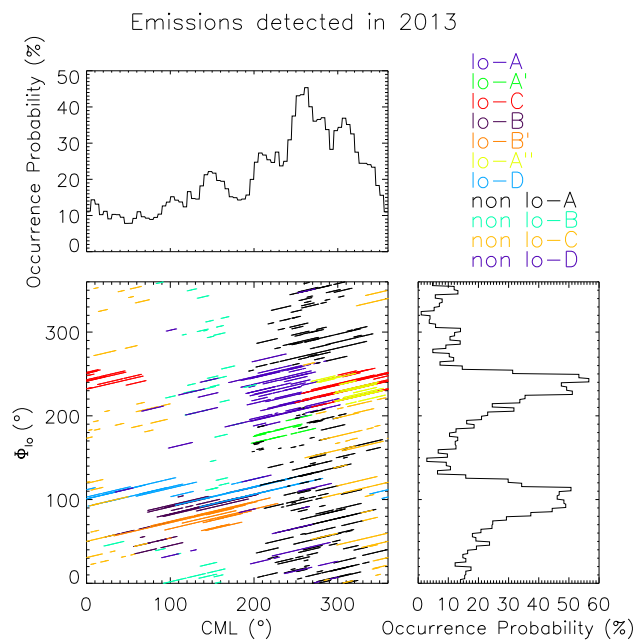
Figure B.24 - Distribution of emissions in the CML-Φ_{Io} plane detected in 2013.
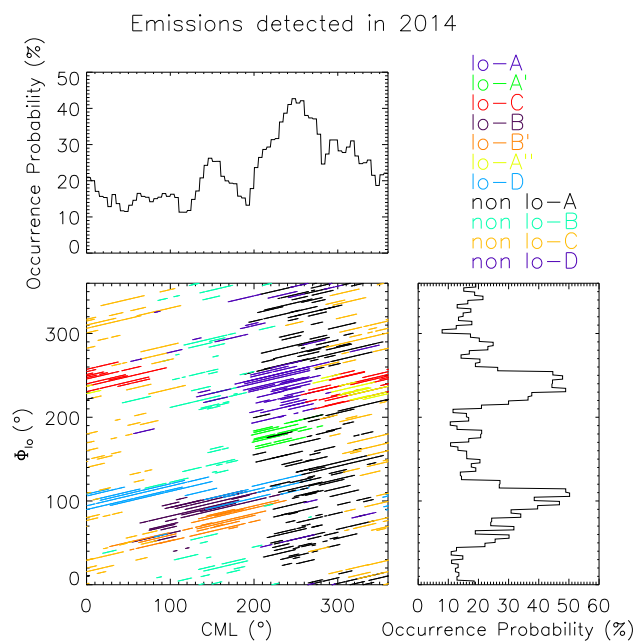
Figure B.25 - Distribution of emissions in the CML-Φ_{Io} plane detected in 2014.

Figure B.26 - Distribution of emissions in the CML-Φ_{Io} plane detected in 2015.

APPENDIX C

C.1 Declination and Solar activity effects on DAM-emissions - Additional results

Here, we show the occurrence probability in the CML-Φ_{Io} plane distribution in each band of declination, discussed in section 5.2.1 (cf. Figure 5.4).
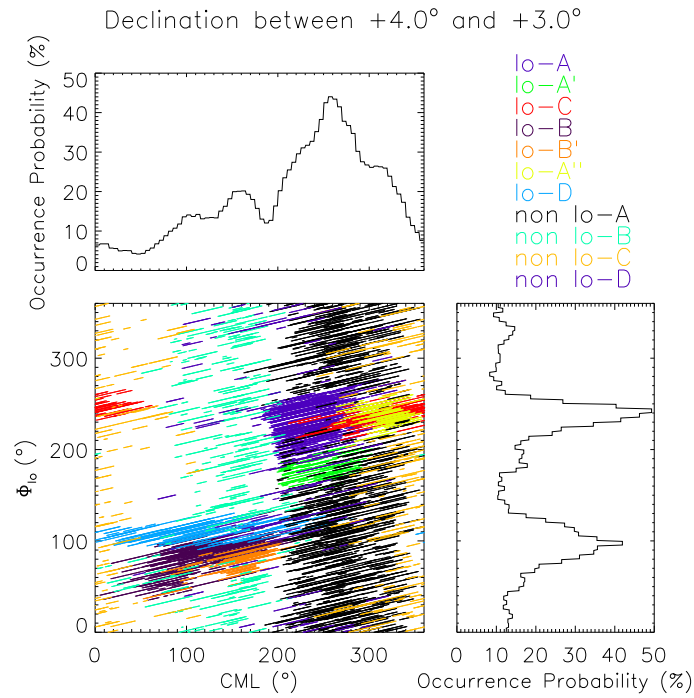
Figure C.1 - Distribution of emissions in the CML-Φ_{Io} plane for declination range between $+4°$ and $+3°$.
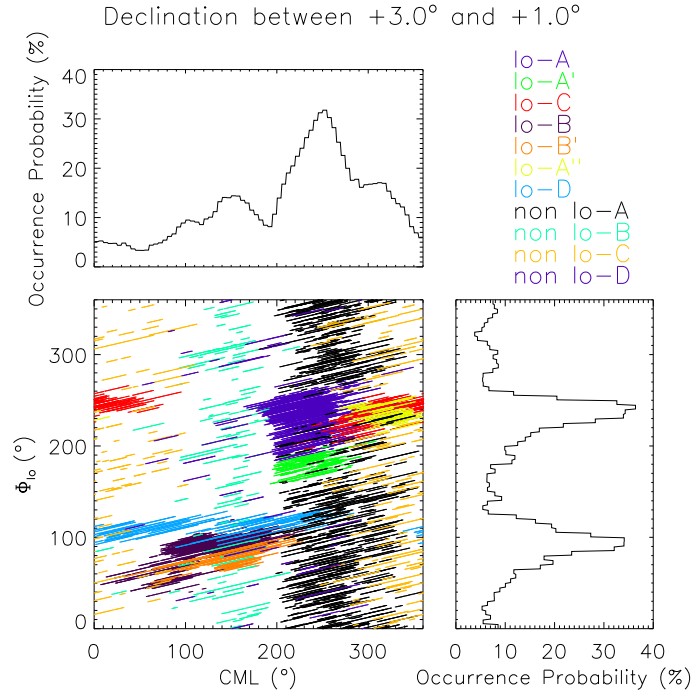
Figure C.2 - Distribution of emissions in the CML-Φ_{Io} plane for declination range between +3° and +1°.
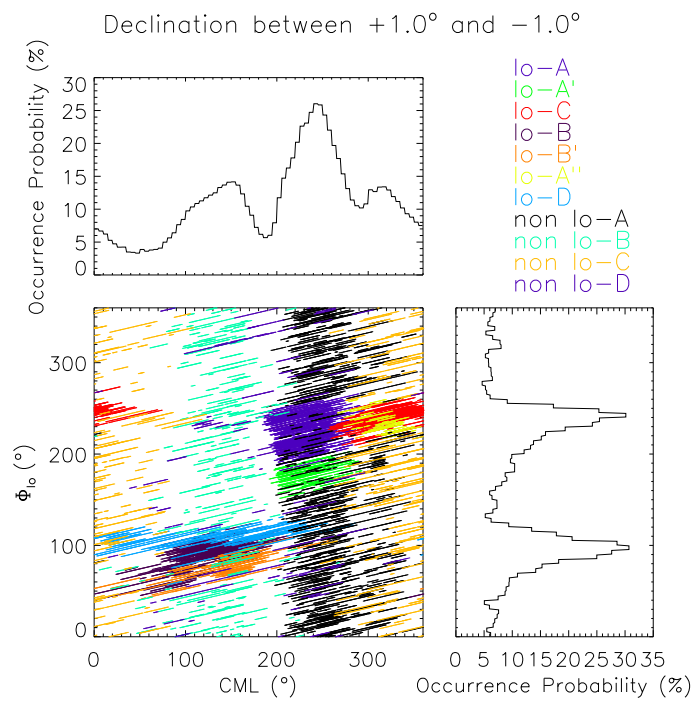
Figure C.3 - Distribution of emissions in the CML-Φ_{Io} plane for declination range between +1° and -1°.
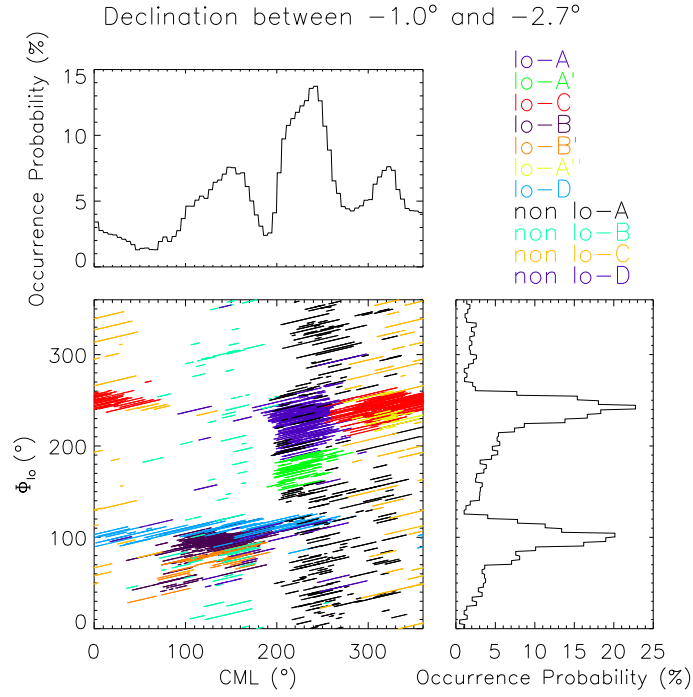
Figure C.4 - Distribution of emissions in the CML-Φ_{Io} plane for declination range between -1° and -2.7°.
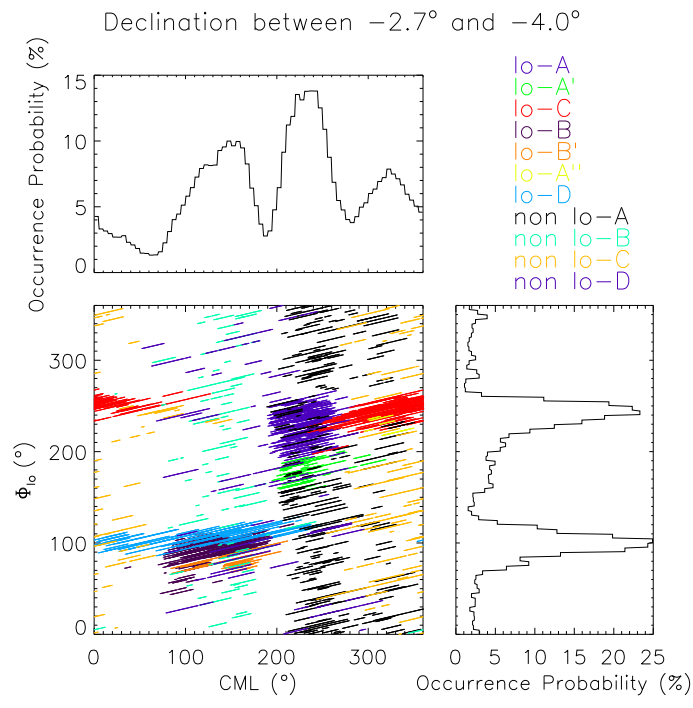
Figure C.5 - Distribution of emissions in the CML-Φ_{Io} plane for declination range between -2.7° and -4°.

PUBLICAÇÕES TÉCNICO-CIENTÍFICAS EDITADAS PELO INPE

Teses e Dissertações (TDI)

Teses e Dissertações apresentadas nos Cursos de Pós-Graduação do INPE.

Notas Técnico-Científicas (NTC)

Incluem resultados preliminares de pesquisa, descrição de equipamentos, descrição e ou documentação de programas de computador, descrição de sistemas e experimentos, apresentação de testes, dados, atlas, e documentação de projetos de engenharia.

Propostas e Relatórios de Projetos (PRP)

São propostas de projetos técnico-científicos e relatórios de acompanhamento de projetos, atividades e convênios.

Publicações Seriadas

São os seriados técnico-científicos: boletins, periódicos, anuários e anais de eventos (simpósios e congressos). Constam destas publicações o Internacional Standard Serial Number (ISSN), que é um código único e definitivo para identificação de títulos de seriados.

Pré-publicações (PRE)

Todos os artigos publicados em periódicos, anais e como capítulos de livros.

Manuais Técnicos (MAN)

São publicações de caráter técnico que incluem normas, procedimentos, instruções e orientações.

Relatórios de Pesquisa (RPQ)

Reportam resultados ou progressos de pesquisas tanto de natureza técnica quanto científica, cujo nível seja compatível com o de uma publicação em periódico nacional ou internacional.

Publicações Didáticas (PUD)

Incluem apostilas, notas de aula e manuais didáticos.

Programas de Computador (PDC)

São a seqüência de instruções ou códigos, expressos em uma linguagem de programação compilada ou interpretada, a ser executada por um computador para alcançar um determinado objetivo. Aceitam-se tanto programas fonte quanto os executáveis.